2018

Investigation of Oxy-fuel Combustion Behind Reflected Shockwaves

Owen Pryor
University of Central Florida

INVESTIGATION OF OXY-FUEL COMBUSTION

BEHIND REFLECTED SHOCK WAVES

by

OWEN MARCUS PRYOR

M.S. University of Central Florida, 2016
B.S. University of Central Florida, 2014
B.A. University of Central Florida, 2014

A dissertation submitted in partial fulfillment of the requirements
for the degree of Doctor of Philosophy in Mechanical Engineering
in the Department of Mechanical and Aerospace Engineering
in the College of Engineering and Computer Science
at the University of Central Florida
Orlando, Florida

Summer Term
2018

Major Professor: Subith Vasu Sumathi

ABSTRACT

Supercritical carbon dioxide has brought about new questions on the chemical kinetics of several small hydrocarbon fuels and the effects of carbon dioxide as the primary diluent on the different fuels. This report presents work on the ignition delay times and several species time-histories of methane, ethylene and syngas over a range of conditions. All experiments were conducted behind reflected shock waves using two different shock tubes. The ignition delay times were measured using a GaP photodetector to measure the emission of light. The species time-histories were measured using single laser spectroscopy. The effect of CO_2 as a diluent on the fluid dynamics of the system were also examined using high-speed camera images. It was determined that the ignition delay times and fuel time-histories were able to be accurately predicted by mechanisms in the literature for pressures up to 30 atm but the literature mechanisms were unable to predict the carbon monoxide time-histories beyond qualitative trends for the various fuels. It was also determined that the carbon monoxide had a string effect on the fluid dynamics of the experiments resulting in a significantly smaller chemical reaction zone. Experiments were also performed to examine the effects of water as a diluent with a ratio up to 66% of the total diluent on the ignition delay times. Using the experimental data, a global kinetic mechanism was created for methane and syngas to predict the ignition delay times and the carbon monoxide time-histories for pressures up to 300 atm.

ACKNOWLEDGMENTS

I would like to thank my advisor and mentor, Dr. Subith Vasu, for all the guidance and assistance throughout my years of study. This work would not have been possible without the help of my many coworkers and friends in the Vasu Lab, especially Dr. Batikan Koroglu, who taught me so much about research while developing the shock tube.

I would also like to thank the different professors that helped me along including Dr. Jayanta Kapat and Dr. Seetha Raghavan. This work would not have been possible without the assistance from the many people who helped me during my visit to the German Aerospace Center under the guidance of Drs. Marina Braun-Unkhoff and Clemens Naumann.

Finally, I would like to thank my family for their constant encouragement and patience. My mother and brothers have been a constant throughout this long journey. I know that this would never have been possible without my father encouraging me to pursue engineering when I was young, and I will be eternally grateful.

TABLE OF CONTENTS

LIST OF FIGURES

LIST OF TABLES

LIST OF EQUATIONS

CHAPTER 1: INTRODUCTION AND BACKGROUND

Oxy-fuel combustion is a potential solution for improving current engine technology and reducing harmful pollutants. By burning oxygen instead of air which contains nitrogen, the chemistry is reduced to carbon dioxide and water as the only products. This allows for separation of the products as water may be easily condensed and removed from the cycle completely. Once the water is removed, the carbon dioxide may be captured and stored through sequestration [1-3]. The problem with oxy-fuel combustion is that such a mixture as Fuel+O2 is incredibly volatile and hard to control and is the reason that engines use air as the oxidizer so that the oxygen may be diluted, and the reactions controlled. The solution explored in this thesis is the use of carbon dioxide as the diluent as it is already a product. This would allow for the same method of carbon dioxide isolation for sequestration and is also allows for more controlled reactions.

The next step for carbon dioxide diluted mixtures is referred to as supercritical carbon dioxide. Supercritical carbon dioxide combines the simplicity of oxy-fuel combustion with the high density of a supercritical fluid to increase the power output of the system. By operating the system at pressures between 100 atm (low pressure) and 300 atm (high pressure), the carbon dioxide will operate above its critical point of 71 atm for the duration of the cycle. According to simulations done at the Southwest Research Institute, this has the potential to increase the efficiency of the cycle to as high as 64% while maintaining zero NO_x emissions and capturing up to 99% of the carbon dioxide created [4, 5]. The cost of such a system has been shown be comparable at a price of $121/MWh compared to conventional coal ($96.60/MWh) or natural gas ($128.4/MWe) [4, 6].

Two fuels are currently considered to be used in the supercritical cycle and are explored in detail, methane and syngas. The first is the main component in natural gas and the second is a synthetic fuel created from combinations of hydrogen and carbon monoxide. Both fuels are well understood and considered to be the two most likely fuels to be used in supercritical cycles.

The problem is that there are no mechanisms that have been validated for carbon dioxide diluted mixtures nor at the relevant temperatures and pressures needed for a supercritical fluid to be present. One method for improving our understanding is to use laser diagnostics to measure the time-histories of key species during the combustion process. It has been shown through experimentation and sensitivity analysis that carbon dioxide is not an inert gas like other diluents (Ar, N_2, etc.). The third body collision rate changes dramatically for the H_2/O_2 combustion [7, 8]. Also, it has been revealed that CO_2 plays a much larger role in the reactions than N_2. Through competition with O_2 for H atoms, CO_2 reduces the radical pools that help propagate combustion reducing the overall speed at which the reaction takes place based on the below reaction (1) [9-11].

$$CO_2 + H \leftrightarrow CO + OH \quad (1)$$

Therefore, measuring the carbon monoxide time-histories could help shed further light on this important reaction. Current work has focused on the measurement of carbon monoxide time-histories with Argon as the primary diluent which will serve as a baseline for measurements of carbon monoxide time-histories in CO_2 diluted environments.

Carbon dioxide has also been shown to cause bifurcation in the shock wave which can lead to large fluid structures being formed in an area that is normally considered a stagnant region. The ideal shock tube theory assumes the following: diaphragm breaks instantly forming a constant speed shock wave; thermodynamic conditions and the flow velocity remain constant between the shock and the contact front; and, reflection from end wall produces uniform conditions behind reflected shock wave [12]. Actual shock tubes slightly deviate from ideal behavior: there is a finite diaphragm breaking and shock formation time; a boundary layer builds up due to viscous effects behind moving incident shock waves which affects the shock velocity described in the boundary layer models developed by the pioneering work of Mirels and co-workers [13-17]; interaction of the reflected shock wave with the boundary layer produces bifurcation [18], and non-uniform test conditions and affects the shock velocity; and contact-surface/reflected-shock interaction affects the available test times [19]. Bifurcation has the potential to create fluid structures in the system due to the separation of the boundary layer which may result in turbulence and non-stagnant flow. Turbulence often results in greater uncertainty in the system and may limit test times due to rising uncertainties. Bifurcation occurs because the boundary layer is not able to negotiate the pressure rise across the reflected shock when brought to rest relative to it, and is therefore trapped and carried along at the foot of the shock [20, 21]. Bifurcation features normally appear in diatomic and polyatomic gases (such as fuel/air mixtures, mixtures with CO_2) but not in argon diluted mixtures and its features have been well-known through experimental visualization utilizing color schlieren [22] and side-wall pressure measurements [23, 24]. Bifurcation has been modeled in many computational studies [25-29]. It has been shown that bifurcation causes large fluid fluctuations behind the reflected shock wave with large vorticity and an unstable shear layer.

Bifurcation affects determination of time zero because of the uncertainty in determining the arrival of the normal shock wave at the sidewall location and its effects are severe as one moves away from the end wall and for short ignition delay times (<100 μs). However, it is commonly assumed that bifurcation should not affect the core portion of the post-shock region, which comprises most of the flow area [23]. However, a comprehensive study using multiple diagnostics to verify the influence of bifurcation and inhomogeneity on chemical kinetics is lacking in the literature though similar studies in rapid compression machines have been carried out by Walton et al. [30]. It was determined, through imaging that two ignition regimes (mild and strong) were present for iso-octane mixtures and that there was good agreement between the simulations and experimental results.

This dissertation explores various aspects of oxy-fuel combustion. Experiments were performed using a shock tube to measure the ignition delay times, methane time-histories and carbon monoxide time-histories during the combustion of methane, syngas and ethylene. The experiments were also performed to understand the fluid dynamics of such a system by using high-speed imaging. The experiments were performed at the University of Central Florida and the Deutsches Zentrum für Luft und Raumfahrt (DLR).

CHAPTER 2: SHOCK TUBE THEORY

To understand the roles that carbon dioxide would play in new combustion systems, experiments were performed to probe various aspects of the chemical kinetics. The experiments were performed behind reflected shock waves utilizing two different shock tube facilities at the University of Central Florida and the Deutsches Zentrum für Luft- und Raumfahrt in Stuttgart, Germany (DLR).

A shock tube is an experimental apparatus that is used to create shock waves in a structured and repeatable method. The shock wave that is formed travels along a constrained path before arriving at an end wall that causes it to reflect backwards into the flow creating a stagnation region near the end wall as the flow is forcibly stopped by the reflection.

The shock wave is formed by creating a pressure disparity across a membrane at some point in the tube. One section is filled with to a high pressure with a gas while the other section is filled with the desired test mixture. By removing the membrane, the system attempts to reach an equilibrium pressure by creating a shock wave that propagates along the low-pressure system. The shock wave eventually reaches the end of the device where it reflects from the solid surface and travels backward. While the shockwave is formed to propagate along the low-pressure system, expansion waves form to bring the high-pressure section to the desired equilibrium point. The expansion waves travel backwards eventually reflecting at the back wall. The experiment typically ends when the boundary region between the two different gas mixtures (contact surface) passes the reflected shock wave into the stagnation zone. The entire system is eventually brought to equilibrium when

the reflected shock wave and the expansion waves collide with each other. Figure 1 shows a diagram of the experiment. The first image is before the membrane is removed and the system is divided into two sections. The second image shows the shock wave and the expansion waves propagating along their respective regions and the final image is after the reflecting of the shock wave and expansion waves.

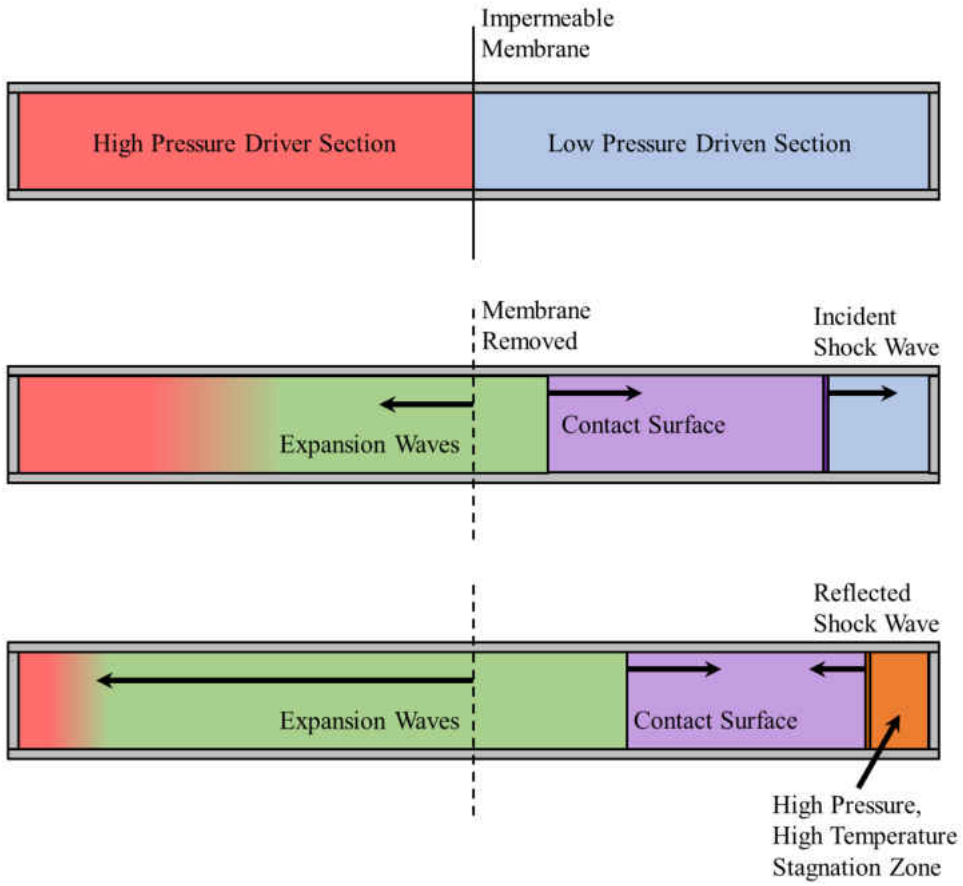

Figure 1: Diagram of shock tube during experiment. Experiment starts with two sections at different pressures. The membrane is removed, and a shock wave and expansion waves form to force equilibrium. Shock wave reflects at the end wall causing a high-pressure, high-temperature stagnation zone.

The major benefit to using shock tubes for chemical kinetics is a result of the stagnation zone that occurs. As the gases behind the reflected shock wave are quiescent, the chemistry of a given

mixture may be isolated with interfering effects of fluid dynamics, heat transfer or other physical phenomenon that could influence the experiment. Another major benefit is that shock tubes are highly repeatable experiments do to the simplicity of the experiment. The strength of the shock wave is adjusted by controlling the Mach Number of the shock wave through the pressure ratio between the original high-pressure and low-pressure sections. The experiment is capable of easily being repeated by utilizing the same pressure ratio across the membrane.

2.1 Velocity, temperature and pressure calculations

The shock wave and the stagnation zone are characterized by understanding the strength of the shock wave. Three main properties are calculated for each experiment, the velocity of the shock wave, the temperature behind the reflected shock wave and the pressure behind the reflected shock wave.

The velocity is calculated by measuring the time interval that it takes the shock wave to pass two locations with a known distance separating them. By calculating the velocity at several points, the velocity at the end wall can be calculated using a linear regression analysis using the method of least squares [31]. The velocity is calculated at several locations as a boundary layer is formed at the along the walls of the shock tube and reduces the speed of the shock wave as it travels and the final velocity at the end wall is extrapolated from the analysis.

Once the velocity is known, the temperature and pressure can be calculated for both the incident shock wave and the reflected shock wave. The conditions in the low-pressure, driven region are

first calculated from the initial temperature and pressure in that region. The temperature and pressure behind the incident shock wave are then calculated by simultaneously solving the Rankine-Hugoniot Relation (2) and the Conservation of Energy simultaneously (3).

$$\frac{p_2}{p_1} = 1 + \rho_1 \frac{{u_s}^2}{p_1}\left(1 - \frac{\rho_1}{\rho_2}\right) \tag{2}$$

$$h_2 - h_1 = \frac{{u_s}^2}{2}\left[1 - \left(\frac{\rho_1}{\rho_2}\right)^2\right] \tag{3}$$

The equations are solved by initially guessing that the shock waves follow the ideal normal shock equations described in general shock wave theory [32]. Solving the equations using Cramer's Rule, the temperature and pressure behind the incident shock wave are solved.

Now that the temperature and pressure behind the incident shock wave is known, the conditions behind the reflected shock wave can be calculated using a similar procedure. The main difference between the incident and reflected shock waves are the altered coordinate system resulting from the reflection. The shock velocity of the reflected shockwave is calculated using … The equations listed below represent the updated Rankine-Hugoniot Relation (4) and the Conservation of Energy (5) after the coordinate system has been considered.

$$\frac{p_5}{p_2} = 1 + \frac{\rho_2}{p_2}\left[\frac{(u_s - u_2)^2}{1 - \frac{\rho_2}{\rho_5}}\right] \tag{4}$$

$$h_5 - h_2 = \frac{(u_s - u_2)^2}{2}\left(\frac{1+\frac{\rho_2}{\rho_5}}{1-\frac{\rho_2}{\rho_5}}\right) \quad (5)$$

2.2 Experimental uncertainty of the shock tube

As the temperature, pressure and velocity must be calculated, the uncertainty of each element applied must be considered to determine the uncertainty of the overall system. The uncertainty of the shock tube started with determining the uncertainty in the initial pressure and temperature of the driven section, the time interval between each point as the shock wave passes and the fundamental parameters and constants of the gases.

The uncertainty in the velocity was calculated using the same linear regression analysis method outlined in Bevington and Robinson [31]. The equation of the line that the velocity depreciates at was calculated and then the uncertainty for the slope and the intercept was estimated using the method outlined. The uncertainty in the velocity has been shown to be less than 1% for all experiments.

The uncertainty in the pressure and temperature behind the reflected shock wave was not able to be estimated using the typical uncertainty equation (6). Since the temperature and the pressure were solved simultaneously, no equation could be derived to factor in the uncertainty of the of the unknown quantity. Instead the uncertainty in the temperature and pressure were solved by estimating the uncertainty for each of the different elements that are used to solve the two equations. These elements are the initial pressure and temperature in the driven section, the

velocity of the shock wave and the mixture composition in the driven section. The initial pressure uncertainty was estimated to be 0.25% of the reading based on the specs of the system and the standard uncertainty in the thermocouple of 0.5 K was used. The uncertainty in the velocity was calculated using the method outlined above. The uncertainty in the mixture composition was calculated by calculating the uncertainty of each pressure measurement that was used to create the overall mixture.

$$\sigma_{x_i} = \sqrt{\sum_j \left(\sigma_j \frac{\partial x_i}{\partial x_j}\right)^2} \tag{6}$$

The temperature and pressure behind both the incident and reflected shock waves were then solved over the range of uncertainty for each of the four elements and a statistical analysis was applied to determine the overall uncertainty in the shock conditions. The uncertainty in the reflected shock temperature was estimated to be less than 1.1% for all conditions with an average uncertainty of 0.9% of the calculated value. The uncertainty in the reflected shock pressure was estimated to be less than 1.8% for all experiments.

CHAPTER 3: EXPERIMENTAL PROCEDURE AND DIAGNOSTICS

3.1 Shock tube facility at UCF

The UCF shock tube was used for most of the experiments. The shock tube consists of a 14.2 cm diameter with optical access 2 cm from the end wall for diagnostics. A four-blade cutter located on the driven side was used to rupture the 5 mil Lexan sheets at a known pressure in this study. Two Agilent DS 102 rotary vane pumps lowered the pressure on either side of the diaphragm. An Agilent V301 turbo-molecular vacuum pump was used to lower the driven pressure to below 50 μtorr before each experiment. The vacuum pressure for each experiment was measured using a combination of a convection gauge and an ionization gauge (Lesker KJL275804LL and Lesker KJLC354401YF). This allowed for a range of pressures to be measured between 10^{-9} torr and 1000 torr. The velocity of the shock wave was measured using five PCB 113B26 piezoelectric pressure transducers attached to four Agilent 53220A timer-counters. The velocity of the shock wave is then extrapolated to the end wall to calculate the temperature and pressure at the test location. The average uncertainty of the temperature and pressure has been measured to be around 2% for both the reflected temperature and reflected pressure leading to typical uncertainties of around 20% for shock tube ignition delay times measurements [33].

3.1.1 Mixing Facility

All mixtures were prepared in a 33L mixing tank made of Teflon coated stainless steel. The mixing tank was vacuumed before each mixture overnight to ensure the most accurate mixture possible.

The mixing tank utilized a magnetically driven stirrer to ensure homogeneity of the mixture. All gasses for the experiments were purchased from Praxair and were of research quality (≥99.99%). The mixtures were made using a partial pressure method through a gas manifold. The pressure was measured using two manometers with full scale ranges of 100 and 10,000 torr baratrons (MKS E27D and MKS 628D). Mixtures were given a minimum of 6 hours to ensure proper mixing before being inserted into the shock tube through the gas manifold. The initial pressure for each experiment was measured using the baratrons attached to the gas manifold.

3.1.2 Shock tube heating

3.2 Diagnostics

Several different diagnostic systems were used to explore the various aspects of oxy-fuel combustion inside of the shock tube. The diagnostics include the pressure inside of the test section, high-speed imaging of the test area, the emission of light from combustion and two distinct species time-histories.

3.2.1 Pressure and emissions measurements

The pressure inside the test section is measured using a Kistler 603B1 pressure transducer with an RTV coating. The chemiluminescent emission was recorded to determine the ignition delay time using a GaP trans-impedance amplified detector from Thorlabs (PDA25K). These diagnostics are to determine the extent of pressure fluctuations after the reflected shock wave passes two

centimeters from the end wall of the shock tube. The emission measurement is used to determine the ignition delay time of the mixture at the calculated temperature and pressure. Combined these two measurements show the global reactivity of a given mixture. A schematic of the emission and pressure system is shown below in Figure 2 A and an example of the experimental data taken from the system is shown in Figure 2 B.

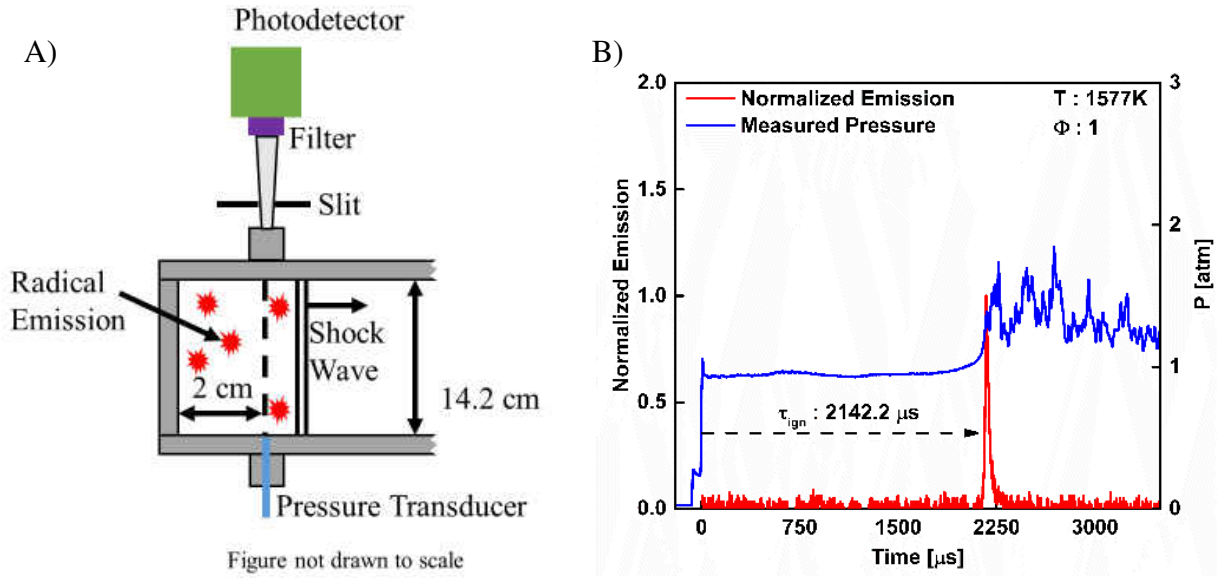

Figure 2: Ignition delay time and pressure measurements inside the shock tube. A) Schematic of the ignition delay times and the pressure measurements. B) example of the experimental data taken from the shock tube (Red Normalized Emission, Blue: Measured Pressure).

3.2.2 Laser absorption diagnostics for methane and carbon monoxide time-histories

Methane time-histories were measured using a continuous wave distributed feedback interband cascade laser from Nanoplus. Two HgCdTe (MCT) detectors (Vigo Systems PVI-2TE-3.4) were used to measure the laser intensity to obtain the absorbance of the laser beam during the experiment. Using this laser, absorption due to P(8) rovibrational transition line located in the ν_3

vibrational band of methane was measured and compared to the initial strength of the laser when the shock tube was under vacuum [34]. This line corresponds to 3403.4 nm and has been described as a good choice for time-resolved measurements of methane concentrations [33, 35-41]. The methane concentration was determined using the Beer-Lambert Law and converting the absorbance into the mole fraction (7).

$$\alpha = -ln\left(\frac{I_{tr}}{I_{ref}}\right)_{\nu} = \sigma(\nu, T, P)\frac{P_{tot}}{RT}\chi L \tag{7}$$

where α is the absorbance, I_{tr} is the intensity of light that passes through the shock tube, I_{ref} is the reference intensity in a vacuum, σ is the absorption cross-section, P_{tot} is the pressure behind the reflected shock wave, R is the specific gas constant, T is the temperature behind the reflected shock wave, X is the mole fraction of methane, and L is the diameter of the shock tube. Using the absorption cross-sections that were measured in Koroglu et al. [33], the methane mole fraction was measured over time for each experiment with typical uncertainties around 6%.

The carbon monoxide time-histories were measured using a quantum cascade laser (Thorlabs QD4580CM1) centered at 4580.4 nm which probes the R(10) transition line for carbon monoxide. This allows for accurate measurements of carbon monoxide using the Beer-Lambert law above. Figure 3 shows the schematic used for both laser setups.

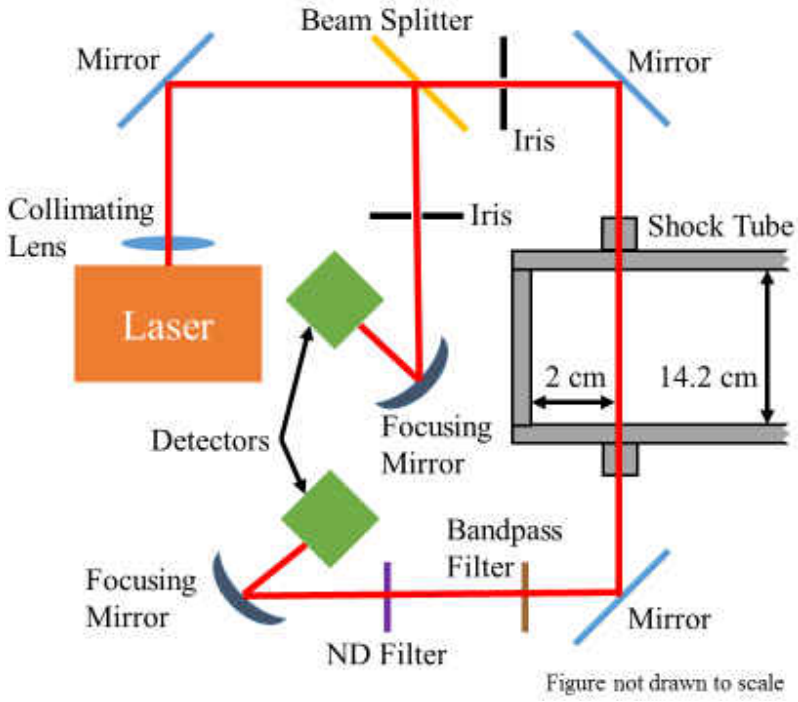

Figure 3: Schematic for single species absorption laser setup

3.2.3 High-speed camera imaging

High-speed camera images were taken to compare with other measurements for all experiments based on a similar method performed by Troutman et al [42]. A Phantom V710 camera was used to record the combustion process with a 256 x 256 resolution at a rate of 67,065 frames per second corresponding to a time resolution of 14.91 μs. The camera was positioned perpendicular to the shock tube so that the entire axial cross-section could be captured by the camera. The camera was focused at the plane corresponding to 2 cm from the end-wall to match the location of the pressure, laser and emission diagnostics. The camera was triggered on the voltage rise of the Kistler pressure transducer. It triggered after the voltage read 2 V for 5 μs. Once triggered, 5,000 frames were then taken before and after frame 0 to ensure that the entire process was captured with a total time span

of 150 ms. Figure 4 A shows the schematic of the camera system and the post-processed output. Figure 4 B shows the processed data that is displayed comparing different methods for measuring the ignition delay time.

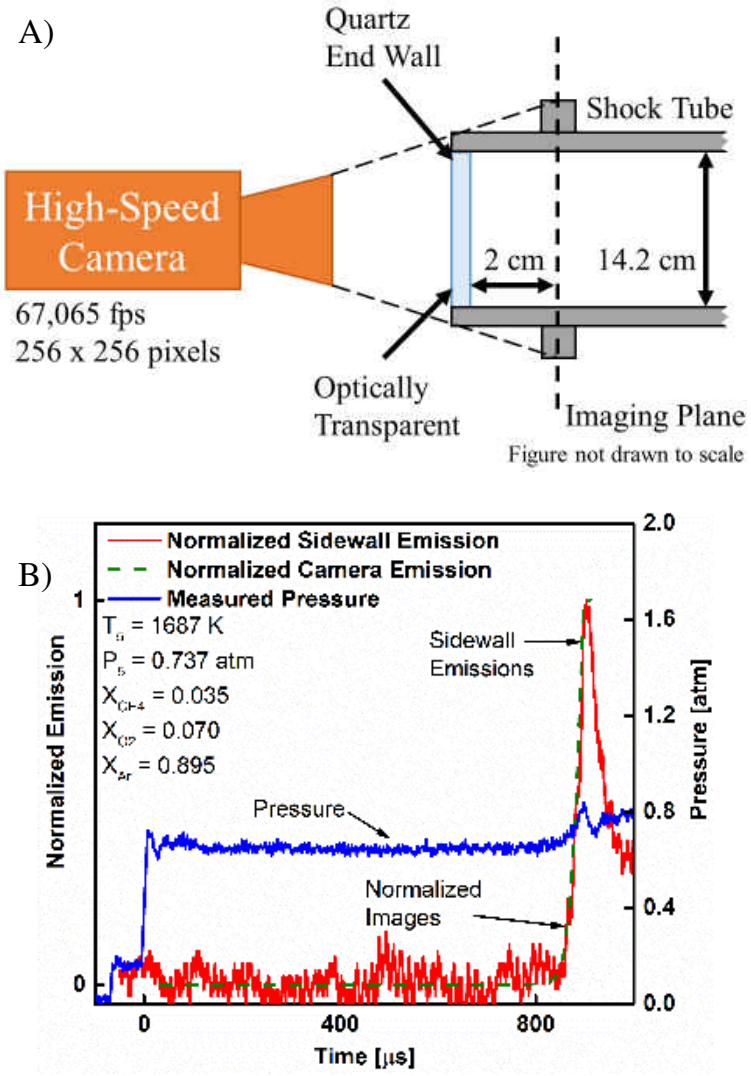

Figure 4: (A) Schematic for the high-speed imaging and post-processed output (not drawn to scale). (B) Comparison of measured pressure and sidewall emission of chemiluminescence with camera emission.

3.3 Numerical simulations

Numerical simulations were performed using Chemkin Pro [43] to compare with experimental data. Two methane mechanisms were used: 1) GRI 3.0 consisting of 325 reactions and 53 species [44], and 2) Aramco 2.0 containing 493 species and 2716 reactions [45]. The common method for modeling a shock tube is to consider the system as a closed-homogeneous batch reactor [33]. This approach treats the entire system as a premixed system that has no mass or energy transfer across the boundary but ignores any spatial differences in the system. Simulations were performed by constraining the volume and solving for the energy equation. The ignition delay times were calculated based on the temperature inflection point over the range of temperatures measured by the experiments. The temperature inflection point is the midpoint of the temperature rise during ignition which has shown good agreement with the simulated time-histories of the different radicals that are often used with emission-based measurements (OH*, CH*).

3.4 Shock tube facility at DLR

Experiments for water addition were performed at a secondary facility at the Deutsches Zentrum für Luft- und Raumfahrt in Stuttgart, Germany (DLR). The shock tube used in the experiments at DLR had an internal diameter of 4.60 cm. The shock tube was evacuated between each experiment using a turbo molecular vacuum pump. The gaseous mixtures mixed several nights before use except at the highest water load where every mixture was prepared by water injection followed by 15 minutes stirring before each shock. The partial pressure method was used to determine the composition of each mixture. All gases used for the experiments were lab grade gases (>99.999%

purity). The driven section of the shock tube was kept at a constant temperature of 160 ºC and the driver section was kept at 120 ºC throughout the experiments. More details on the high pressure shock tube at DLR can be found here [46].

Ignition delay times were measured using a Hamamatsu R3896 photomultiplier tube with a 431-nm filter to isolate the CH* emission and amplified by a FEMTO HLVA-100 logarithmic amplifier. The pressure was measured using a Kistler 603B pressure transducer with an RTV106 coating to eliminate thermal shock to the transducer. Both devices were located 1 cm from the end wall. In addition to the radial measurements, axial emission was detected spectrally resolved to 5 wavelengths (310 nm, 375 nm, 430 nm, 476 nm and 516nm; FWHM = 5nm) through a sapphire window in the end wall.

CHAPTER 4: FLUID DYNAMICS OF CO_2 ADDITION

The fluid dynamics inside a shock tube are generally considered to be minimal in a typical mixture diluted in argon. The region behind the reflected shock wave stagnates as the system comes to rest behind the moving shock wave. As result of the heavily diluted mixture, the specific heat of the mixture is relatively constant and the difference between the temperature in the boundary layer and the core flow region does not have a major impact on the flow. The specific heat capacity of carbon dioxide has a strong is strongly dependent on temperature (Figure 5). Therefore, an energy balance is created between the boundary layer and the core flow and a phenomenon known as bifurcation occurs. In previous experiments where the gas mixtures were diluted with CO_2 [39, 47], the ignition delay time for the system was measured by combining the pressure trace of the system with the sidewall emission trace. The pressure trace was used to measure the time-zero while the emission of light was used to signify the ignition delay time.

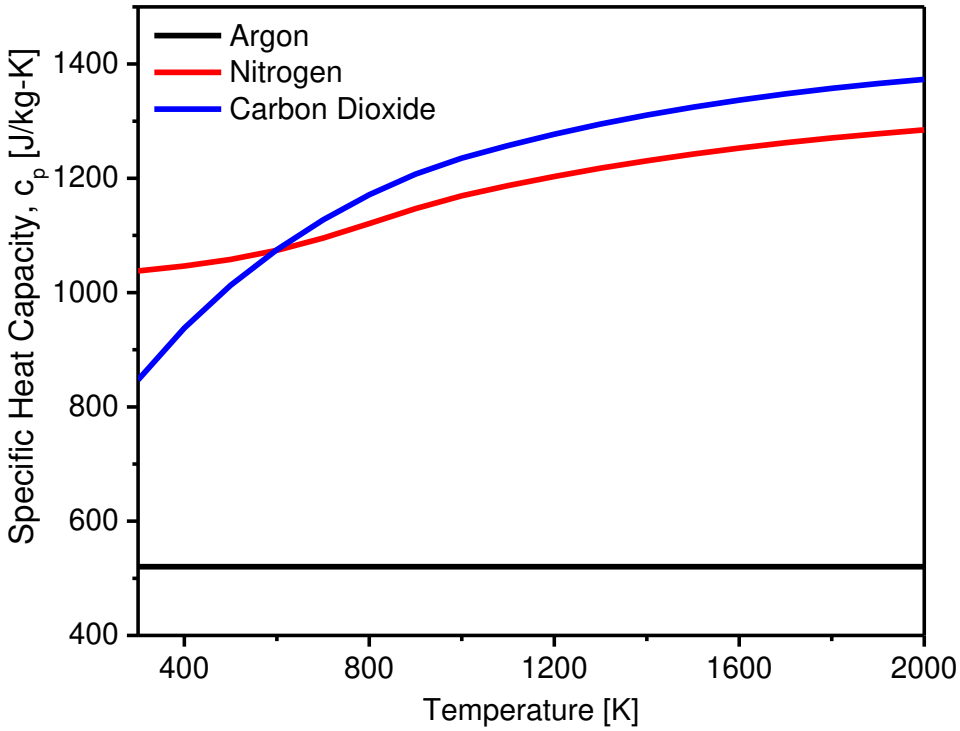

Figure 5: Comparison of the specific heat capacities of three different gases. Specific heat capacities calculated using the database provided by Burcat and Ruscic [48].

4.1 Fluid dynamics and bifurcation of the shock wave

Bifurcation is the phenomenon that occurs when the normal shock wave splits into counter-facing oblique shock waves inside of the boundary layer. For a mixture with diatomic and monoatomic compounds, such as the CO_2 diluted mixtures present in this system, the shock wave splits in the boundary layer into two oblique waves [49] as shown in Figure 6. Bifurcation is a major concern for the experiments presented above and leads to uncertainty in the experiments. When the shock wave reflects from the end wall, the normal shock wave splits due to the boundary layer forming two opposing oblique shocks, or a lambda wave. The lambda wave is formed due to the boundary

layer separating from the end wall. This phenomenon occurs primarily due to the lack of momentum in the boundary layer to pass through the normal shock wave as described by Mark [18].

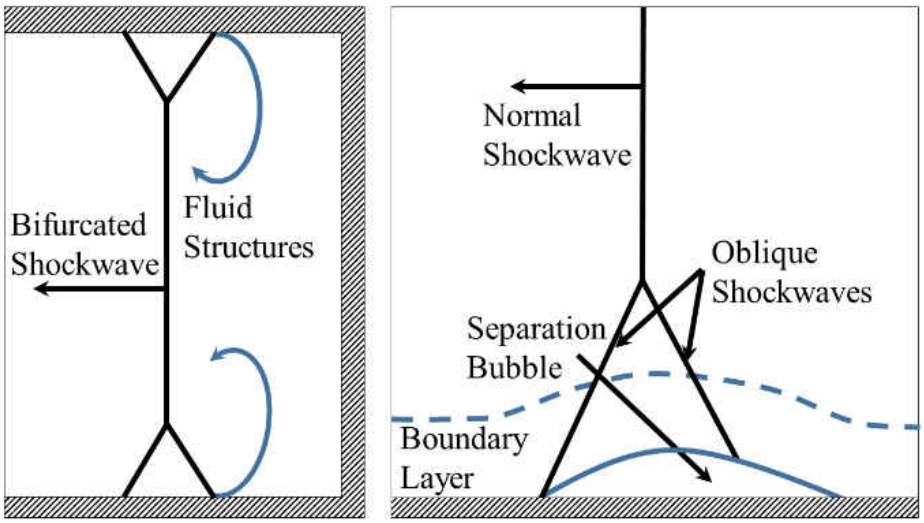

Figure 6: Representation of the bifurcation of the reflected shock wave in CO_2 diluted experiments.

The effects of bifurcation have been well documented from many different studies [22, 28, 50-55]. The main effects of bifurcation in carbon dioxide mixtures were also explained by Hargis and Petersen [56]. These works explained the non-steady conditions that are often seen in the reflected shock region and how temperature, pressure and mixture composition effect the experiment. One major concern that is described by Nowak et al., is the formation of hot spots near the wall [55]. These events that are caused by the swirling turbulence of the oblique shock waves can cause early and heterogeneous ignition resulting in a poor understanding of the shock conditions before ignition. This is also a concern for longer ignition experiments as the test conditions present become increasingly unstable and early ignition more likely.

Another concern with bifurcation is that the pressure rise no longer occurs in a continuous and uniform manner. Due to passing through two oblique shock waves, the sidewall pressure trace shows that pressure jump occurs in two-steps rather than a single smooth jump from the incident to the reflected shock conditions.

The time-zero calculation is also affected by the bifurcation. Traditionally, time-zero is measured by taking the midpoint of the reflected pressure jump but because of the non-uniformity, the pressure jump occurs over a significantly longer period. An alternative for time-zero was used for these experiments by utilizing the maximum of the schlieren peak that occurs from the beam steering of the 3.4 μm laser. The beam steering is minimally affected by the bifurcation event due to the laser passing through the shock tube rather than only measuring inside of the bifurcation region. Figure 7 shows an experiment with 89.5% CO_2 and the effect of bifurcation on the shock wave. Time-zero as defined by the pressure rise, $t_{o,p}$ was 34 μs after the schlieren peak created by the passing shock wave. The method of using a continuous wave laser to locate the time zero was first suggested in Petersen and Hanson [49].

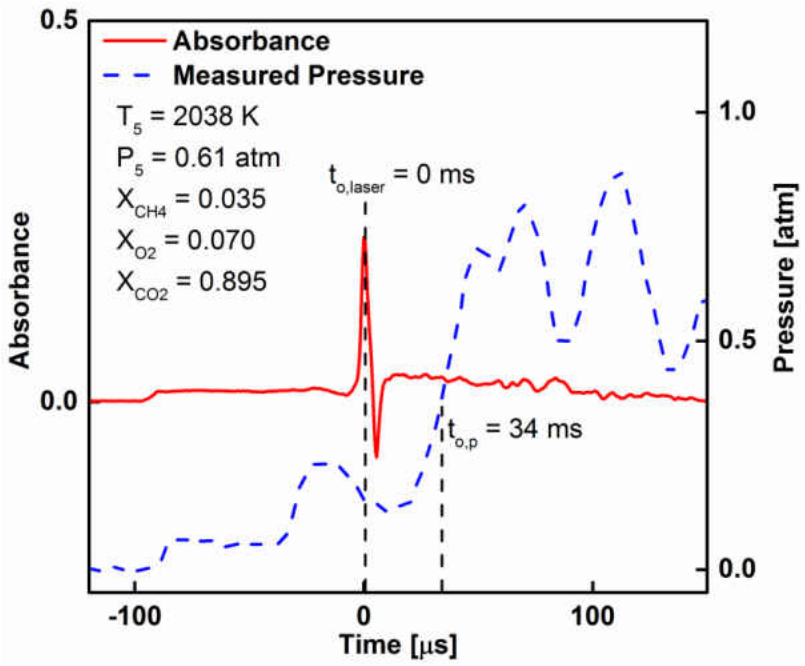

Figure 7: Example of time-zero for a bifurcated shock wave. Time-zero as defined by the pressure rise, $t_{o,p}$ was 34 μs after the schlieren peak created by the passing shock wave.

4.2 High-speed chemiluminescence visualization and image processing

To understand the fluid dynamics of bifurcation on the experiments, high-speed camera images were taken of the test-section cross-sectional area. The images were recorded at a rate of 67,065 fps with a resolution of 256 x 256 pixels. All images were post-processed in MATLab. The time-zero image was determined by matching the 3.4 μm laser schlieren spike to the time when the pressure trace reached 2 V as the camera was triggered directly from the pressure trace. The pixel intensity was calculated for each image and each experimental image set was normalized to the brightest pixel at the emission peak. The cumulative pixel was also determined to compare the emission recorded by the camera to the normalized light from the emission detector. Finally, a

color map was superimposed on each image to convert the high-speed camera images to artificial color to better distinguish between individual images.

An example of an experiment with the high-speed camera is seen in Figure 8. The vertical black lines denote the time location of each image in the subset. As shown below, the normalized pixel intensity correlates extremely well with the side-wall emission. A circle has been artificially drawn on the image to denote the interior wall of the shock tube.

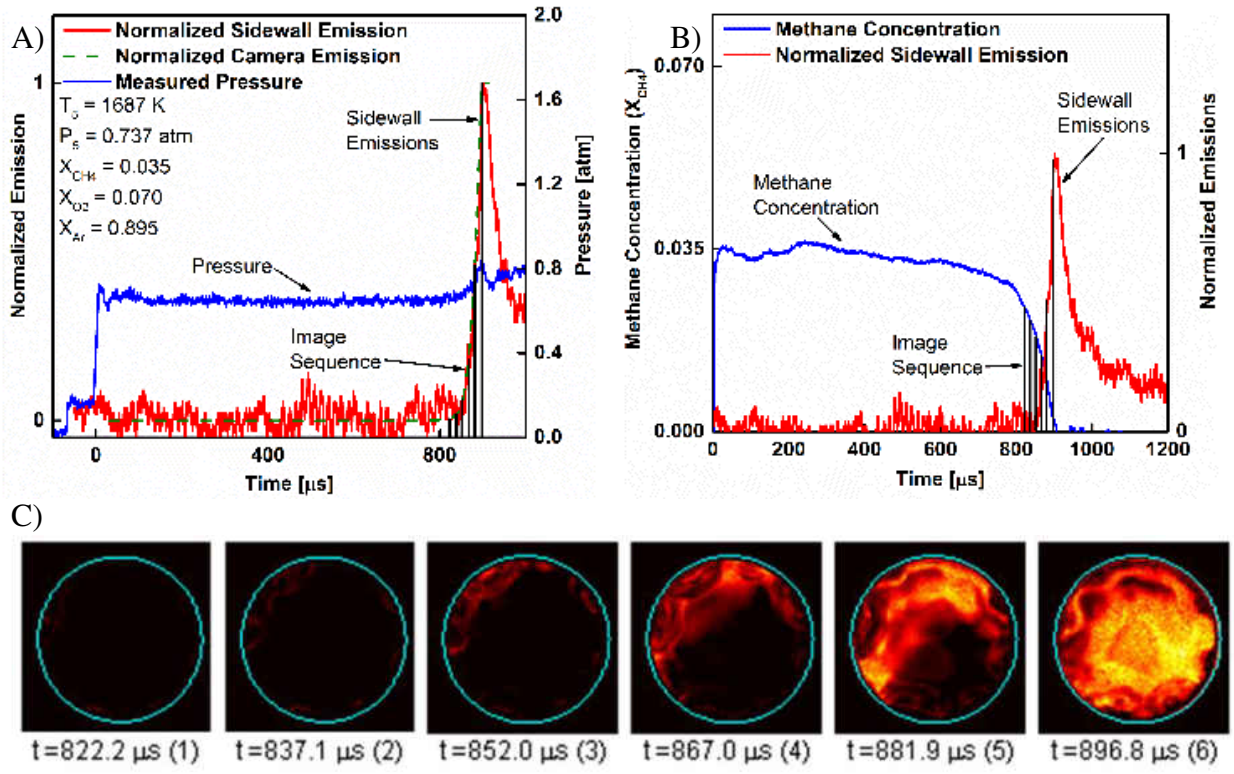

Figure 8: Comparison of images taken at the end wall to the pressure, sidewall emission and methane time-history. (A) Pressure and emission trace for argon dilution with the images from (C) seen are depicted as black lines. (B) Methane time-history and emission trace compared to high-speed camera images. (C) High-speed camera images at a temperature of 1687 K. Vertical black lines (in A, B) show time instances corresponding to images.

4.3 Fluid Dynamic effects on ignition delay times

Ignition delay times are an important parameter for understanding the global reactivity of a fuel mixture. The addition of carbon dioxide results in fluid dynamic effects that need to be better understood and how they affect the ignition delay times during combustion. These effects are seen largely by looking at different definitions of ignition delay times from different sensors and comparing them across different mixtures over a range of various levels of carbon dioxide dilution.

The ignition delay times were measured for four different mixtures using a total of six different techniques. Three methods were taken from the emission detection system and allow us to look at the width of the emission profile for each experiment. These methods include the location of the peak of the emission trace and the midpoint of the emission peak from the baseline. The last method is tracing a tangent line from the maximum rise in the emission signal back to the baseline of the signal. These three methods examined how the emission profile changed with adding carbon dioxide to the system and give evidence to the impact of non-combustion dynamics on the system. The remaining three methods are taken from other systems that have been shown to match well with traditional ignition delay time measurements taken from emission profiles. In Koroglu et al., the methane decay time was defined as the time taken for methane to reach $1/3^{rd}$ of its initial value in the mixture and was shown to correlate extremely well with the ignition delay times taken from emission [33]. Pressure increase is also an indicator of combustion because of the energy released during the process. The ignition delay time based on the pressure was defined as the time of the peak pressure after the arrival of the reflected shock wave. For the mixtures with carbon dioxide dilution, a pressure rise was not observed during the combustion process and therefore this method

is only applicable to the baseline experiments. The last method was to look at the image intensity of the high-speed camera images and to trace back to the baseline where the tangent line of the maximum rise in the images crosses. The experimental data is compared in Table 1 for all for mixtures and the various methods.

The data in the table shows that with the addition of carbon dioxide the emission profile is significantly broadened compared to Argon as the only diluent. An analysis was performed on the emission profile by comparing the difference in the peak of the emission profile to the baseline measurement normalized by the peak measurement. The first mixture shows that the difference between the peak and baseline of the emission profile varied by 5% of the peak value but with the addition of CO_2 the baseline occurred a minimum of 17% earlier than the peak and as much was up to 50% of the peak value at the highest temperatures. The difference in ignition delay times was also variant with respect to temperature. Mixture 1 had a standard deviation of around 0.6% of the 4.9% average but when argon was completely replaced by carbon dioxide (Mixture 4), the standard deviation of the mixture increased to 11.9% of an average value of 31.5%. The changes in the emission profile show that other physical aspects of the experiment are changing besides the combustion dynamics of the system.

Table 1: Summary of ignition delay times based on different methods of evaluation. Ignition delay time based on the pressure rise could only be determined for mixture 1 due to the small pressure rise for the carbon dioxide diluted mixtures.

Mixture	T5 [K]	Emis. Peak [µs]	Emis. ½ Peak [µs]	Emis. Slope [µs]	Laser [µs]	Press. [µs]	Camera [µs]	Δt [µs]
1	1672	1021.5	998.5	969.5	1022	1003	976.5	52.5
	1687	902.5	886.5	866	905.5	897.5	867	39.5
	1749	644.5	626.5	609	656.5	645.5	591	65.5
	1770	469	456.5	445	485	477	442	43
2	1750	504	455	409	516	n/a	461.5	107
	1797	309	265	212.5	301		254	96.5
	1920	172.5	155	135	166.5		166	37.5
3	2038	140	103	70	142	n/a	95	72
4	1724	503	448	396	536.5	n/a	440	140.5
	1726	400	364.5	325.5	424.5		374	99
	1839	236	195.5	150.5	259.5		209.5	109
	1874	205.5	170	137	182		167.5	68.5
	1951	156	116.5	81	114.5		128	75

This can be further shown by plotting the different methods onto one graph (Figure 9). Figure 9 shows the ignition delay times for Mixture 1 and 2 for a direct comparison. By calculating the range of ignition delay times calculated for each mixture, it shows that the range of ignition delay time values increased by over 50% when 60% carbon dioxide was added to the mixture from 50 µs to an average of 80 µs.

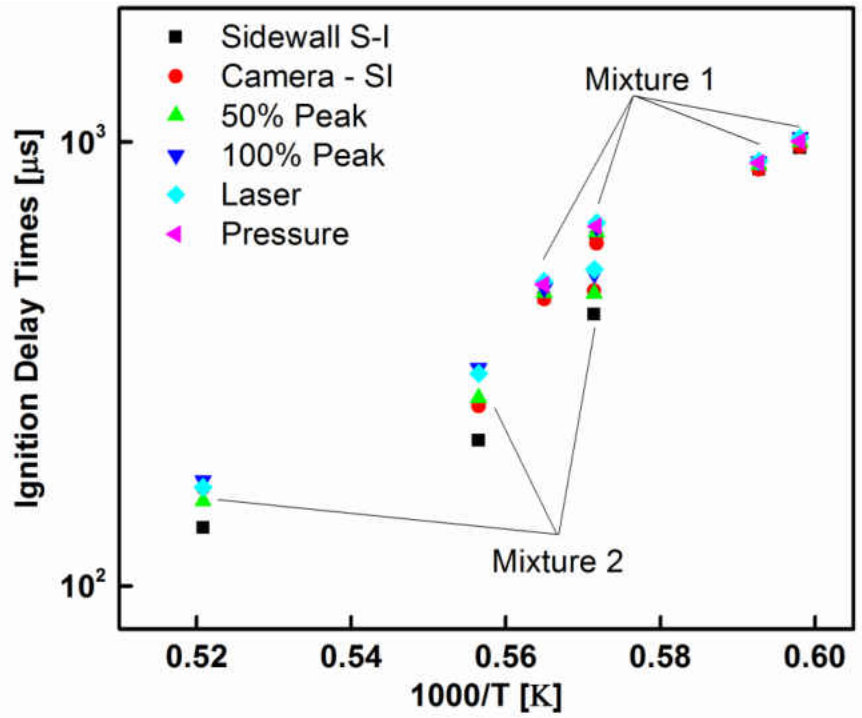

Figure 9: Comparison of different ignition delay time methods for two mixtures. Mixture 1: X_{CH4} = 0.035, X_{O2} = 0.07, X_{CO2} = 0.00, X_{Ar} = 0.895. Mixture 2: X_{CH4} = 0.035, X_{O2} = 0.07, X_{CO2} = 0.60, X_{Ar} = 0.295.

4.4 Experiments without CO_2 addition

The fluid dynamics of methane oxidation diluted in argon was examined using high-speed camera imaging behind reflected shock waves. These experiments served as a baseline for the experiments, so a direct comparison could be made with the addition of carbon dioxide to the system. The ignition event started around the edge of the shock tube, probably at the location of one of the different plugs in the test section which has been shown to be the start of combustion [42]. Figure 10 shows the combustion process of all the experiments in argon dilution. The figure clearly shows that the entire sequence can be captured in less than 100 µs and that at the location of peak emission

(sixth image shown for each experiment), the shock tube has completely ignited the cross-sectional area.

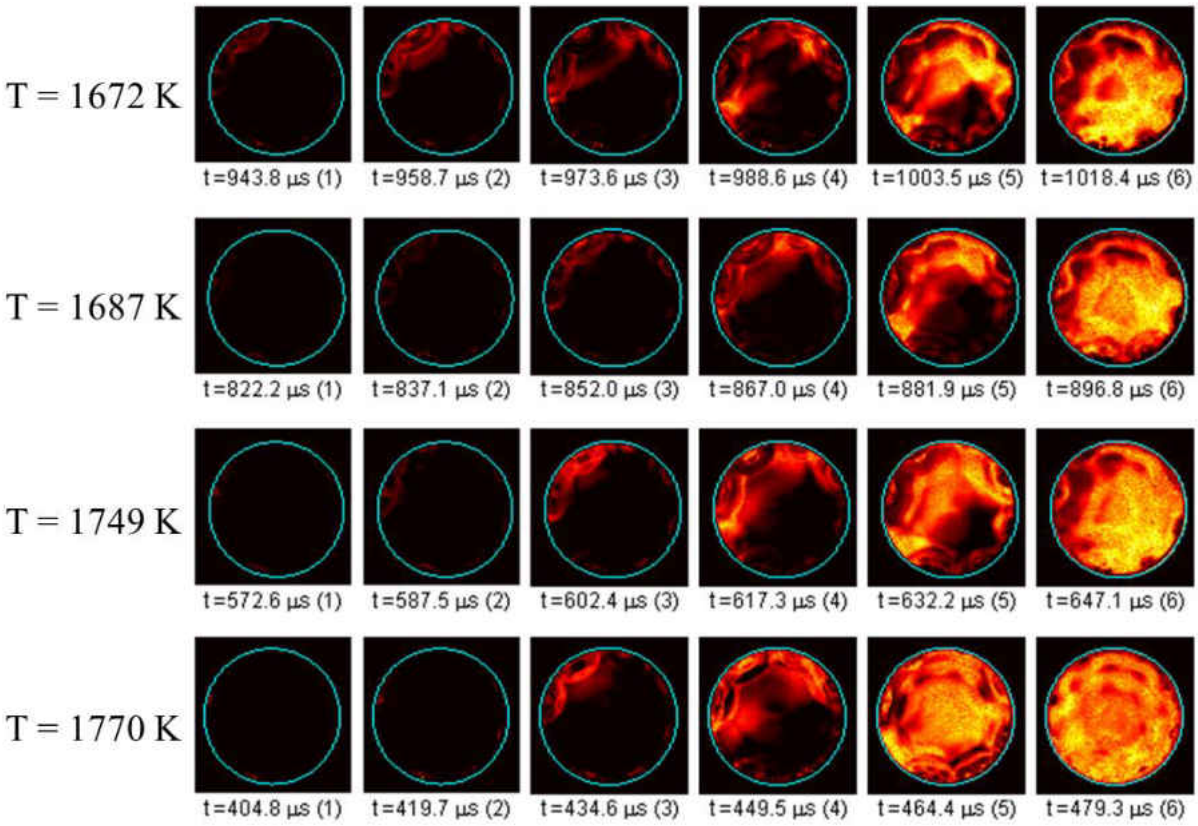

Figure 10: Comparison of high-speed camera images for different temperatures during argon-diluted methane combustion. All intensities were normalized to the highest pixel intensity of the last image for each individual run.

Examining all the runs, several assertions about the mixture can be made. Each of the experiments had the combustion process occur over a brief time. The initial stages of ignition occurred slowly with a small portion of the cross-section showing light emission within the first three images. By the sixth image (75 µs after the first image), the ignition process covered the entire shock tube cross-section apart from small vacant areas which closely track with the location of the plugs in the test section.

4.5 Experiments with CO_2 dilution

The addition of CO_2 was previously shown to increase the ignition delay times from the participation of carbon dioxide in the combustion process [33]. Other work had discussed the influence of bifurcation on the experimental results [56]. The addition of carbon dioxide has been shown to reduce the emission of light and reduce the pressure rise of combustion as carbon dioxide has a higher specific heat capacity than argon. This section presents high-camera imaging of the cross-sectional area of the shock tube for various levels of carbon dioxide dilution.

The most noticeable thing that was noticed with the addition of carbon dioxide was the reduced emission of light in both the sidewall and the high-speed imaging. Despite this reduction in the signal, the ignition delay time is still well represented by the rise in emission in the high-speed camera images as seen in Figure 11.

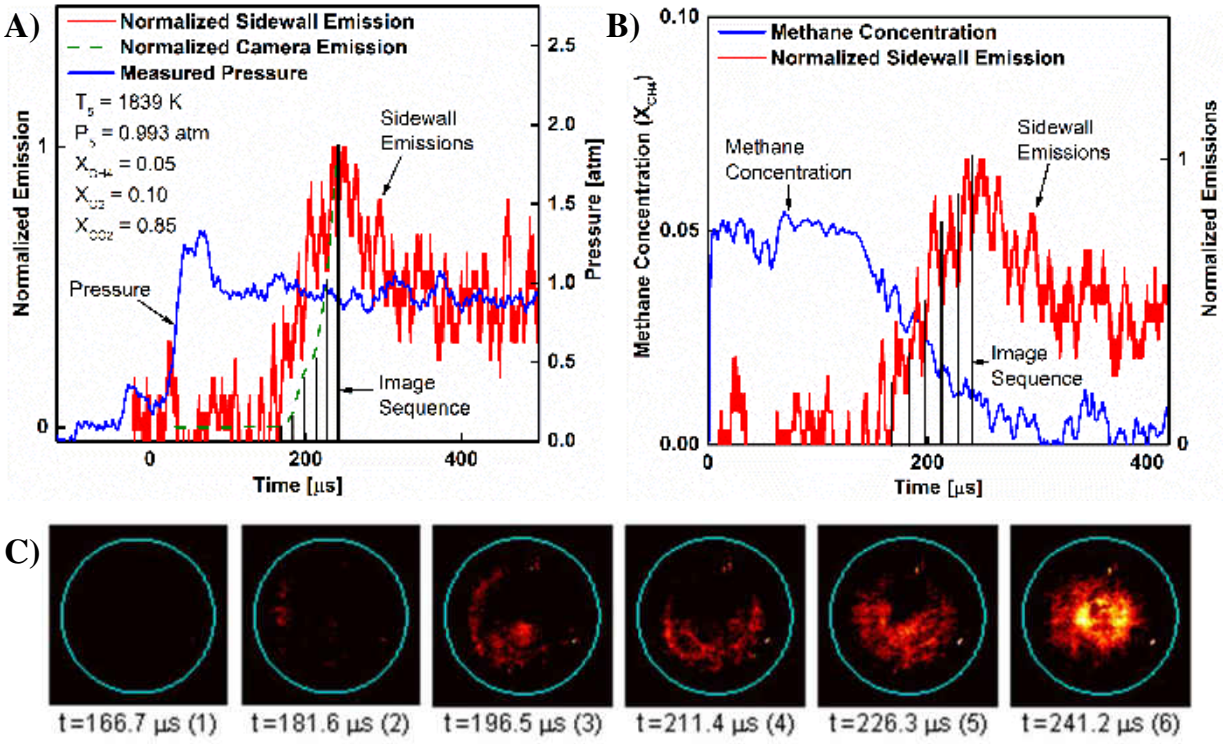

Figure 11: Experimental pressure and emission trace compared to the high-speed camera images. Black vertical lines represent the time location for each of the images. (A) Pressure and emission trace for 85% carbon dioxide dilution with the images from (C) seen are depicted as black lines. (B) Methane time-history and emission trace compared to high-speed camera images. (C) High-speed camera images at a temperature of 1839 K. Vertical black lines (in A, B) show time instances corresponding to images.

The ignition delay times are to be predicted by the camera emission, but Figure 11 also demonstrates that the carbon dioxide fundamentally changed the combustion process. The area that shows visible ignition has been greatly reduced compared to previous experiments. The area that ignition was visible was calculated and compared to the cross-sectional area of the shock tube. This ratio, called the Ignition Area Ratio, is presented in Table 2. The ratio was calculated by approximating the light emission as a circle and dividing the area by the known area of the shock tube highlighted by the circle. The addition of carbon dioxide had several effects on the ignition process. The first is that CO_2 addition resulted in smaller areas of visible ignition, decreasing from

near 100% of the shock tube ignited in argon dilution to an average of 40% of the shock tube showing visible ignition. One interesting note is that temperature appeared to have no relationship to the size of the area ratio as direct comparisons can be made across all three conditions around 1725-1750 K. This comparison shows that we had approximately a 30% reduction in the area that was visibly ignited with the first 60% of CO_2 and a further 30-40% reduction when argon was completely replaced with carbon dioxide.

Table 2: Ratio of the area of visible light emission to the cross-sectional area of the shock tube. Ignition area was assumed to be circular and be the maximum extent of the flame as determined by the high-speed imaging.

CO_2 %	P_5 [atm]	T_5 [K]	Ignition Area Ratio
0	0.780	1672	0.984
	0.756	1687	0.953
	0.625	1749	1.000
	0.737	1770	0.984
60	0.944	1750	0.712
	0.866	1797	0.710
	0.833	1920	0.806
85	1.093	1724	0.288
	1.043	1726	0.389
	0.993	1839	0.484
	0.946	1874	0.410
	0.919	1951	0.452

Another difference was the shape of the captured event. The argon diluted experiments all followed the same trends, starting in the upper left of the image before igniting across the entire cross-section. When CO_2 was added to the system, the shape was less uniformly consistent as the temperature varied. Figure 12 shows the ignition process for the experiments with 60% CO_2 (Mixture 2). Comparing the images that correspond to the peak of the sidewall emission signal,

the first experiment at 1750 K show an ignition event with the strongest emission at the bottom of the shock tube when the other experiments show a more complete central ignition event with large vacant regions above the center.

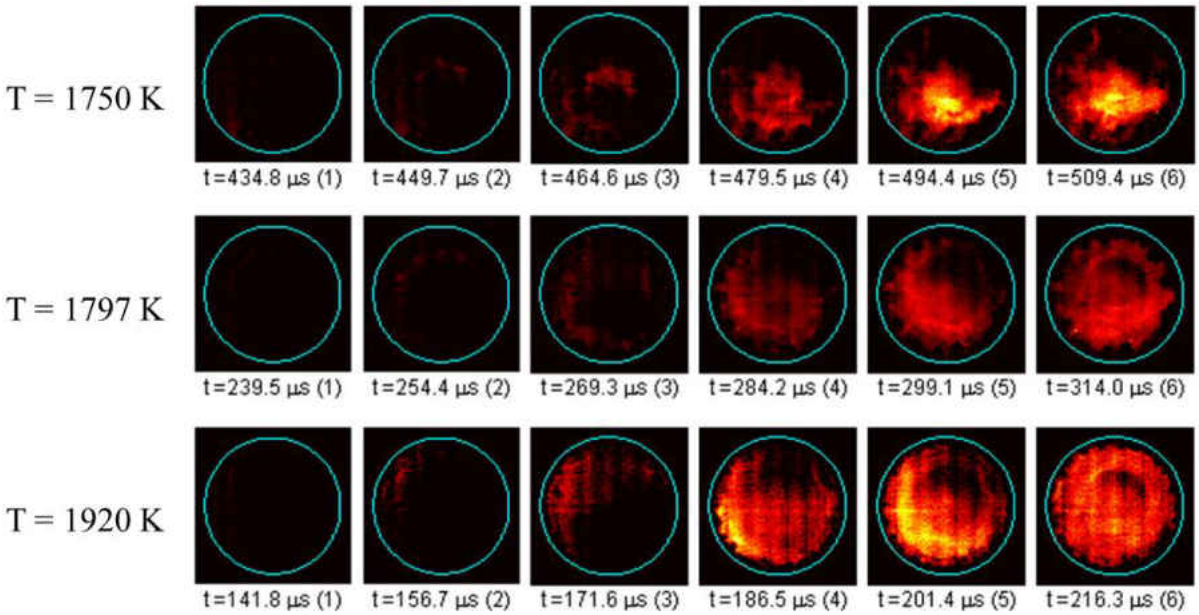

Figure 12: Comparison of high-speed camera images for different temperatures of 60% carbon dioxide dilution. All intensities were normalized to the highest pixel intensity of the last image for each individual run.

The same trend was even more noticeable when the carbon dioxide concentration was further increased to 85% of the total mixture. The variation in the area ratio increased to around 20% compared to 9% for the second mixture and less than 5% for the baseline experiments. This trend is explained because of the bifurcation of the normal shock wave in the boundary layer. As the temperature in the boundary layer of the shock tube must approach the temperature of the room (approximately 300 K) as it gets closer to the inside wall of the shock tube, the specific heat capacity of the mixture would be greatly reduced compared to the core region (see Figure 5).

The effect of carbon dioxide was clearly shown when high-speed imaging was added to the system. The general trend of CO_2 addition was shown in previous research [33, 56]. The issue is that traditional diagnostics have been shown to be susceptible to increasing levels of noise due to bifurcation. As the heterogeneity of the experiments increased, the camera was able to identify additional information that was not previously known. The argon diluted mixture demonstrated consistent results in the size and shape of the ignited area but as shown in Figure 13, the addition of carbon dioxide caused several different effects in the visible light emission. The increased uncertainty in the combustion event could result in unaccounted for errors when comparing to simulations that assume homogeneous ignition with no fluid dynamic effects. The reason for the discrepancy is that bifurcation results in large zones of circulation as the bifurcated shock wave moves away from the test section [29]. In a typical shock tube experiment, the region behind the reflected shock wave is considered stagnant but the bifurcated shock wave causes non-homogeneous temperature and pressure across the cross-section as described by Grogan and Ihme [29].

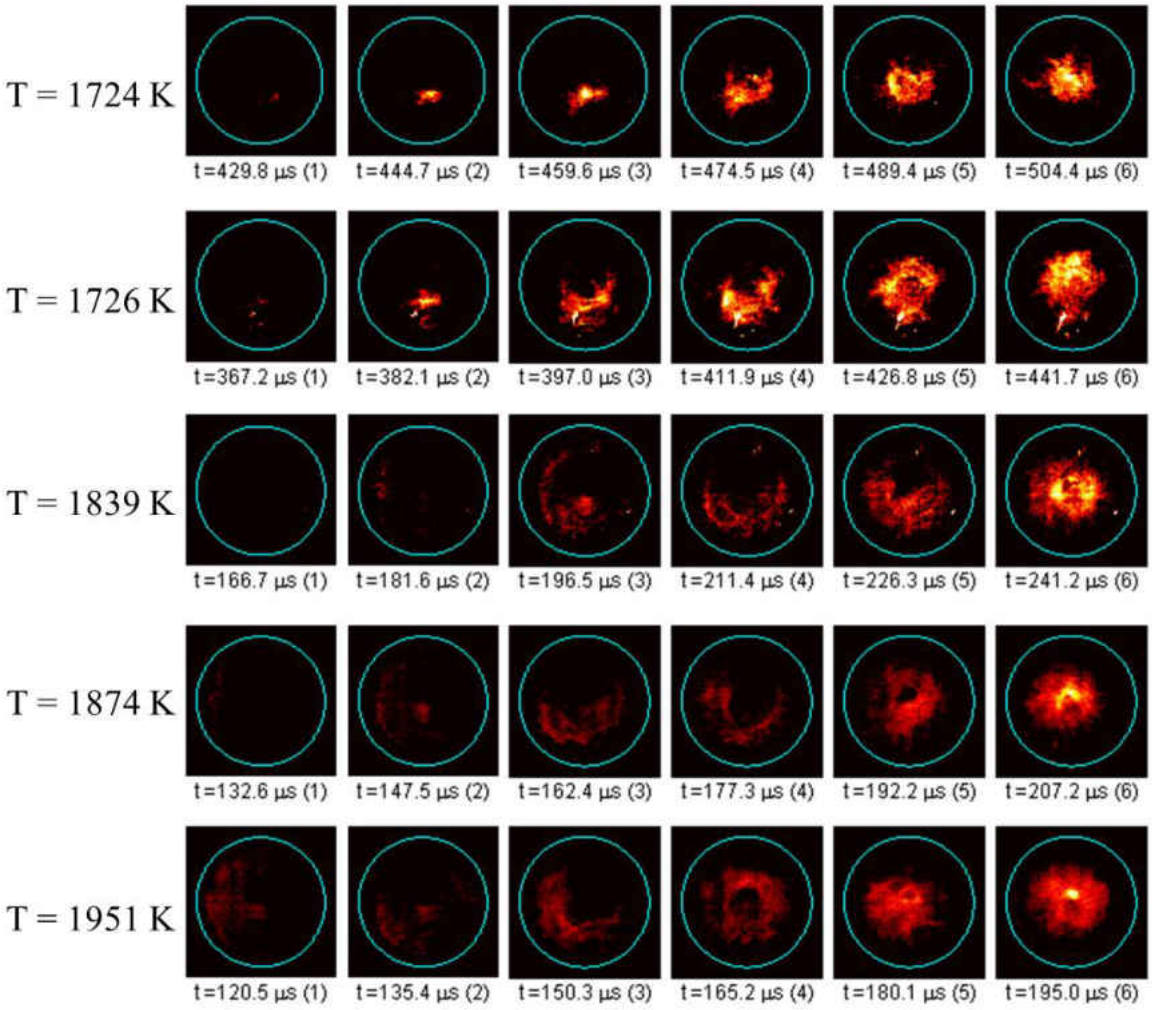

Figure 13: Experimental Images for 85% carbon dioxide dilution. This mixture shows that the flame forms in the center of the shock tube and that the edges do not ignite during the combustion process as it did for the argon diluted mixture.

Another theory about the reduction in light emission comes from the theory of flameless combustion [8, 57]. In a situation with flameless combustion, the cross-section would have ignited but light emission would have been below the threshold to be recorded by the camera. This would be consistent with laser ignition experiments that show complete oxidation of the fuel, but flameless combustion has been shown to increase homogeneity in the system. Research on

flameless combustion has shown that the temperature and luminosity are homogeneous across the reactor [57-60]. If the temperature distribution had been uniform as expected in a flameless combustion scenario, the visible ignition event most likely would have been uniform across the entire cross-section and not centered in the shock tube as has been shown for each of the CO_2 diluted mixtures.

Bifurcation has been observed in shock tube experiments in many different studies [20-22, 28, 50, 54, 56, 61, 62]. Hargis and Petersen described the effects of carbon dioxide addition and how altering the temperature, pressure and mixture composition affected the ignition delay times. By examining the length of time of the bifurcated foot, Hargis and Petersen were able to observe that the increasing CO_2 mole fraction resulted in longer bifurcation times regardless of both pressure and temperature [56]. Another concern is the formation of hot spots at the separation point in the boundary layer. Nowak et al. raised the concern that these hot spots could cause localized temperature and pressure increases which would result in shorter ignition delay times and therefore heterogeneous combustion [62]. Grogan and Ihme further showed that experiments with higher Mach numbers increased both the attenuation and the inhomogeneity in the cross-sectional area [29]. Carbon dioxide experiments have higher Mach numbers resulting from the higher heat capacity compared to argon adds to the increasing issue of bifurcation as carbon dioxide is added to the mixture.

Bifurcation is the main theory for the variation between the different definitions of ignition delay time. The reduction in signal which leads to the large uncertainty in the experiments is most likely caused by the bifurcation and non-ideal flame structure that is present in the bifurcated shock

waves. Based on the images, bifurcation does not cause the system to ignite early but does play a factor in the homogeneity of the combustion process. The system does not ignite on or around the edge where the boundary layer has formed. The boundary layer keeps the system cool enough that it remains unburnt despite the flame in the center of the system for every run tested with CO_2 dilution. This unburnt ring also grows with increasing concentrations of CO_2. At the smaller concentration, the ring was small and most of the cross-section burned during the combustion process but with 85% CO_2, the flame only filled about half the cross section, despite the fuel and oxidizer concentrations being increased for these experiments. One possible concern with the flame area ratio described earlier was that the bifurcation was creating cold spots and the flame denoted the size of the bifurcation region. Using a correlation developed by Petersen et al, it was determined that the size of the bifurcation was on a similar scale for the experiments and that it did not correspond to the difference in the average flame area ratio between the mixtures [49]. The flame area ratio deviated by up to 44% between Mixtures 2 – 4 but the bifurcation area only differed by approximately 7%.

CHAPTER 5: IGNITION DELAY TIMES OF NATURAL GAS SURROGATES

Ignition delay times represent one of the fundamental fuel properties for oxidation of a given mixture. The property represents one of the basic time-scales that can be used to investigate new combustor designs and provide valuable target data for creating and validating chemical kinetic mechanisms. This chapter presents the ignition delay times of several different natural gas surrogates to understand how different fuels and conditions affect the ignition delay times.

5.1 Ignition delay times in methane

Natural gas is made up primarily of methane. Methane is one of the simplest hydrocarbon fuels and understanding how ignition delay times of methane are affected with the addition of carbon dioxide is important for developing a chemical kinetic mechanism for supercritical carbon dioxide. Experiments were performed over five different mixtures to cover a range of different conditions at near atmospheric conditions. Table 3 and Table 4 show the experiments and the ignition delay times for methane oxidation experiments with and without carbon dioxide dilution, respectively. These different experiments represent a continuation of previous work to fill out more conditions from Koroglu et al [33]. The experimental conditions cover methane concentrations from 1.0% to 5.0%, oxygen concentrations from 1.0% to 10.0% and carbon dioxide concentrations between 0.0% to 85.0%.

Table 3: Summary of low pressure ignition delay time experiments without carbon dioxide dilution.

P_5 [atm]	T_5 [K]	X_{CO2}	X_{CH4}	X_{O2}	X_{Ar}	τ_{ign} [µs]
1.33	1975	0.0%	1.0%	2.0%	97.0%	182.5
1.38	1929					280.5
1.40	1882					330.0
1.43	1845					477.5
1.45	1792					604.5
1.48	1746					900.0
1.51	1693					1219.5
1.52	1630					1847.5
1.57	1603					2063.0
1.27	2083	0.0%	1.0%	1.0%	98.0%	212.5
1.31	2030					274.0
1.22	1998					272.0
1.38	1993					353.0
1.24	1956					407.0
1.27	1949					440.0
1.27	1894					589.5
1.31	1868					700.5
1.39	1822					925.5
1.39	1819					967.0
1.34	1813					1088.5
1.29	1801					1024.0
1.43	1795					1126.5
1.41	1755					1482.0
1.34	1720					1693.0
1.43	1712					2108.5
1.38	1678					2317.5
1.32	1613					3107.0

Table 4: Summary of low pressure ignition delay time experiments with various levels of carbon dioxide dilution.

P_5 [atm]	T_5 [K]	X_{CO2}	X_{CH4}	X_{O2}	X_{Ar}	τ_{ign} [µs]
0.78	1672	0.0%	3.5%	7.0%	89.5%	1021.5
0.76	1687					902.5
0.63	1749					644.5
0.74	1770					469.0
0.94	1750	60.0%	3.5%	7.0%	29.5%	504.0
0.87	1797					309.0
0.83	1920					172.5
1.09	1724	85.0%	5.0%	10.0%	0.0%	503.0
1.04	1726					400.0
0.99	1839					236.0
0.95	1874					205.5
0.92	1951					156.0

The ignition delay time experiments were compared to different detailed chemical kinetic mechanisms. At the conditions presented, the ignition delay times show good agreement with the Aramco 2.0 mechanism and the GRI 3.0 mechanism [44, 45]. Figure 13 shows that the ignition delay times are well predicted by the Aramco 2.0 mechanism when carbon dioxide is not added to the system as was expected by the system. The main difference between the mechanism and the experimental data is that the experimental data is unable to match the simulations at the lowest temperatures tested. At temperatures starting around 1700 K, the mechanism starts to rise at a greater rate than the experiments.

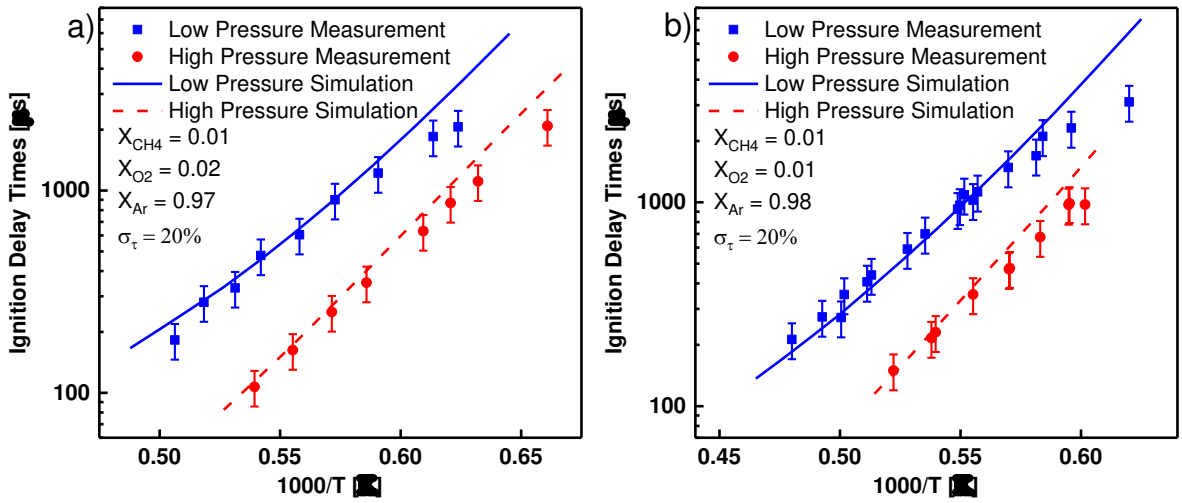

Figure 14: Ignition delay times for methane combustion compared to the Aramco 2.0 mechanism. A) Stoichiometric conditions, mixture: X_{CH4} = 1.0%, X_{O2} = 2.0%, X_{Ar} = 97.0%. B) Rich conditions, mixture: X_{CH4} = 1.0%, X_{O2} = 1.0%, X_{Ar} = 98.0%. Uncertainty for all experiments was estimated to be 20%.

The addition of carbon dioxide was well predicted by both the Aramco and the GRI mechanisms. Both mechanisms predicted a slight increase in the ignition delay times at the lower temperatures but the experimental data shows that any change was within the uncertainty of the experiments. The global reactivity of oxy-methane combustion is well predicted by current mechanisms available in the literature. The experimental data is compared to the mechanisms for atmospheric pressures in Figure 15 below.

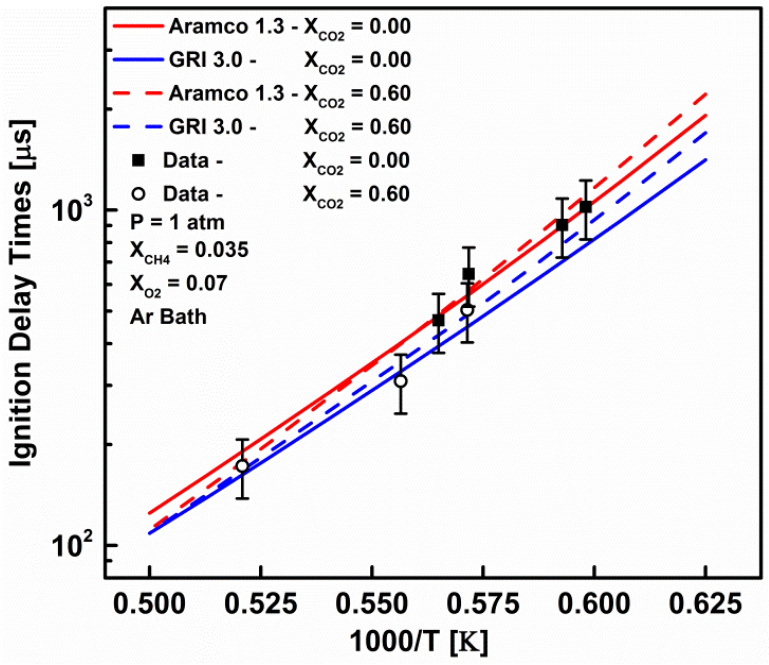

Figure 15: Effect of carbon dioxide on the ignition delay time measurements. Mixture 1: X_{CH4} = 3.5%, X_{O2} = 7.0%, X_{CO2} 0.0%, X_{Ar} = 89.5%, mixture 2: X_{CH4} = 3.5%, X_{O2} = 7.0%, X_{CO2} 60.0%, X_{Ar} = 29.5%. Uncertainty for all experiments was estimated to be 20%.

The ignition delay times were also measured at elevated pressures up to 30 atm. Pressure has been shown to have a large effect on the ignition delay times of different fuels. To understand how pressure effected the ignition delay times, five mixtures were examined at pressures ranging from 6 atm to 30 atm. Table 5 and Table 6 show the ignition delay times at elevated pressures.

Table 5: Summary of ignition delay time experiments without carbon dioxide dilution at elevated pressures.

P_5 [atm]	T_5 [K]	X_{CO2}	X_{CH4}	X_{O2}	X_{Ar}	τ_{ign} [μs]
6.94	1854	0.0%	10.0%	20.0%	97.0%	107.0
7.22	1801					162.5
7.44	1750					251.0
7.59	1707					350.5
7.69	1641					630.5
7.83	1611					867.5
8.04	1582					1110.5
8.07	1513					2084.0
6.20	1915	0.0%	1.0%	1.0%	98.0%	149.5
6.46	1859					216.0
6.89	1853					230.5
6.68	1801					353.5
7.95	1754					470.0
8.99	1753					475.5
6.69	1715					675.5
7.01	1681					972.5
6.91	1680					988.5
9.22	1662					976.0
9.59	1485					4216.5

Table 6: Summary of ignition delay time experiments with various levels of carbon dioxide dilution at elevated pressures.

P_5 [atm]	T_5 [K]	X_{CO2}	X_{CH4}	X_{O2}	X_{Ar}	τ_{ign} [µs]
8.91	1521	30.0%	3.5%	7.0%	59.5%	702.0
8.85	1558					497.5
8.71	1625					274.5
9.02	1749					105.0
7.42	1568	60.0%	3.5%	7.0%	29.5%	598.0
7.43	1590					501.5
7.48	1636					309.5
6.87	1667					213.5
7.00	1725					151.5
6.97	1764					128.0
28.71	1334	85.0%	5.0%	10.0%	0.0%	1268.0
30.97	1484					312.0
29.24	1515					214.0

The same can also be said for the ignition delay times around 8 atm. Both mechanisms can predict the ignition delay times within the uncertainty of the experiments. This shows that within the pressure range of the original mechanisms validation range, the effect of CO_2 addition does not change the ability of the mechanisms in predicting the ignition delay times as shown in Figure 16. The addition of CO_2 from 0.3 to 0.6 mole fraction shows that the ignition delay time is further decreased compared to an argon baseline. This result shows that carbon dioxide is playing a weak role in slowing the ignition and this effect needs to be well understood for these experiments.

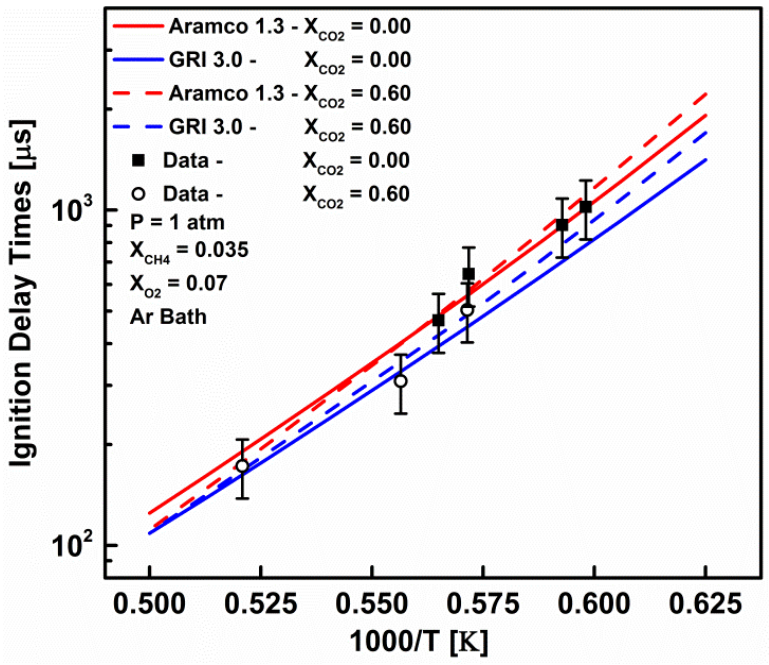

Figure 16: Effect of carbon dioxide on the ignition delay time measurements at elevated pressures. Mixture 1: X_{CH4} = 3.5%, X_{O2} = 7.0%, X_{CO2} = 0.0%, X_{Ar} = 89.5%, Mixture 2: X_{CH4} = 3.5%, X_{O2} = 7.0%, X_{CO2} 60.0%, X_{Ar} = 29.5%. Uncertainty for all experiments was estimated to be 20%.

The experiments at 30 atm differ much more from the GRI 3.0 mechanism predictions, while the Aramco 1.3 mechanism agreement is reasonably good. More data points are required to draw accurate conclusions on the accuracy of the mechanisms at 30 atm. Effort is underway in our laboratory to expand measurements at high pressures and for different fuel/O_2 equivalence ratios. The data for 30 atm experiments is shown in Figure 17.

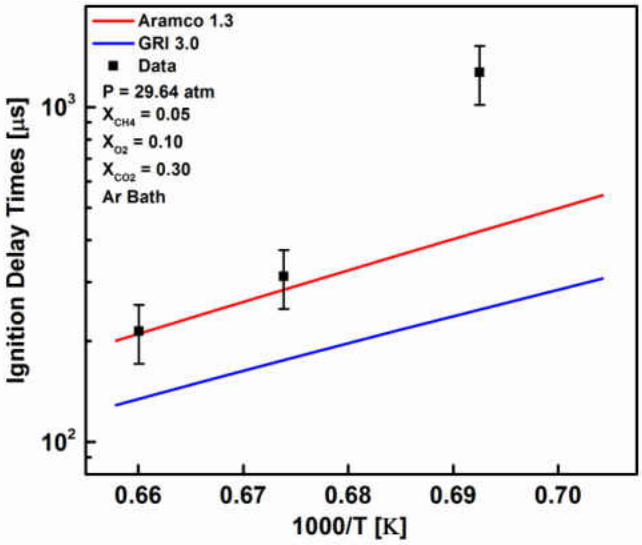

Figure 17: Ignition delay times for P ~ 30 atm compared to Aramco 1.3 (Red) and GRI 3.0 (Blue) mechanisms [44, 45].

The ignition delay times were combined with data from Koroglu et al. in order to create an equation for calculating the ignition delay time in the form of a modified Arrhenius Equation (8) [33]. The correlation developed is based on all the different parameters that have been modified within the two studies to include the effect of pressure, fuel concentration, equivalence ratio, temperature and carbon dioxide concentration. The correlation is applicable for the following conditions: T_5=1484-2114K, P_5=0.6-31atm, and X_{CO2}=0-85%. The correlation shows that the activation energy for these experiments is estimated to be 49.64 kcal/mol.

$$\tau = 7.51 \cdot 10^{-4} \cdot e^{\frac{40100}{RT}} \cdot P^{-0.52} \cdot \phi^{0.42} \cdot {\chi_{CH4}}^{0.72}(1 - \chi_{CO2})^{-0.55} \quad (8)$$

where the activation energy is in kcal/mol, temperature is in K, the pressure is in atm and τ_{ign} is in μs. The correlation can predict the ignition delay times over an extensive range of experimental conditions. The R^2 of the correlation was calculated to be 0.967 based on the parameters used.

Figure 18 compares the calculated ignition delay times based on the correlation compared to the ignition delay times.

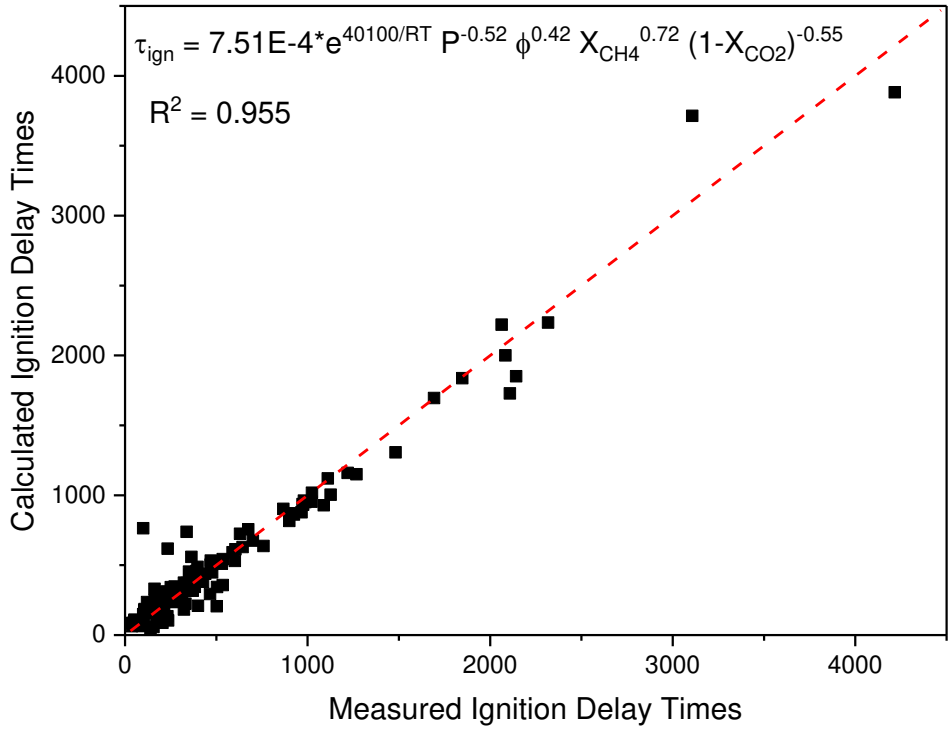

Figure 18: Ignition delay time correlation for methane oxidation. Data taken from this study and Koroglu et al. [33].

5.2 Ignition delay times in syngas

Experiments were performed in a mixture of $X_{CO} = 0.01$, $X_{H2} = 0.01$, and $X_{O2} = 0.01$ in an Argon bath ($X_{Ar} = 0.97$). Pre-combustion temperatures for these experiments ranged between ranged from 1034 to 1417 K for the low-pressure experiments. For the elevated pressures, the temperature ranged from 1067 to 1265 K. Table 7 shows the results from these experiments.

Table 7: Experimental results from syngas oxidation. X_{CO} = 0.01, X_{H2} = 0.01, X_{O2} = 0.01, X_{Ar} = 0.97.

Temperature [K]	**Pressure [atm]**	**τ_{ign} [µs]**
1417	1.50	266.5
1322	1.65	316.0
1290	1.64	394.0
1207	1.73	438.5
1117	1.77	655.5
1065	1.86	861.0
1034	2.10	1385.0
1265	8.73	94.0
1192	9.07	129.5
1120	9.38	268.5
1107	11.54	420.0
1067	9.73	1048.5

The ignition delay times were poorly predicted by the Aramco 2.0 mechanism at the extremes of the measured temperature range. The mechanism predicted a much larger increase below 1100 K than was measured at elevated pressures while the experimental data was underpredicted for the hotter experiments at atmospheric conditions. This shows that more work needs to be performed to understand how the combination of hydrogen and carbon monoxide burns. The experimental data is compared to the Aramco 2.0 mechanism in Figure 19.

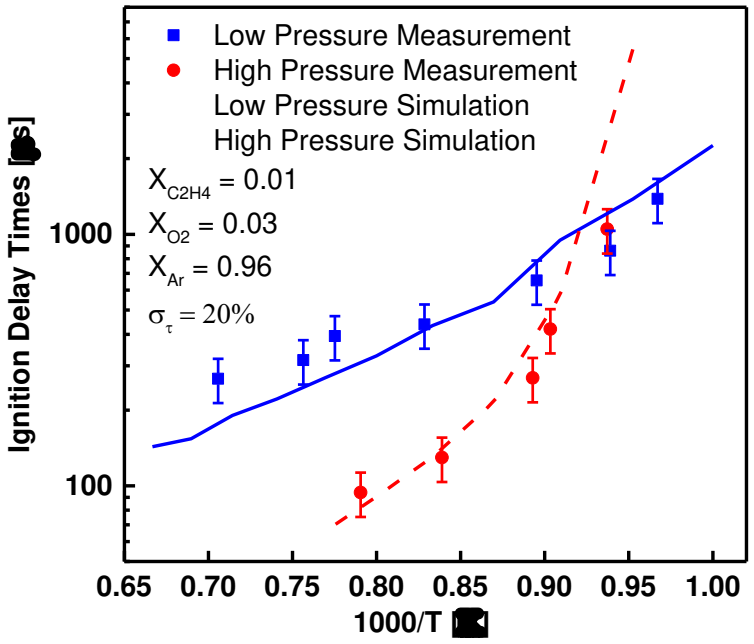

Figure 19: Ignition delay time measurements for syngas oxidation. Mixture was X_{CO} = 1%, X_{H2} = 1%, X_{O2} = 1% and X_{Ar} = 97%. Simulations performed using the Aramco 2.0 mechanism.

An ignition delay time correlation was created to match the syngas oxidation experiments (9). The correlation was created based on the experiments at two different pressure ranges. The correlation shows a negative dependence with pressure. This correlation also has the least predictive ability compared with an R^2 value of 0.786. The correlation for syngas ignition delay times is compared to the experimental data below in Figure 20.

$$\tau = 1.60 \cdot 10^{-1} \cdot e^{\frac{18800}{RT}} \cdot P^{-0.19} \tag{9}$$

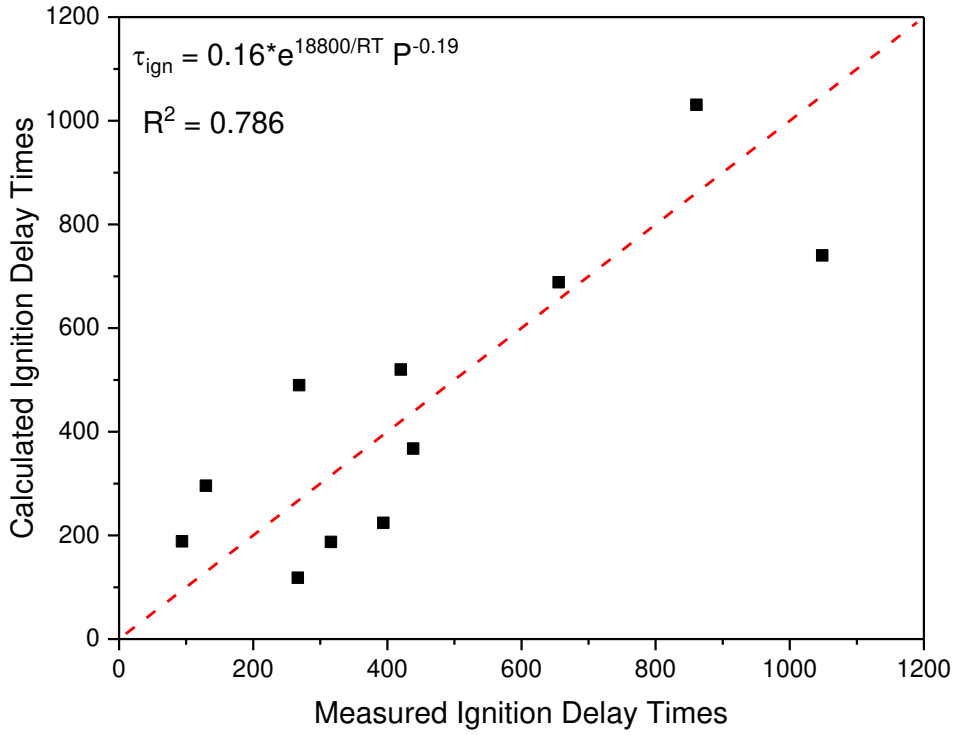

Figure 20: Ignition delay time correlation for syngas oxidation.

5.3 Ignition delay times in ethylene

Experiments were performed in a mixture of 1% C_2H_4, 3% O_2 in an Argon bath. Temperatures for these experiments ranged between ranged from 1192 to 1538 K for the low-pressure experiments. For the elevated pressures, the temperature ranged from 1179 to 1389 K. Table 8 shows the experimental results from the ethylene experiments.

Table 8: Experimental results from ethylene oxidation. X_{C2H4} = 0.01, X_{O2} = 0.03, X_{Ar} = 0.96.

Temperature [K]	Pressure [atm]	Ignition Delay Time [μs]
1538	1.46	90
1445	1.53	134.5
1389	1.60	199
1385	1.60	194
1336	1.67	287
1277	1.71	412.5
1236	1.76	652.5
1192	1.79	1030
1389	8.48	44.5
1303	8.99	136
1256	9.54	302
1179	9.75	995

Figure 21 shows that the CO time-histories are well represented during ethylene oxidation for pressures between 1 and 10 atm. The time-scales for CO oxidation are accurate and the concentrations after are shown to be well-predicted after ignition.

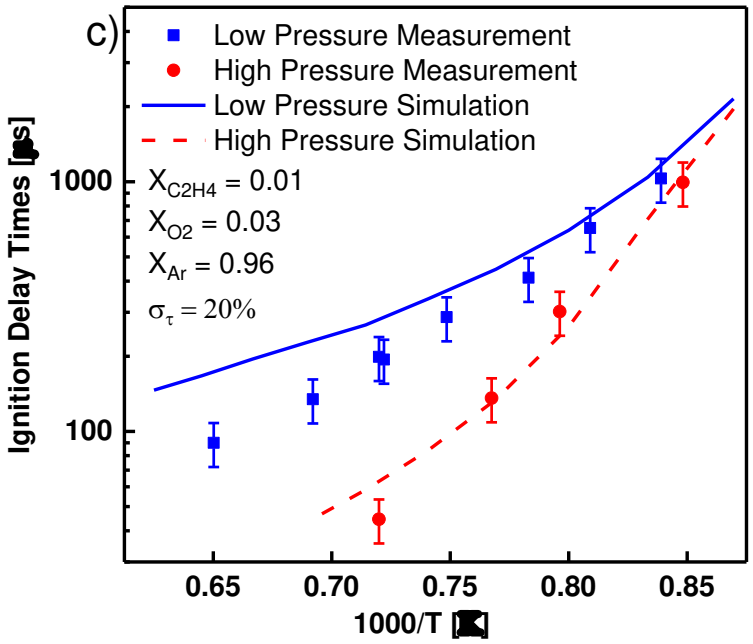

Figure 21: Ignition delay time measurements for ethylene oxidation. Mixture was X_{C2H4} = 1.0%, X_{O2} = 3.0% and X_{Ar} = 96.0%.

A correlation was created for the ethylene oxidation to calculate the ignition delay times and to determine the effect of pressure on the ignition delay times. A correlation for ethylene ignition delay times is shown below (10). The correlation is compared to the experimental data in Figure 22 below.

$$\tau = 6.16 \cdot 10^{-4} \cdot e^{\frac{34300}{RT}} \cdot P^{-0.18} \tag{10}$$

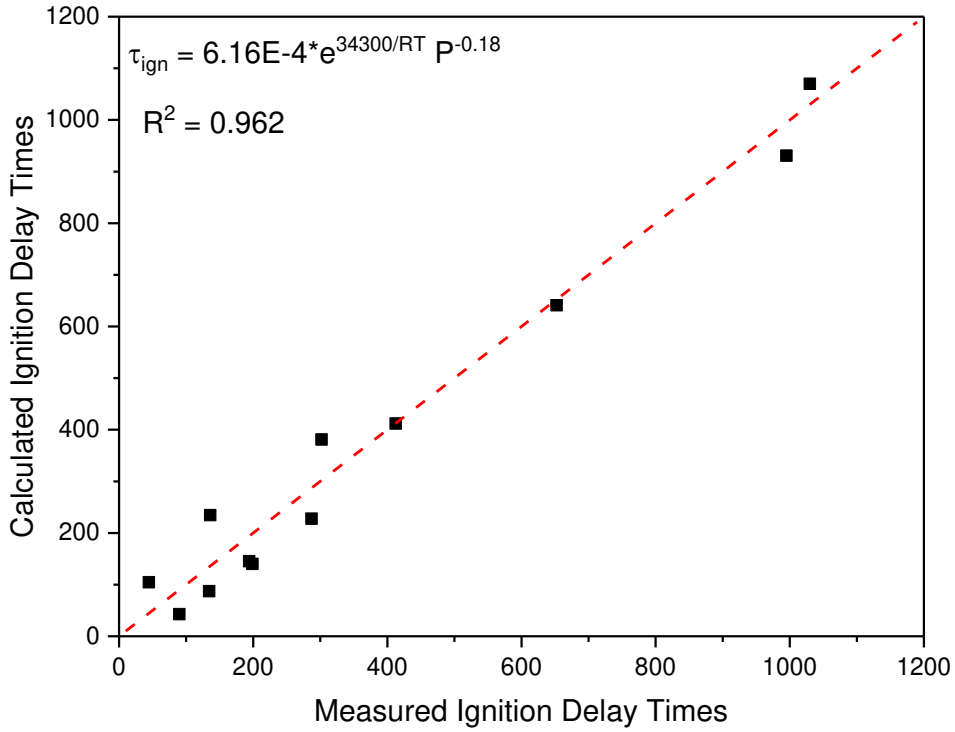

Figure 22: Ignition delay time correlation for ethylene oxidation.

5.4 Ignition delay times in REFGas, a natural gas surrogate

Natural gas is a combination of multiple gases that alter the ignition delay times compared to pure methane. REFGas is a surrogate mixture created by the Deutsches Zentrum für Luft- und Raumfahrt (DLR) to better simulate the conditions that are present during natural gas combustion in a gas turbine. The ignition delay times for REFGas oxidation are presented below in Figure 23.

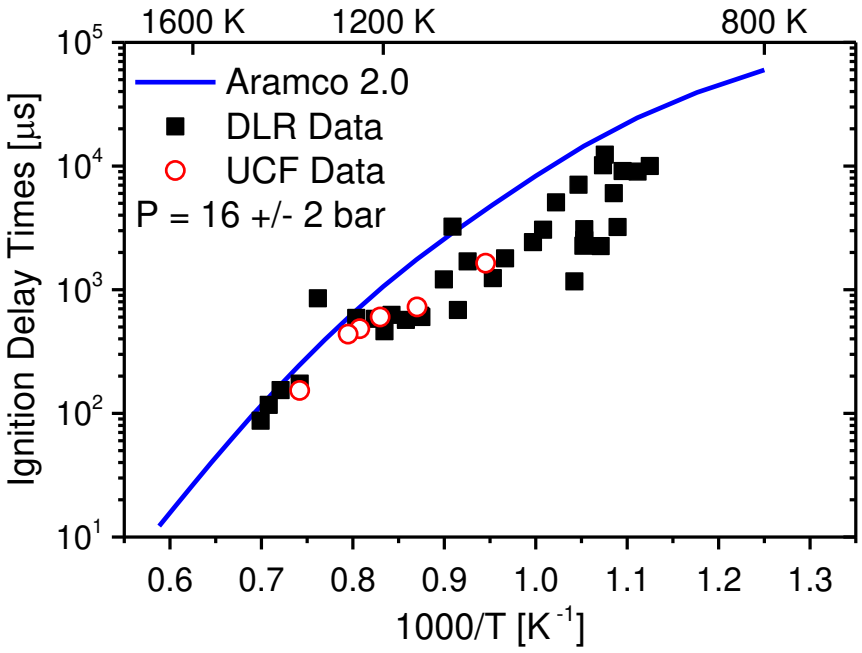

Figure 23: Ignition delay time measurements of REFGas combustion under a high fuel loading condition. Mixture: X_{CH4} = 14.51%, X_{C2H6} = 1.26%, X_{O2} = 32.89% and X_{CO2} = 51.34%.

CHAPTER 6: SPECIES TIME-HISTORIES IN NATURAL GAS SURROGATES

Carbon monoxide is one of the most important species during the combustion of natural gas. Carbon monoxide is a heavily regulated, toxic compound. Higher levels of carbon monoxide also signify incomplete and inefficient combustion as it shows that there is not enough oxygen in the system to oxidize the carbon monoxide into carbon dioxide. It has also been shown that replacing the diluent with carbon dioxide, higher levels of CO is formed but there has been relatively little work done in understanding the carbon monoxide time-histories in methane, ethylene or syngas.

Carbon monoxide time-histories are presented for in methane, syngas and ethylene oxidation for temperatures between 1100 K and 2100 K over a pressure range between 1-10 atm. The carbon monoxide time-histories.

6.1 Characterization of species' absorption cross-sections

The absorption cross-section is the measure of a given molecules absorptivity at a given wavelength of light. The cross-section is a function of the temperature and pressure of the mixture and can be combined with the Beer-Lambert Law (7) to calculate the mole-fraction of a target species from the absorbance given the temperature and pressure of the given system. The characterization of the methane cross-section was performed by Koroglu et al [33].

The absorption cross-section was measured for both carbon monoxide and carbon dioxide to isolate the absorption of CO during the experiment. The cross-section was measured using the

same experimental set-up as the oxidation study. The characterization was performed over a range of temperatures between 900 K and 2500 K to accurately cover the full range of the experiments and ensure that the edges of the characterization were accurate. The experiments were performed for a pressure range between 1 and 12 atm. The experimental results were compared to the HITEMP database for further comparison and an equation based on the HITEMP database and validated with the experimental results was created [63]. The equation below (11) shows the absorption cross-section equation that was used for all the following analysis.

$$\sigma_{CO} = P^{-0.95}(219.8 - 0.058T) \tag{11}$$

The equation can accurately predict the measured cross-sections across most of the conditions. The experimental results with the highest measured cross-sections (lowest pressures) perform the worst compared to the calculated results with a large spread compared to experimental results at 2 and 10 atm. Figure 24 shows the comparison between the calculated and measured results.

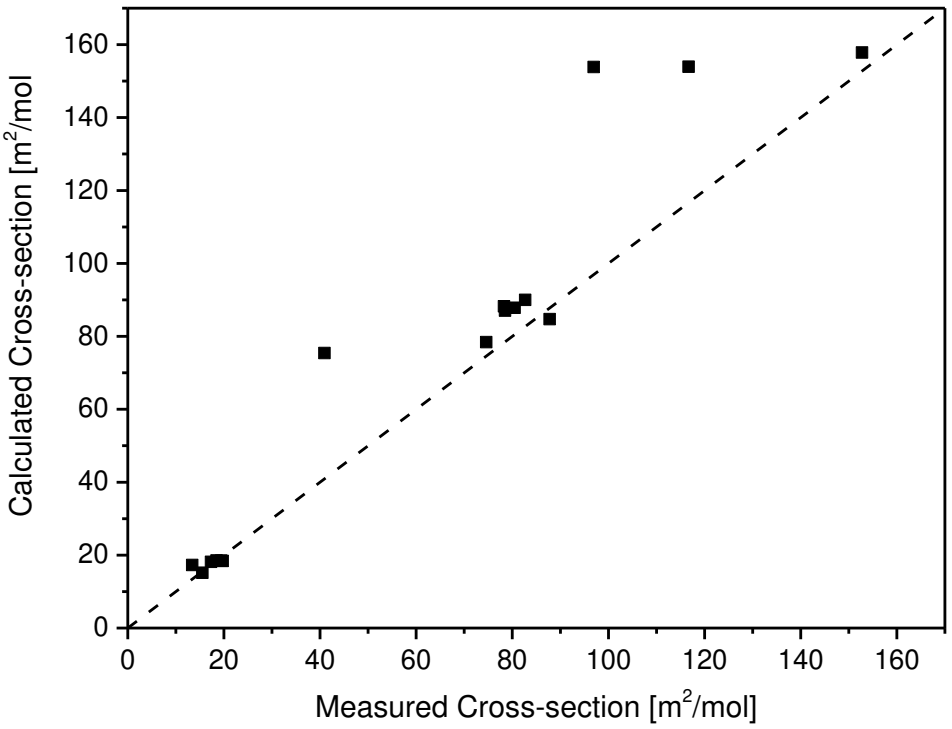

Figure 24: Characterization of the carbon monoxide absorption cross-section compared to the HITEMP database [63]. Values calculated from Equation (11) are based on the values from HITEMP.

The interference from carbon dioxide was determined to be larger than originally expected from the HITRAN database [64]. Experiments were performed to characterize the carbon dioxide cross-section at the same pressure and temperature conditions as the other experiments. The experiments were compared to simulations from the HITEMP database and an equation was created to calculate the absorption cross-section over a temperature range of 900-2500 K and up to 12 atm (12) [63].

$$\sigma_{CO2} = P^{0.046}(14.67 - 0.03T + 2.78 \cdot 10^{-5}T^2 - 5.29 \cdot 10^{-9}T^3) \quad (12)$$

The equation can accurately predict the cross-section measurements for the entire range of interest. The equation slightly underpredicts the cross-section at temperatures above 2000 K across the entire pressure range that was measured. Figure 25 compares the experimental data to the calculated carbon dioxide cross-sections.

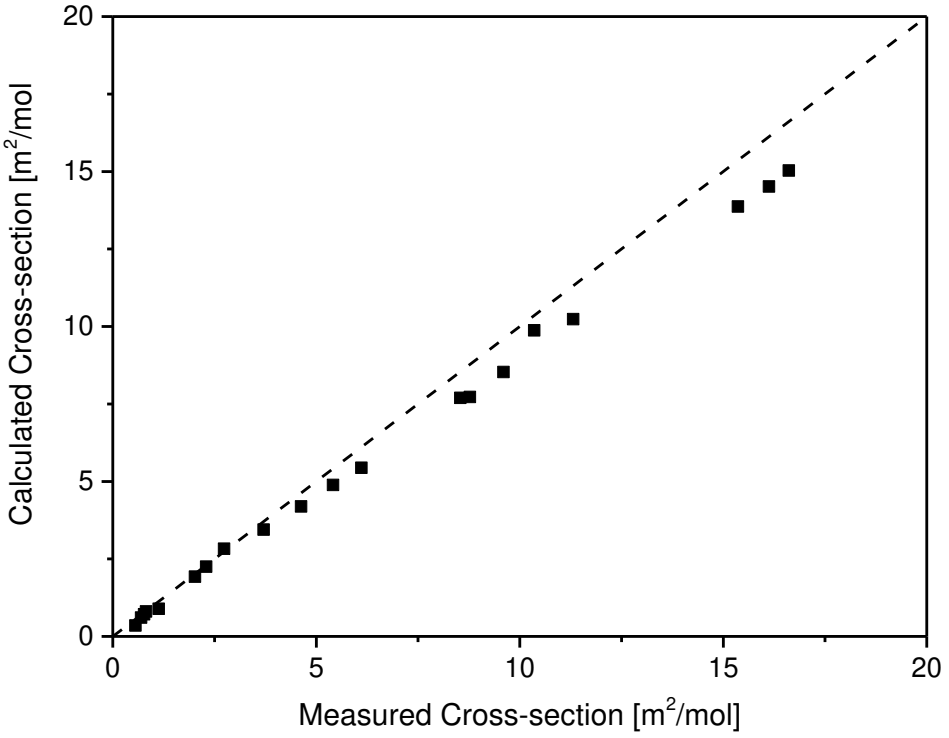

Figure 25: Characterization of the carbon dioxide absorption cross-section compared to the HITEMP database [63]. Values calculated from Equation (12) are based on the values from HITEMP.

6.2 Characterization of absorbance

During each experiment, the total absorbance time-history was calculated using the ratio of the light passing through the experiment. Several manipulations were performed on the raw absorbance traces to determine the carbon monoxide time-histories of the given experiment.

The intensity from the laser was filtered using a Savitzky-Golay filter with an order of one on the measured absorbance. This filter was used to remove noise from the laser and provide accurate comparisons to the simulated experiment. The filter was applied to both the transmitted intensity and the reference intensity. The filter window was taken to be 50 points before and after each data point.

The ignition delay time results show that the time-scales that the combustion process performed at are not precisely predicted by the Aramco 2.0 mechanism. As a result, two different points were used to scale the simulated results to the experimental results. For experiments with stoichiometric methane and ethylene experiments, the peak CO absorbance was used to scale the simulated results. As syngas and rich methane do not have a distinctive peak that can be matched, the CO inflection point was used to scale the results. The CO inflection point was defined as the intersection between the plateau level of CO and the tangent line of the CO as it approaches the plateau level. The results show that the absorbance traces can be accurately compared between experiment and simulations once the times have been scaled together.

The absorbance from carbon dioxide interference was then estimated using the simulation results from Chemkin. By calculating the expected absorbance from the simulation result, the contribution to the total of carbon monoxide could be calculated by removing the interference from carbon dioxide from the experimental trace [65].

The filtered signal was then compared to the original signal to determine the uncertainty in the measured absorbance trace. Since the absorbance is a ratio of two measured values, the uncertainty

in each trace was estimated by comparing the difference in the raw signal and the filtered signal. The uncertainty was taken to be two standard deviations in the window of the filtered signal.

The results for the measured CO absorbance and the processed data is shown in Figure 26.

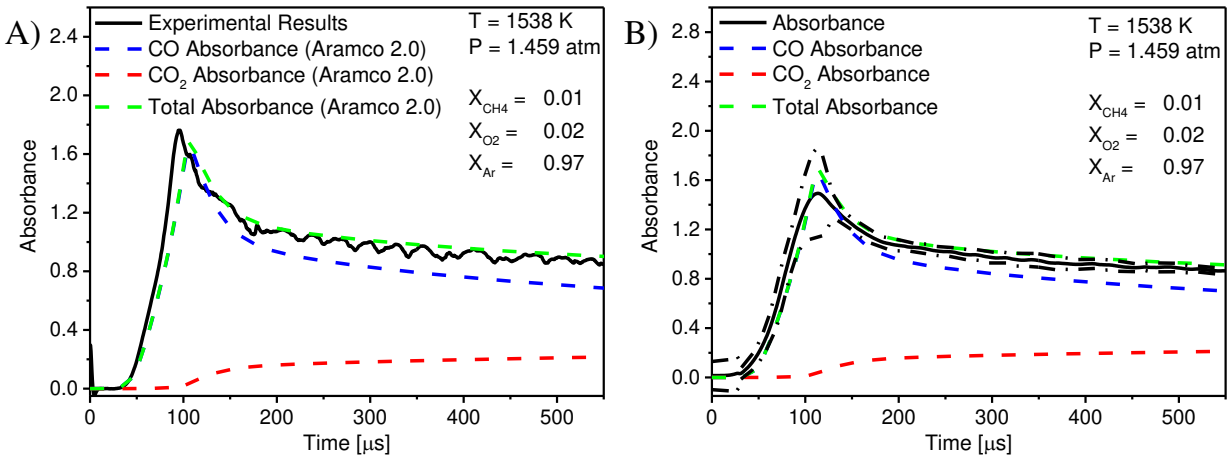

Figure 26: Example of data processing for the calculating the carbon monoxide time-histories. A) Unprocessed absorbance signal compared to the Aramco 2.0 mechanism. B) Final absorbance signal after data processing. Uncertainty bounds shown with black dashed line. Mixture: X_{C2H4} = 1.0%, X_{O2} = 3.0%, X_{Ar} = 96.0%.

6.3 Methane time-histories in methane oxidation

The time-histories of methane were recorded in experiments with and without carbon dioxide dilution for all the methane experiments. The experimental conditions for the experiments can be seen in Table 3-6. The methane time-histories provide further validation of the experimental time-scales for ignition and verify the fuel profile shape from the Aramco 2.0 simulation. The experimental results show that the Aramco 2.0 mechanism can accurately predict the methane time-histories with and without carbon dioxide as the primary diluent (Figure 27). The main

difference between the experimental traces is that the noise greatly increases when carbon dioxide is used as the primary diluent for both the pressure and laser trace. The experimental results show that the altered methane profile at the highest levels of carbon dioxide dilution are still well matched by both mechanisms.

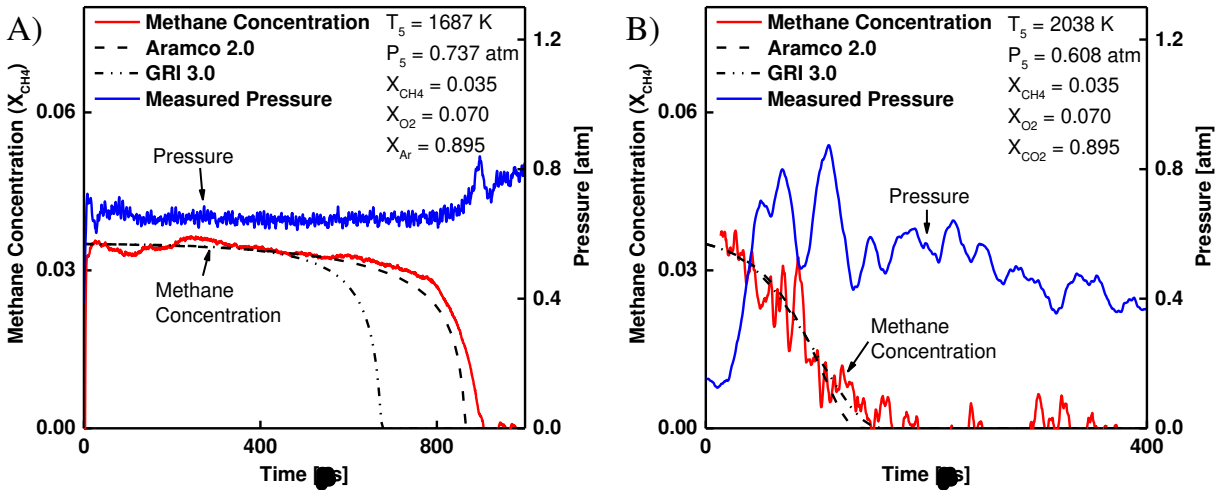

Figure 27: Time-resolved methane concentrations for mixtures with and without carbon dioxide dilution around 1 atm. A) Mixture: X_{CH4} = 3.5%, X_{O2} = 7.0%, X_{Ar} = 89.5%. B) Mixture: X_{CH4} = 3.5%, X_{O2} = 7.0%, X_{CO2} = 89.5%.

6.4 Carbon monoxide time-histories in methane oxidation

Carbon monoxide time-histories were measured for the experiments without carbon dioxide dilution. The carbon monoxide time-histories were compared to the Aramco 2.0 mechanism until shortly after the ignition delay time. This comparison stops after ignition due to issues with the temperature and pressure after combustion because the shock tube can no longer be considered a constant volume chamber and the increasing interference with carbon dioxide that occurs as a

result. Experiments cover a range of temperatures between 1600 and 2100 K and pressures between 1 and 10 atm.

Several comparisons were made between the experimental traces and the simulated results. The first comparison is the time it takes for the carbon monoxide to reach the peak carbon monoxide concentration during the experiment. The peak value of carbon monoxide was also calculated and compared for each experiment and finally, the steady-state level of carbon monoxide. For rich methane oxidation, the peak time was replaced with the inflection time. The inflection time was defined as the time when the carbon monoxide concentration starts to plateau at the steady-state value. The time was calculated by determining the intersection of the tangent line at the maximum slope with the plateau level of carbon monoxide.

6.4.1 Carbon monoxide time-histories at stoichiometric conditions

Experimental traces of carbon monoxide were compared to simulations from the Aramco 2.0 mechanism for methane oxidation under stoichiometric conditions (Figure 28). The results show that the carbon monoxide is overpredicted at low pressures compared to the experimental result but that the overall trend is predicted well. The results show a rapid rise at the time of ignition before reaching a peak level and then reaching a slow steady rate of depletion post combustion. At the elevated pressures near 10 atm, the interference from carbon dioxide was much greater than experienced at low pressures. Post combustion the absorbance measured by carbon dioxide is greater than the total absorbance measured during the experiments despite the carbon dioxide cross-section being well validated in this region.

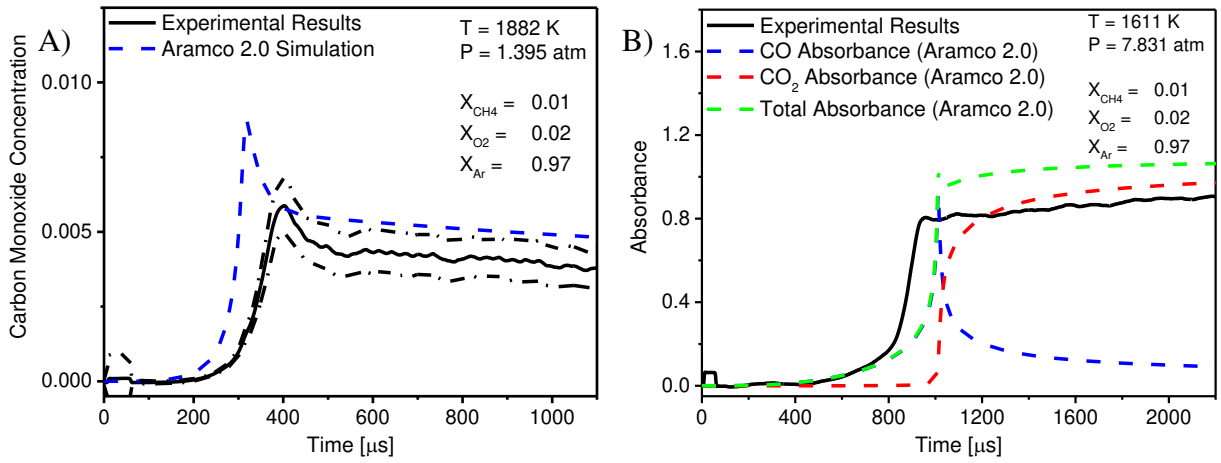

Figure 28: Time-resolved carbon monoxide concentration measurements in stoichiometric methane oxidation at different pressures. A) Experiments performed at atmospheric conditions. Uncertainty bounds shown with black dashed line. B) Experiments performed at elevated pressures. Mixture was X_{CH4} = 1.0%, X_{O2} = 2.0%, X_{Ar} = 97.0%.

All the experiments were compared to understand how temperature affects the carbon monoxide concentrations. The time of the peak CO concentration was measured and compared to the simulations performed by the Aramco 2.0 simulation. The results, shown in Figure 29, are displayed below. The results show that the Aramco 2.0 mechanism can accurately predict the time-scales of carbon monoxide well with the time that the peak level being measured at closely matching the results for the ignition delay times. At elevated pressures, the time-scale performs better than the ignition delay times at the lowest temperatures.

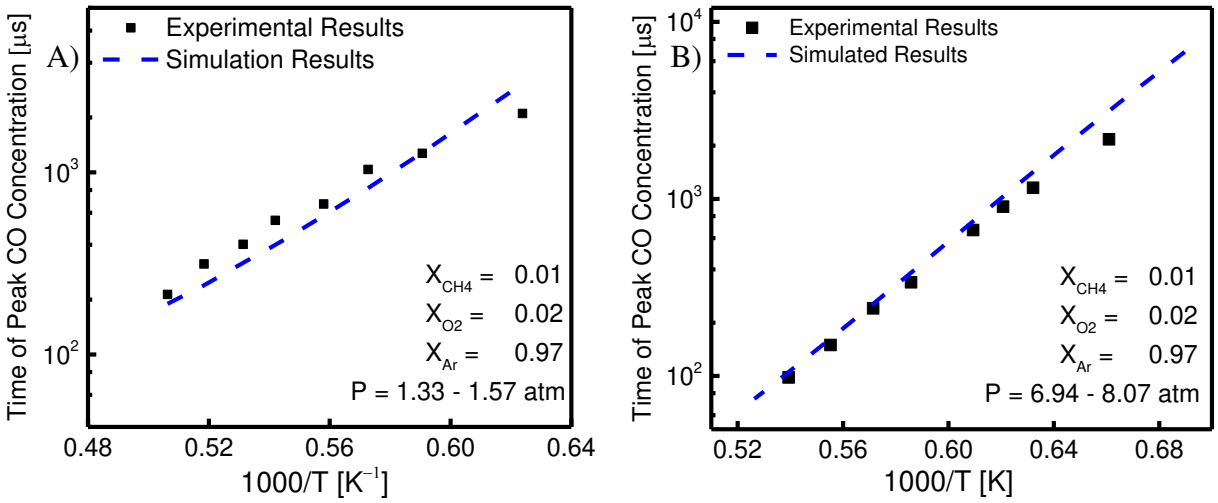

Figure 29: Experimental and modeling results for the time that the peak level of carbon monoxide occurs at. A) Experiments performed at atmospheric conditions. B) Experiments performed at elevated pressures. The experimental results are compared to the Aramco 2.0 mechanism. All experiments were performed for a mixture of X_{CH4} = 1.0%, X_{O2} = 2.0%, X_{Ar} = 97.0%.

The carbon monoxide concentration was also compared at two times to the simulated values. These peak values were the peak CO concentration which occurred around the time of ignition and the concentration of carbon monoxide after 25% more time passed after ignition. This intermediate location was chosen to understand how fast the carbon monoxide depleted after combustion but was short enough to eliminate the issues with the fluid dynamics of the shock tube. Figure 30 displays the results compared to the experiments and show that the carbon monoxide concentration is overpredicted at both times during the experiment. At the peak concentration, the carbon monoxide concentration was predicted to be twice as much as measured. The peak concentration remains relatively constant across all temperatures measured with some scatter in the experimental data. The intermediate concentration shows that the carbon monoxide also experiences a smaller amount of oxidation to carbon dioxide than compared to be the simulations and the decreasing level with decreasing temperature is also predicted by the experiments.

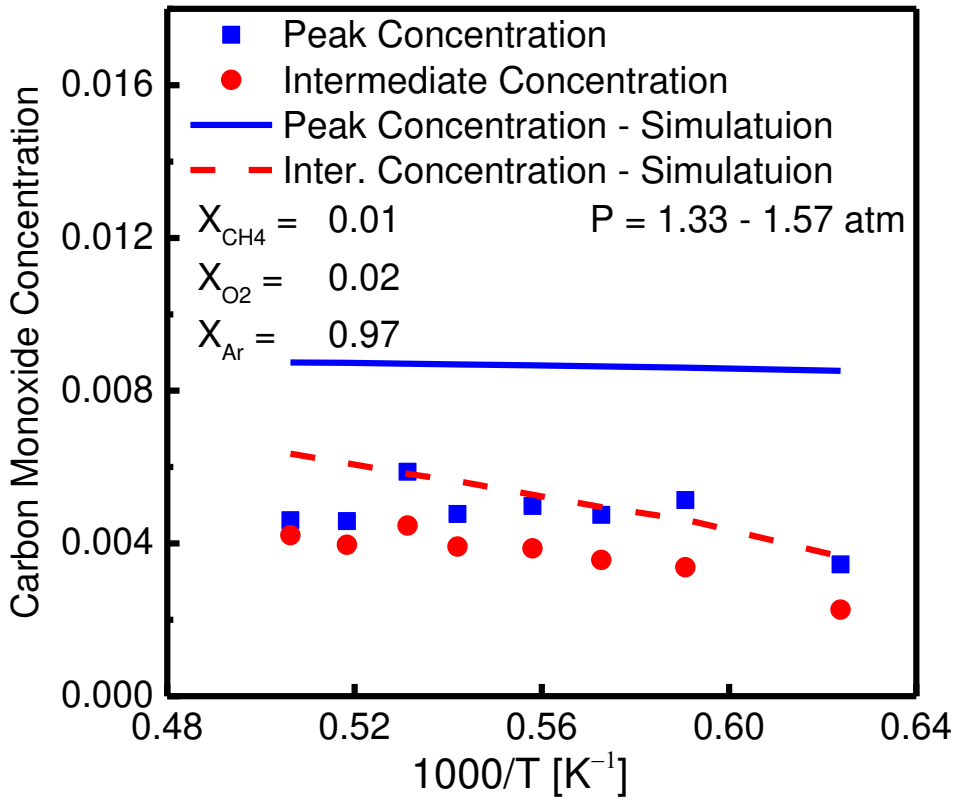

Figure 30: Carbon monoxide concentrations at two times during the experiment. The concentration of the peak carbon monoxide concentration and at a time 25% longer were compared to the Aramco 2.0 mechanism. All experiments were performed for a mixture of X_{CH4} = 1.0%, X_{O2} = 2.0%, X_{Ar} = 97.0%.

6.4.2 Carbon monoxide time-histories at fuel-rich conditions

The carbon monoxide time-histories were also compared to the results for fuel-rich conditions. Two carbon monoxide profiles are compared below in Figure 31. The Aramco 2.0 mechanism does an excellent job predicting the general trend at both atmospheric conditions and elevated pressures. The results show that the carbon monoxide concentration eventually reaches a plateau level as shown below. The experimental results show that at atmospheric conditions, the carbon

monoxide concentration is overpredicted by the Aramco 2.0 mechanism but is better predicted at the elevated pressures. The carbon monoxide time-histories were able to be extended longer for the fuel-rich conditions due to limited interference with carbon dioxide and minimal pressure rise after combustion.

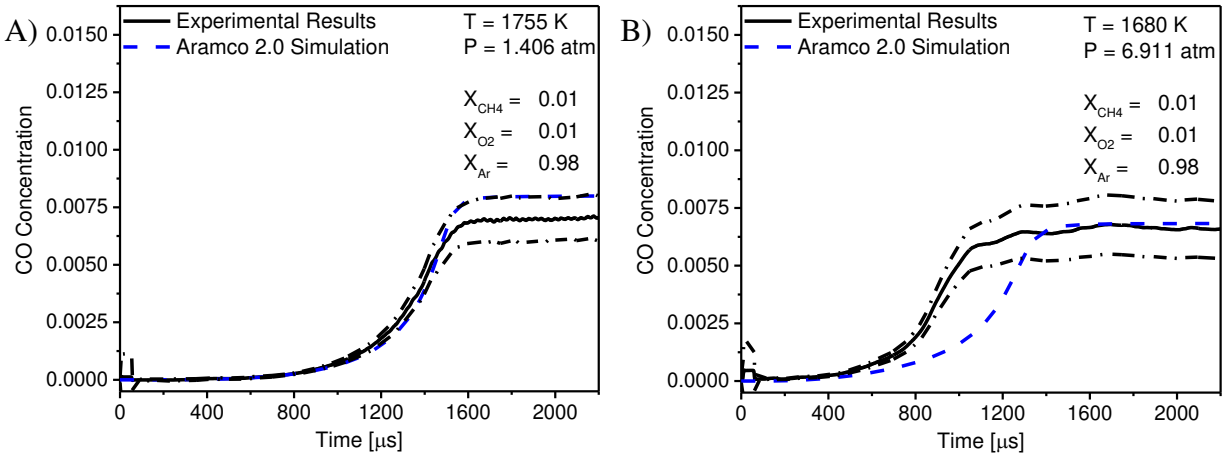

Figure 31: Carbon monoxide time-history measurements in fuel-rich methane combustion at different pressures. A) Experiments performed at atmospheric conditions. B) Experiments performed at elevated pressures. Uncertainty bounds shown with black dashed lines. All experiments were performed for a mixture of X_{CH4} = 1.0%, X_{O2} = 1.0%, X_{Ar} = 98.0%.

As there is no sharp peak as with stoichiometric conditions, a new time-scale was created to compare the experimental results with the simulations. This time-scale was defined as the intersection of the tangent line of maximum ascent of carbon monoxide with the plateau level of carbon monoxide measured, referred to as the inflection time. The experimental results match well with the simulations showing an increasing time-scale as the temperature drops similar to the trend displayed in the ignition delay times.

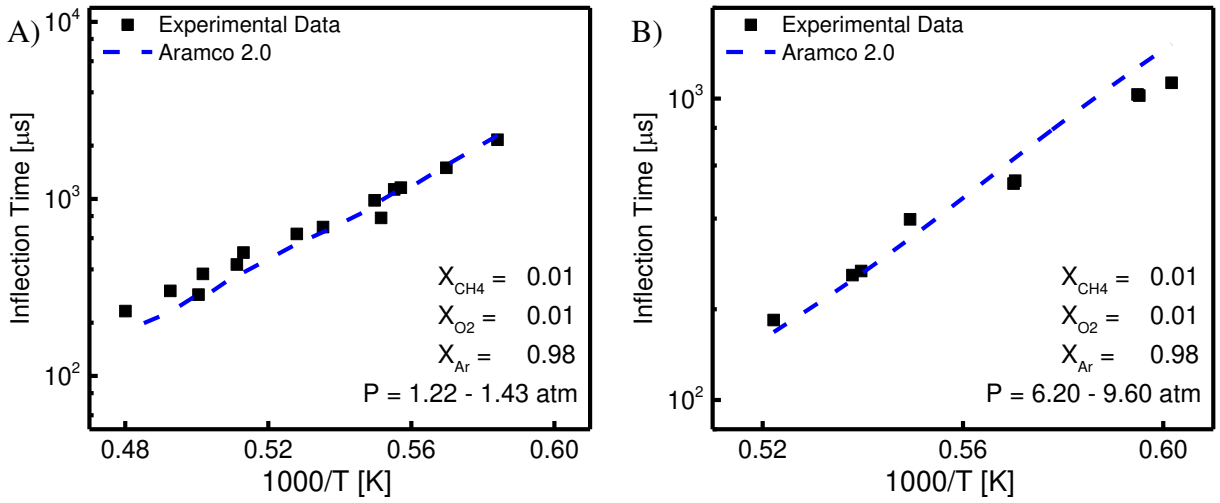

Figure 32: Inflection time of the carbon monoxide concentration during fuel-rich combustion of methane. A) Experiments performed at atmospheric conditions. B) Experiments performed at elevated pressures. Experimental results were compared to the Aramco 2.0 mechanism. All experiments were performed for a mixture of X_{CH4} = 1.0%, X_{O2} = 1.0%, X_{Ar} = 98.0%.

The plateau level for carbon monoxide was also examined for fuel-rich combustion. The maximum concentration for the fuel-rich conditions is overpredicted at the lowest pressures but matches well for the elevated pressures.

6.5 Carbon monoxide time-histories in syngas oxidation

Experimental traces of carbon monoxide were compared to simulations from the Aramco 2.0 mechanism for syngas oxidation for a mixture of X_{CO} = 1.0%, X_{H2} = 1.0%, X_{O2} = 1.0%, X_{Ar} = 97.0%. Two different carbon monoxide profiles are shown below in Figure 33. The experimental traces show that carbon monoxide concentrations are well predicted by the Aramco 2.0 mechanism at both atmospheric and elevated pressure.

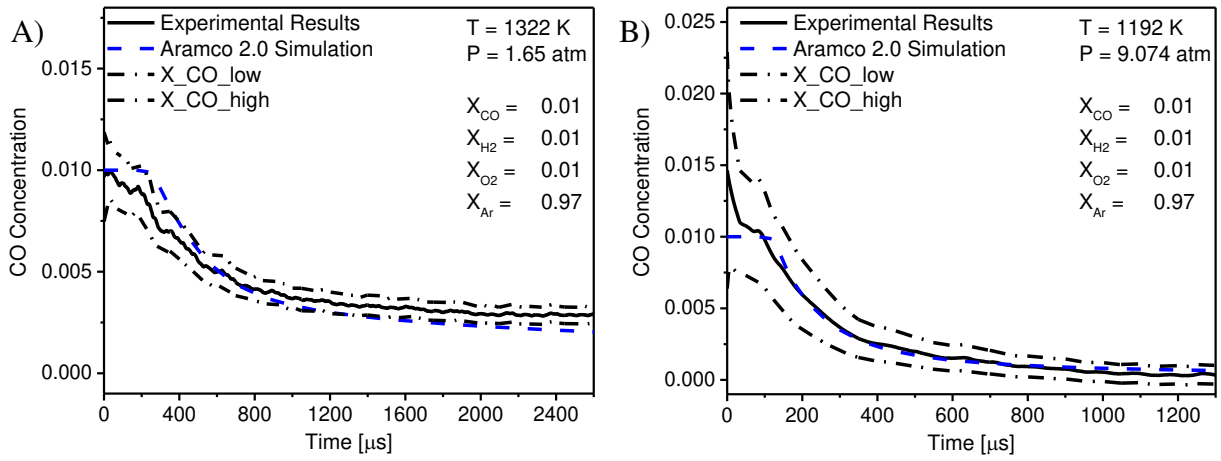

Figure 33: Carbon monoxide time-history measurements in syngas oxidation at different pressures. A) Experiment performed at atmospheric conditions. B) Experiment performed at elevated pressures. Uncertainty bounds shown with black dashed lines. Mixture was X_{CO} = 1.0%, X_{H2} = 1.0%, X_{O2} = 1.0%, X_{Ar} = 97.0%.

Two different time-scales were again used to understand how temperature affected the carbon monoxide time-histories. The first time-scale is the start of carbon monoxide depletion while the second is the time when the carbon monoxide concentration shifts rates of consumption. These time scales are calculated by comparing the maximum rate of carbon monoxide depletion to the initial concentration of carbon monoxide and the steady-rate after combustion. The two time-scales are displayed below in Figure 34 at both atmospheric and elevated pressures.

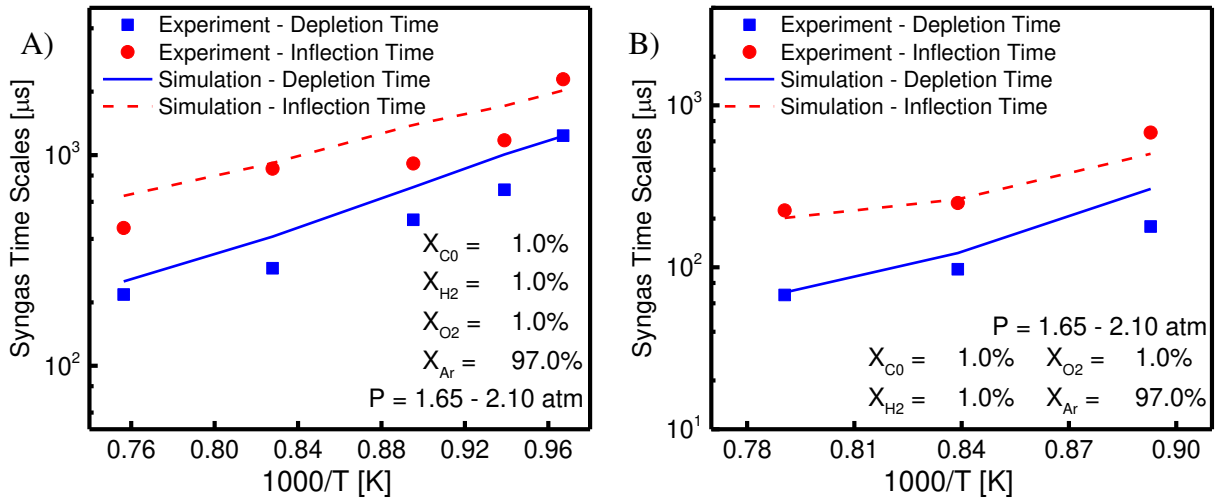

Figure 34: Time-scales for carbon monoxide concentrations during syngas combustion. A) Experiments performed at atmospheric conditions. B) Experiments performed at elevated pressures. Experimental results were compared to the Aramco 2.0 mechanism. All experiments were performed for a mixture of X_{CH4} = 1.0%, X_{O2} = 1.0%, X_{Ar} = 98.0%.

The carbon monoxide concentrations were also compared at these two time-scales. The carbon monoxide concentration had no general trend. Data was noisy. Relatively constant. Had a negative trend with decreasing temperature

6.6 Carbon monoxide time-histories in ethylene oxidation

The final fuel that was measured was ethylene. All experiments were performed in a mixture of X_{C2H4} = 1.0%, X_{O2} = 3.0% and X_{Ar} = 96.0%. The carbon monoxide time-histories were able to be predicted well for atmospheric conditions, but the carbon dioxide interference was extremely high at the elevated pressures; similar to the results for stoichiometric methane combustion. The main difference between ethylene and methane combustion is the early initial rise in the carbon monoxide concentration. Ethylene starts to decompose earlier than methane and therefore carbon monoxide can be seen being formed as early as 50 µs after the reflected shock wave. At

atmospheric conditions, the peak and the post-combustion level for carbon monoxide was well predicted based on the results in Figure 35.

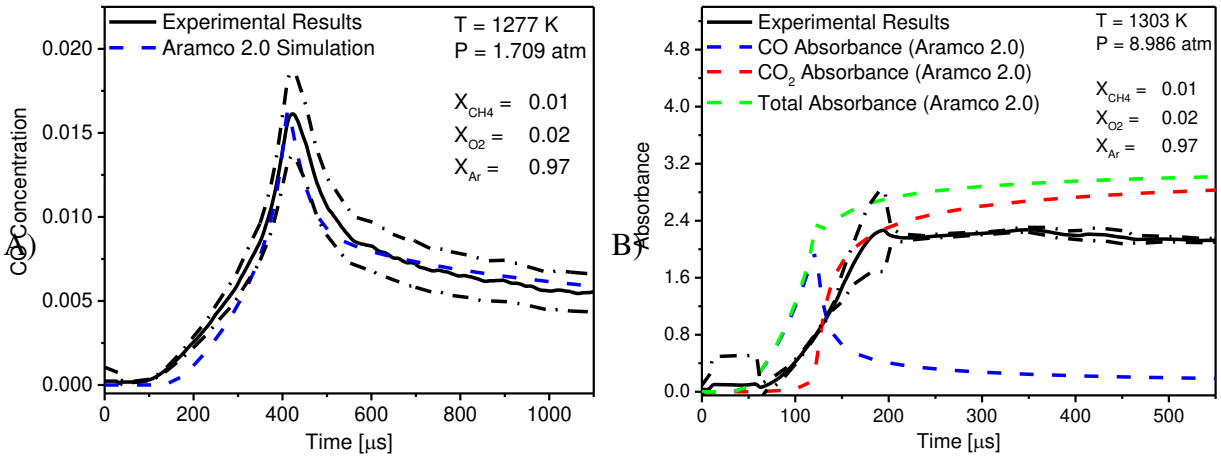

Figure 35: Carbon monoxide time-history measurements in ethylene oxidation at different pressures. A) Experiments performed at atmospheric conditions. B) Experiments performed at elevated pressures. Uncertainty bounds shown with black dashed line. Mixture was X_{CO} = 1.0%, X_{H2} = 1.0%, X_{O2} = 1.0%, X_{Ar} = 97.0%.

Two time-scales were again employed to understand the carbon monoxide time-histories across the measured temperature range. The first time-scale was time it took to reach the peak CO concentration during the experiment. The second time-scale was 25% after the peak CO concentration.

Figure 38 shows the first time-scale and the concentration of carbon monoxide at the two different time-scales. The time of the peak CO concentration is well predicted by the Aramco 2.0 mechanism as well as the concentration of carbon monoxide. The main discrepancy between the model and the experimental results is the peak CO concentration at the hottest temperatures which is slightly overpredicted compared to the measured values.

A) B)

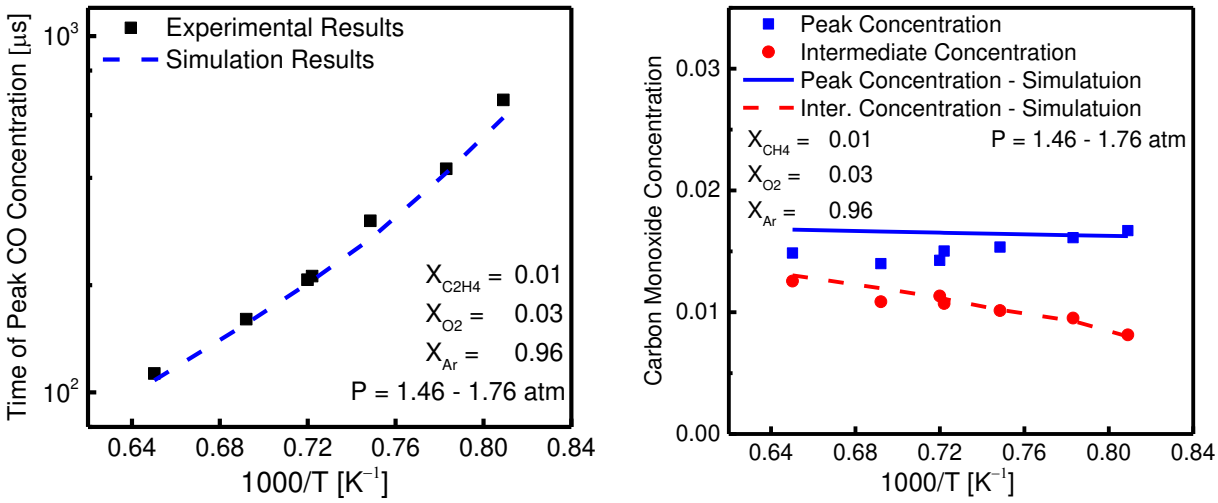

Figure 36: Comparison of carbon monoxide concentrations during ethylene combustion at atmospheric pressures. A) Time of Peak CO level. B) Peak CO concentration at two different time scales. All experiments were performed for a mixture of X_{C2H4} = 1.0%, X_{O2} = 3.0%, X_{Ar} = 96.0%.

6.7 Carbon monoxide sensitivity of the Aramco 2.0 mechanism

To understand the key differences between the Aramco 2.0 mechanism and the experimental results, a sensitivity analysis was performed on carbon monoxide and carbon dioxide for both methane and ethylene oxidation. The sensitivity analysis was performed using the built-in code in Chemkin Pro [66]. The sensitivity analysis was performed for both atmospheric and elevated pressures to isolate differences between based on the pressure of the system. A sensitivity analysis was not performed for syngas oxidation as was determined that syngas was well predicted by the mechanism.

6.7.1 Sensitivity analysis for stoichiometric methane combustion

A sensitivity analysis was performed on methane at both stoichiometric and fuel-rich conditions for atmospheric pressure. The simulation was performed for a temperature of 1800 K or around the median temperature of the experiments. The sensitivity analysis shows that most of the reactions have the opposite effect on the carbon monoxide concentrations between the two conditions Figure 37.

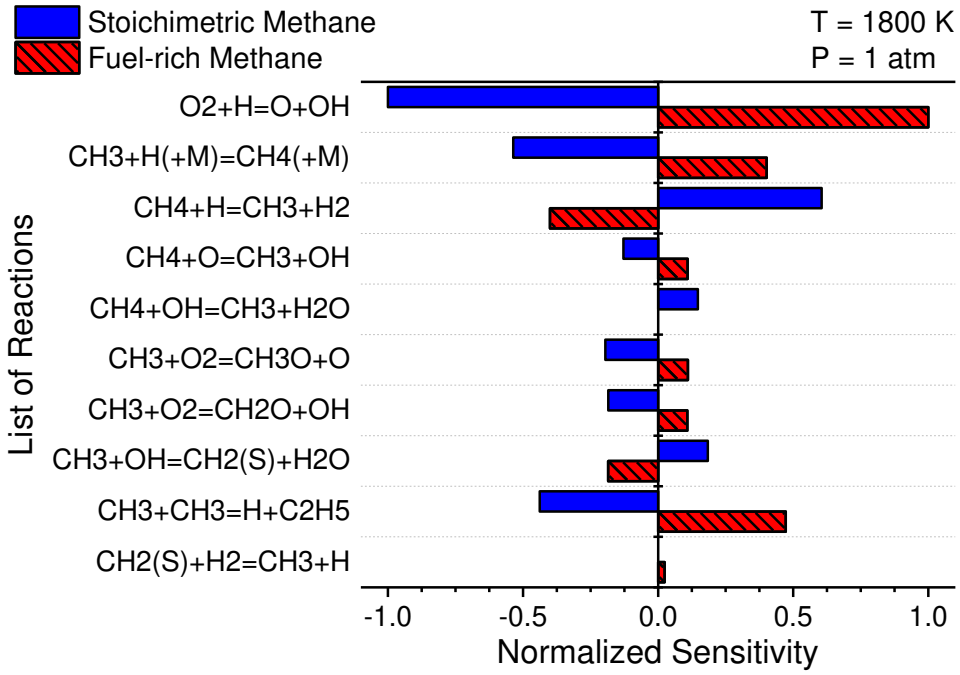

Figure 37: Sensitivity Analysis for carbon monoxide formation during atmospheric methane combustion. Sensitivity performed for the Aramco 2.0 mechanism at the time of ignition.

The most sensitive reaction is the chain branching reaction between converting oxygen in an oxygen atom and a hydroxyl radical. This is expected as it is the primary reaction for propagating the chemical kinetics. The other important reactions that were of more interest were the methyl

radical chemistry that was highlighted in the analysis. These reactions are important pathways that encourage the abstraction of H atoms from methane which leads to the formation of formyl radicals the main pathway to carbon monoxide formation (through CH_3O and CH_2O).

A sensitivity analysis was also performed at the same temperature but at 10 atm (Figure 38). This simulation shows that the propagation reaction becomes even more dominate at these elevated pressures. The elevated pressures also show higher sensitivity on the methane and methyl radical chemistry. The fuel rich chemistry revealed that the higher pressures were sensitive to methylene chemistry.

By looking at these different reactions, it is shown that more understanding needs to be performed at the different radicals and intermediate species that eventually lead to the formation of carbon monoxide through the formyl radical.

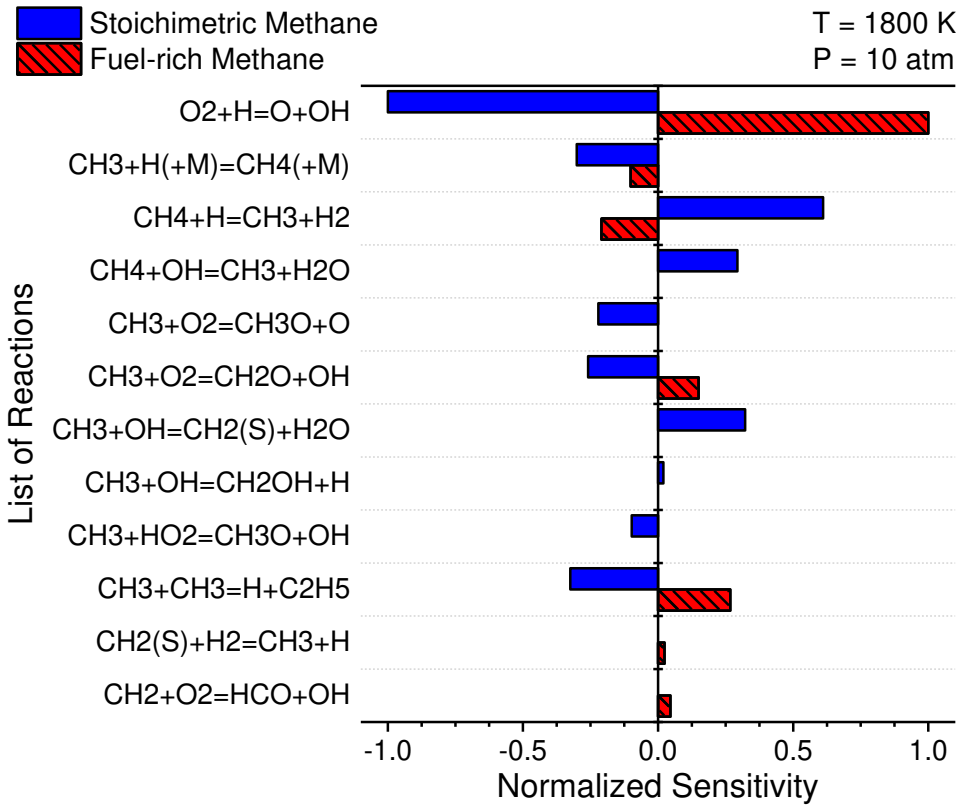

Figure 38: Sensitivity Analysis for carbon monoxide formation during elevated methane combustion. Sensitivity performed for the Aramco 2.0 mechanism at the time of ignition.

6.7.2 Sensitivity analysis for ethylene combustion

A sensitivity analysis was also performed on ethylene as the high-pressure experiments predicted much higher carbon dioxide absorbance than was possible during the experiments. Most of the reactions have near equal sensitivity between the pressures except for two main differences. The first difference is that the low pressures show some sensitivity to formyl radical chemistry. These pathways are the dominate reactions for the formation of carbon monoxide. The next difference is the breakdown of ethylene, particularly when colliding with hydroperoxyl radicals (HO_2).

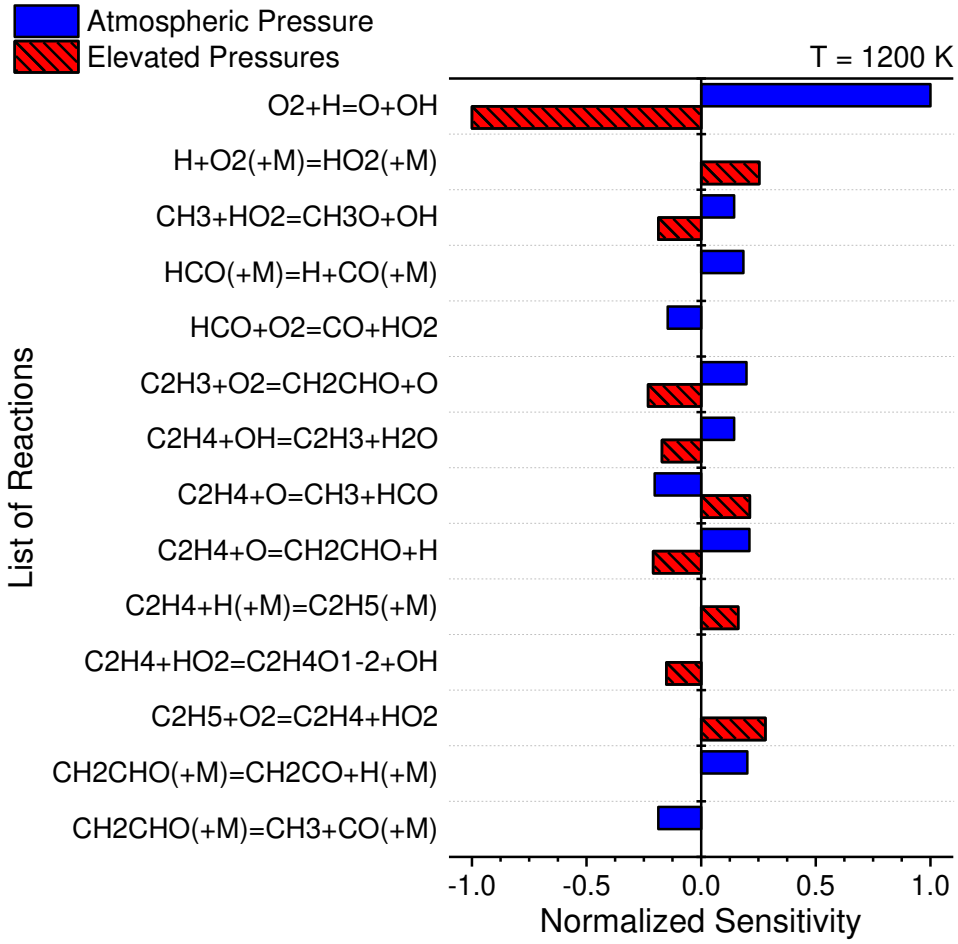

Figure 39: Sensitivity Analysis for carbon monoxide formation during ethylene combustion. Sensitivity performed for the Aramco 2.0 mechanism at the time of ignition.

CHAPTER 7: EFFECT OF WATER ADDITION

The nature of these novel mixtures is that they entire system is designed to be closed-loop. As a result, there is concern about the build-up of carbon monoxide and water in the system. In this section, experimental results on the effect of water ignition on the ignition of natural gas is discussed. Water was added to a mixture of methane and ethane up to 50% of the overall mixture of the system. The experiments were conducted at DLR and UCF.

7.1 Effect of water addition on the ignition delay times

Experiments were performed for several mixtures (Table 9) to look at the combination of water and CO_2 on the effect of ignition delay times of REFGAS. Mixture 1 contained a total level of 5% water and the ignition delay times show (Figure 40) that the predictions by the Aramco 2.0 is very good. This result is similar to previous experimental results from UCF which have shown that ignition delay times of highly diluted CO_2 methane mixtures are well modeled by detailed mechanisms found in the literature [67].

Table 9: Summary of mixtures with water dilution

	X_{CH4}	X_{C2H6}	X_{O2}	X_{CO2}	X_{H2O}	Facility
1	0.1451	0.0126	0.3289	0.5134	0.0000	UCF / DLR
2	0.0767	0.0067	0.1667	0.7000	0.0500	UCF
3	0.0759	0.0075	0.1669	0.6498	0.1000	UCF
4	0.0758	0.0081	0.168	0.5983	0.1498	UCF
5	0.0726	0.0063	0.1645	0.2567	0.5000	DLR

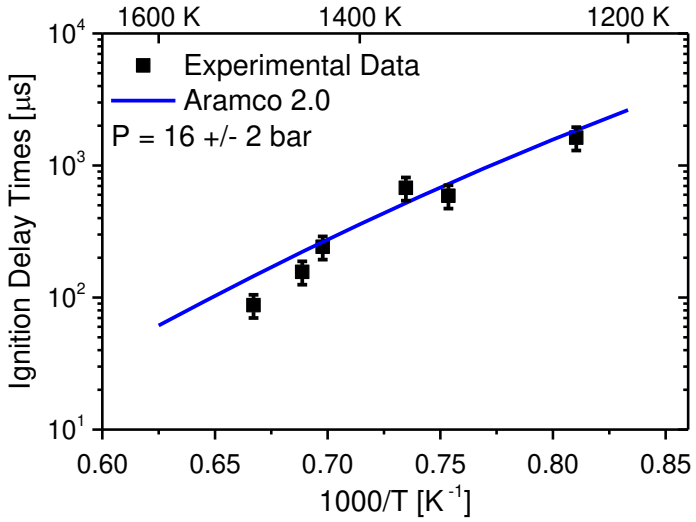

Figure 40: Ignition delay times for baseline mixture (Mixture 2). (X_{CH4} = 0.0767, X_{C2H6} = 0.0067, X_{O2} = 0.1667, X_{CO2} = 0.7000, X_{H2O} = 0.0500). Simulations were performed with the Aramco 2.0 mechanism.

The third and fourth mixtures increased the level of water to 10 and 15%, respectively. One common solution to reduce the emissions of natural gas combustion is to recirculate the exhaust gas of the system. These two mixtures show how ignition delay times respond to increasing water fractions. Results in Figure 41 show that the predictions of the ignition delay times are still matched

well with the experimental results up to 15% water dilution with a fuel and oxidizer loading of 25%.

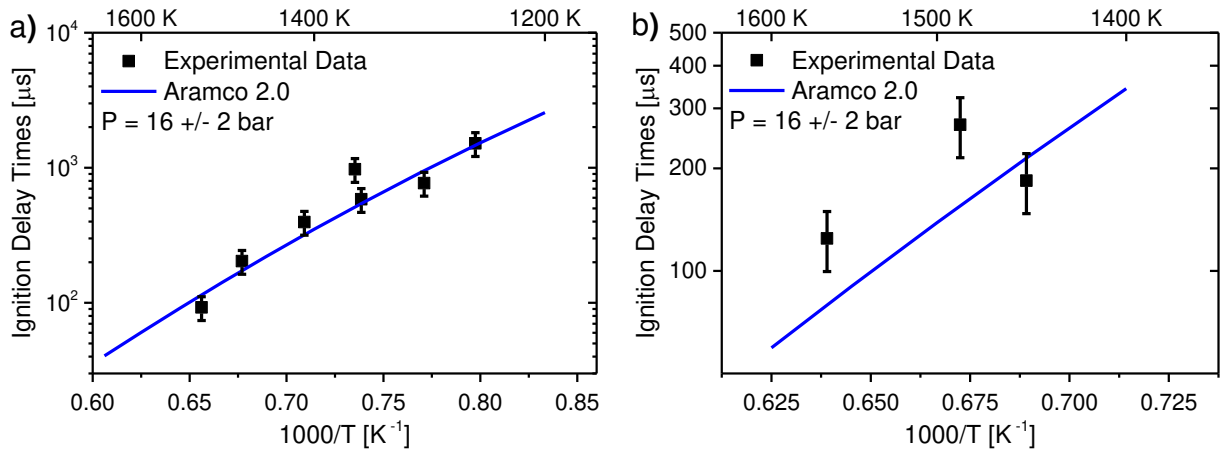

Figure 41: a) Ignition delay times for Mixture 3 (X_{CH4} = 0.0759, X_{C2H6} = 0.0075, X_{O2} = 0.1669, X_{CO2} = 0.6498, X_{H2O} = 0.1000). b) Ignition delay times for Mixture 4 (X_{CH4} = 0.0758, X_{C2H6} = 0.0081, X_{O2} = 0.1680, X_{CO2} = 0.5983, X_{H2O} = 0.1498). Simulations were performed using the Aramco 2.0 mechanism.

To understand the effect that water would have on REFGAS ignition and to stress the chemical kinetics, experiments were performed with 50% H_2O and only 25% CO_2. The results from Mixture 5 (Figure 42) display that with the addition of significant water, the ignition delay times are longer than those predicted by the Aramco 2.0 mechanism for the entire range of temperatures between 1100 and 1500 K. Again, an average pressure rise of 2% per ms was factored into the simulations. The results indicate similar scatter as the first mixture although the model clearly shows an underprediction in the experimental results.

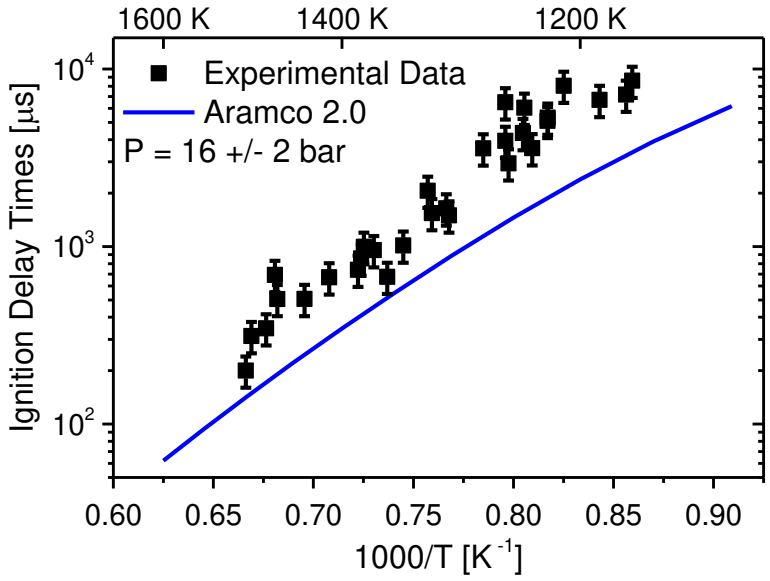

Figure 42: Ignition delay times for Mixture 4 (X_{CH4} = 0.0726, X_{C2H6} = 0.0063, X_{O2} = 0.1645, X_{CO2} = 0.2567, X_{H2O} = 0.5000). Simulations were performed with the Aramco 2.0 mechanism with a 2% per ms pressure rise.

7.2 Sensitivity Analysis on the Effect of Water Addition

A sensitivity analysis was performed on the hydroxyl (OH) and carbyne (CH) time-histories to understand the dependence of ignition delay times on different reactions in the mechanism. Based on the sensitivity analysis, the main reactions that affect the ignition delay times are similar to those for Mixture 2 (shown in Figure 43 for OH). The difference between various reactions shown in Figure 43 are changes in the C_2 chemistry with H_2O playing some role. It has also been observed that the third-body collisions become extremely important for CH sensitivity (not shown here). This suggests that the difference in the predictions and data (as seen in Figure 42) may be a result of lack of understanding of H_2O and CO_2 as third body partners. Therefore, future investigations

should focus on accurately determining the collision efficiencies (either through experiments or theoretical calculations).

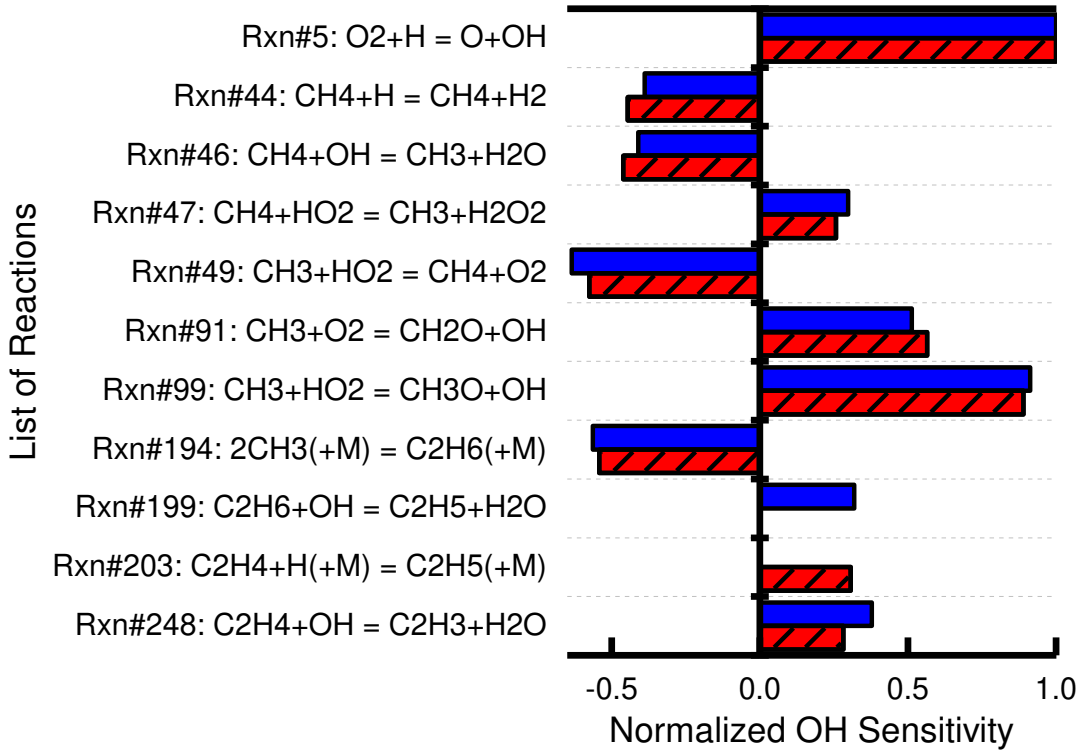

Figure 43: Normalized Sensitivity for hydroxyl radicals for Mixtures 2 (blue) and 5 (red -dashed) performed using the Aramco 2.0 mechanism.

It was also seen in the experiments that at elevated temperatures, the emissions exhibited a large initial rise at the arrival of the reflected shock wave as shown in Figure 44. The emission profile was seen at several different wavelengths in the visible light spectrum but not at 310 nm (for measuring OH* for ignition determination). Several theories were established to determine the cause of this initial rise. Two types of water were tested, deionized water and high purity water, to determine if any types of impurities were being excited by the hot gases. It was determined that the type of water had a minute effect on the ignition delay time with both types of water exhibiting

the same effect at the high temperatures. The second theory for the initial rise was that the hot gases were exciting the water with the second temperature jump from the reflected shock wave. Experiments were performed with 50% H_2O in air and was determined that the hot gases did not emit at the same conditions as Mixture 5. The final theory was that the CO_2* was being formed resulting in a small amount of emissions immediately after the arrival of the reflected shock wave. This phenomenon is only present with the addition of the fuel and oxidizer and was not present without the water. This shows that the reactions leading to involving CO_2* are becoming more relevant at these elevated temperatures and are playing a larger role in the combustion process diagnostics than was previously understood.

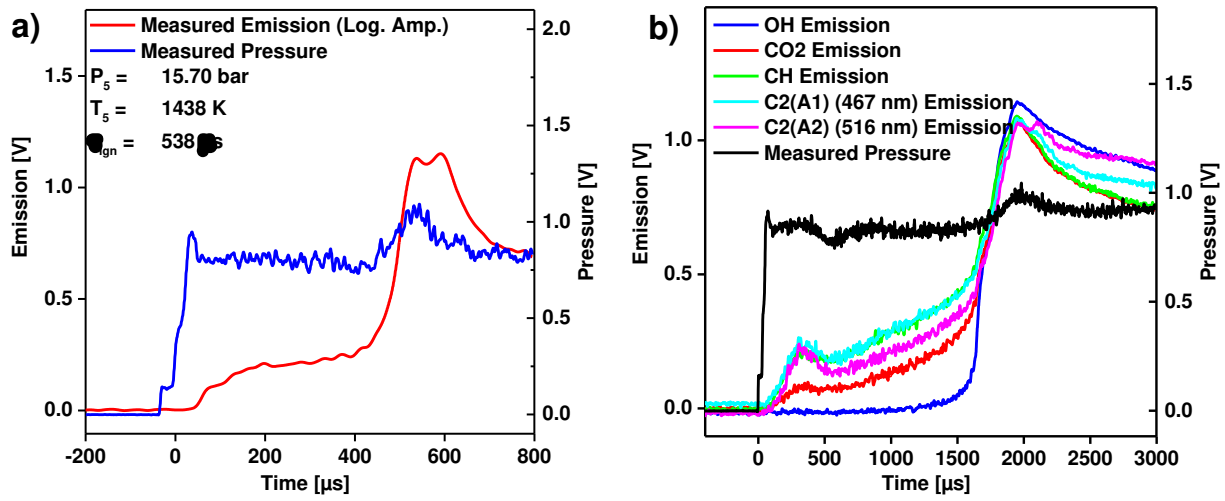

Figure 44: a) Example of ignition delay time measurement for Mixture 5 (X_{CH4} = 0.0726, X_{C2H6} = 0.0063, X_{O2} = 0.1645, X_{CO2} = 0.2567, X_{H2O} = 0.5000). The emission show an immediate rise after the arrival of the reflected shock wave before ignition occuring around 500 μs. b) Emission profiles at different wavelengths (310 nm, 375 nm, 431 nm, 476 nm, 516 nm.

CHAPTER 8: MECHANISM DEVELOPMENT

Predictions of the carbon monoxide during these systems is crucial for the entire system. To understand the chemical kinetics of carbon monoxide, a two-tiered approach was taken based on the information determined from the carbon monoxide time-histories data.

Using the Aramco 2.0 detailed mechanism, the carbon monoxide concentration was calculated for different conditions to determine how much carbon monoxide would be present at the end of the system. The oxidation of carbon monoxide is highly dependent of the temperature at which the reaction takes place. It was also determined that at different pressures, the temperature that is needed to oxidize CO is relatively constant. Figure 45 shows the carbon monoxide remaining after two different residence times in various temperature and pressure combinations.

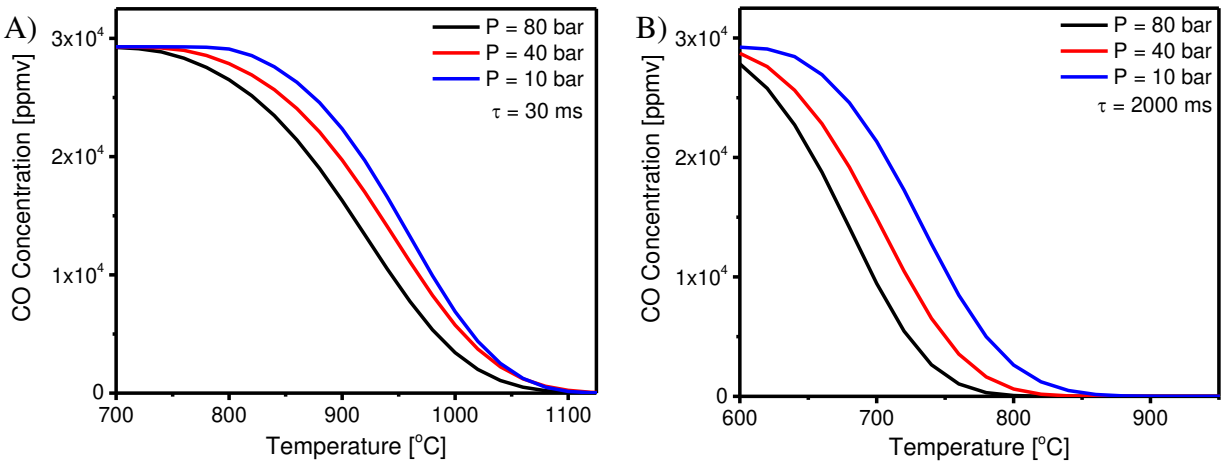

Figure 45: Temperature map for carbon monoxide oxidation at residence times of (A) 30 ms and (B) 2000 ms.

The model shows that below 800°C, the oxidation rate significantly reduces. Therefore, once the turbine reduces the gas to below this 800°C threshold, if carbon monoxide remains, not all of it will be oxidized. In short, the model demonstrates that temperature is a much greater driver in CO oxidation as compared to pressure.

Global chemical kinetic mechanisms were created to understand the chemical kinetics of the entire system. There are several mechanisms that exist in the literature for methane combustion that have been developed over the years. Jones and Lundstedt developed a four-step mechanism that included two fuel breakdown reactions and then included hydrogen oxidation and the water-gas shift reaction [68]. A second mechanism was created by Westbrook and Dryer that was most recently updated in 2007 combining fuel breakdown with the oxidation of carbon monoxide [69]. The problem was that as novel concepts to improve the efficiency and reduce the emissions are conceived, the two mechanisms start to leave the narrow range of conditions that the mechanisms were designed for. Neither mechanism could match the CO-CO_2 interactions that had been shown to be have important effects when CO_2 was used as the diluent compared to air [70-72].

In the last 10 years, these global mechanisms have been modified as oxy-fuel has become an increasingly important topic. Andersen et al. developed two mechanisms based on each of the mechanisms above and modified the reaction rates to predict oxy-fuel combustion in an isothermal plug flow reactor [73]. The mechanisms kept the initiation reactions from the original mixtures and modified the other steps to match the time-histories of major species. Improvements to the CO-CO_2 reaction subsets allowed for major improvements in the performance for oxy-fuel

conditions. The problem is that the mechanisms were not able to match the combustion time-scales that are seen in larger detailed mechanisms.

The new mechanism developed focuses matching ignition delay times and the global reactivity with the improvements that Andersen et al. made to the carbon monoxide concentration. The mechanism was also compared to data taken from the literature and the data presented in previous chapters to understand the extent of conditions that the modified mechanism can accurately model the oxy-fuel combustion.

8.1 Theory and Mechanism Development for Methane Global Mechanism

Modifications to the 3-step mechanism from Andersen et al. were taken to improve the combustion time-scales while maintaining the emissions improvements found in the original version. The modifications were performed on all three reactions on the pre-exponential factor, the activation energy and the reaction orders using a closed-homogeneous reactor with constant-pressure. The time-scales were based on ignition delay times. The mechanism was compared to the Westbrook and Dryer mechanism, the modified mechanism from Andersen et al. and the detailed Aramco 2.0 mechanism which contains 493 species and 2716 reactions [45, 69, 73]. The simulations were compared to data taken from Pryor et al. [74]. The modifications to the 3-step mechanism are shown in Table 10.

Table 10: Modifications to the Andersen et al. mechanism. Units for the mechanism are in cm, mole, s, K, cal.

	Reactions	A	β	E	Reaction Orders
1	$CH_4 + 1.5O_2 \Rightarrow CO + 2H_2O$	5.0×10^9	0	56.0×10^3	$[CH_4]^{0.4}\,[O_2]^{0.6}$
2	$CO + 0.5O_2 \Rightarrow CO_2$	4.0×10^8	0	10.0×10^3	$[CO]^{1.2}\,[O_2]^{0.25}\,[H_2O]^{0.5}\,[CO_2]^{-0.2}$
3	$CO_2 \Rightarrow CO + 0.5O_2$	6.0×10^8	-0.97	66.5×10^3	$[CO_2]^{0.8}\,[H_2O]^{0.5}\,[O2]^{-0.2}\,[CO]^{-0.3}$

Simulations were performed using Chemkin Pro software [66]. All ignition delay times for comparison were measured in UCF's shock tube. The shock tube was modeled using a constant-pressure reactor and the energy equation was solved. The initial temperature range for these simulations was 1000 – 2000 K. The mixture used for the development of the mechanism was kept constant at $X_{CH4} = 0.05$, $X_{O2} = 0.10$, $X_{CO2} = 0.85$. All five species (CH_4, O_2, CO, H_2O, CO_2) and temperature profiles were monitored during the simulations.

Typically, the ignition delay time is taken from an emissions profile for both experiments and the simulations. The ignition delay times for these simulations are taken from the methane time-histories of the experiments. Because the global mechanism does not include any radical species in the mechanism, a new definition for the ignition delay time has been created for this work. The ignition delay time was defined for all simulations as the time difference between the start of the simulation and the time when methane concentration reaches 5% of its initial value. Methane decay has been shown in Koroglu et al. to be a good approximation of the ignition delay times [33]. As a result, the methane profile was also included as a parameter for global mechanism improvements.

The original modified mechanism used by Andersen et al. employed an equilibrium approach to match the global mechanism constants to the stoichiometric constants. The mechanism created by Andersen et al. left the initiation reaction untouched from the values that were calculated from Westbrook and Dryer and focused on the CO-CO_2 subset. The problem is that ignition delay times are relatively insensitive to CO-CO_2 subset, being dominated by the first reaction. As such the initiation reaction was modified to more accurately model the system. The mechanism developed in this work was based on the methods outlined in Andersen et al. for developing a global mechanism for oxy-fuel conditions [73].

The accuracy of global mechanisms suffers as a result in the minimum number of species that are used in the model. This results in the breakdown in the fundamental thermodynamics that define the chemical kinetics field. This also allows for modifications to be made not only to the pre-exponential factor and the activation energy but also the reaction orders that are typically calculated internally in a detailed mechanism. The reaction orders were both reduced in order to ensure that the methane time profile matched the profile from the Aramco 2.0 mechanism which has been confirmed in the Koroglu et al. [33]. Figure 46 shows a comparison of the methane time-histories with the time-normalized to the ignition delay times for a temperature of 1500 K. Similar profiles are seen at other temperatures.

The issue that was created by altering the initiation reaction was that the peak CO level becomes much lower than the level compared to the detailed mechanism. The activation energies and the pre-exponential factors were altered as a result. The reaction orders were also edited to match the profile shapes of the major species time-histories. The addition of CO_2 and CO as negative reaction

orders in the forward and reverse CO oxidation reaction allowed for a high peak CO level while maintaining the carbon monoxide steady-state level and matching the max temperature during the simulation.

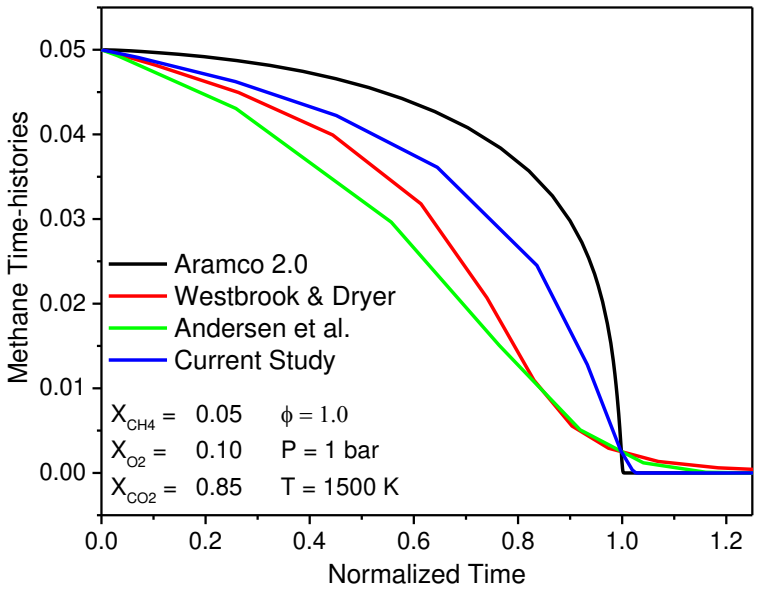

Figure 46: Comparison of the methane time-histories between different mechanisms at 1500 K. Time was normalized based on the ignition delay time for each mixture. The ignition delay times were defined as the time to reach 5% of the initial value of methane.

8.2 Global mechanism for oxy-methane combustion

The mechanism was compared to experimental data that was taken from Pryor et al. [74].The ignition delay times are much better modeled with the improved oxy-methane global mechanism compared to the previous state-of-the-art. Figure 47 shows the ignition delay times using the modifications to the reactions compared to the original Westbrook and Dryer mechanism and the modifications undertaken by Andersen et al. The different mechanisms are also compared to data

taken from Pryor et al. that shows the Aramco 2.0 mechanism does a good job predicting the ignition delay times [74]. By editing the pre-exponential factor and the activation energy of Reaction 1, both the ignition delay times and the slope of the curve could be matched to the detailed mechanism and experimental data that has been taken for this mixture. The new mechanism is unable to match the curve that occurs at the low temperatures of the detailed mechanism but there is no data that has been taken in this area to verify that this curvature is real.

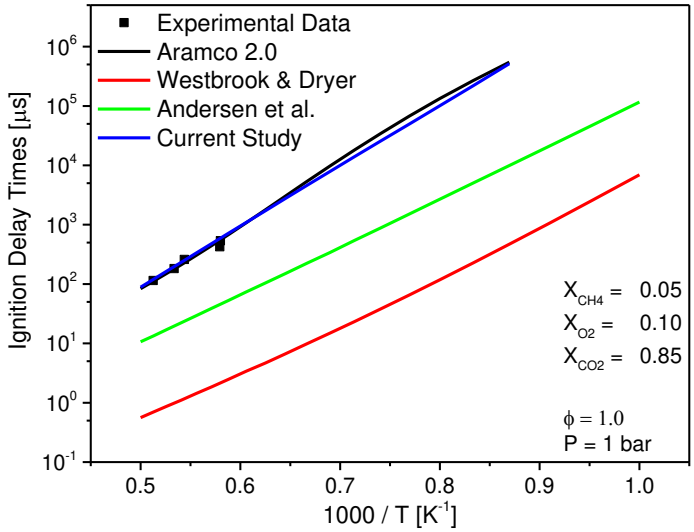

Figure 47: Ignition delay times for oxy-methane combustion using four different mechanisms. The experimental data was taken from Pryor et al [74]. Pressure for all simulations was kept at 1 bar. Mixture Composition: X_{CH4} = 0.05, X_{O2} = 0.10, X_{CO2} = 0.85.

The CH_4, CO, H_2O time-histories as well as temperature profiles were all considered during the development of the new mechanism. Three different temperatures were considered during this system at 1200 and 1800 K to represent the full range simulations.

CO concentration was an important species to monitor during the mechanism development. CO is the only intermediate and is a regulated species for power generation. Both the peak CO concentration and the steady-state CO level after ignition were considered during the development. Figure 48 shows the CO concentrations during the simulations at the 1200 K (Left) and 1800 K (Right). The mechanism is not able to match the peak level of CO during the simulations compared to the Aramco 2.0 mechanism. By altering the first reaction and the ignition delay times, the peak CO remained at a lower level than is expected by the detailed mechanism. The trends that are present in the Aramco 2.0 mechanism are maintained by the mechanism and the CO steady-state value is modeled relatively well at all conditions. The Andersen et al. mechanism did an excellent job of matching the steady-state value and was an important parameter shown in the paper but some accuracy in the level was sacrificed in this paper to match the time-scales that are shown by the Aramco 2.0 mechanism.

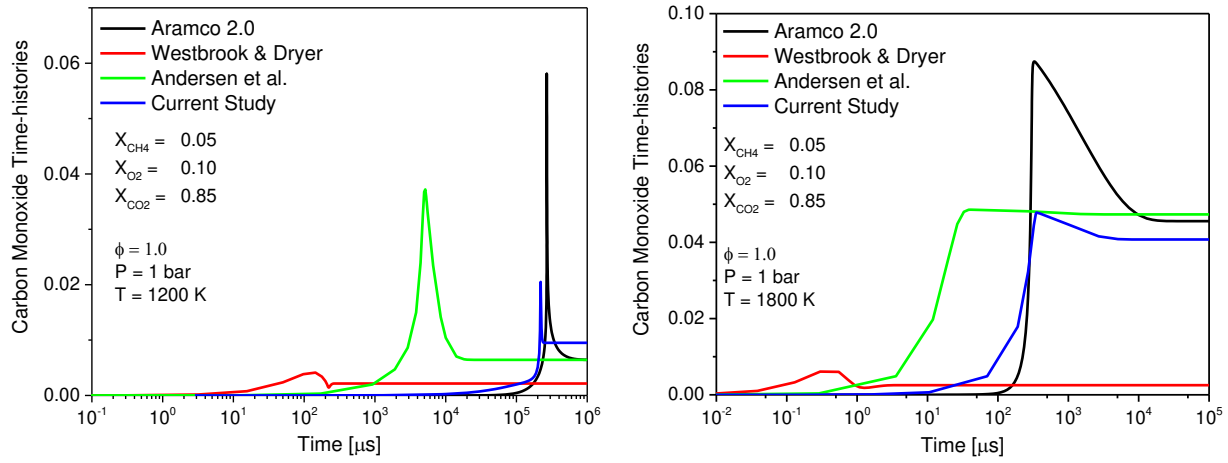

Figure 48: Carbon monoxide concentration time-histories. Left) temperature at 1200 K. Right) Temperature at 1800 K. Pressure was 1 bar. Mixture Composition: $X_{CH4} = 0.05$, $X_{O2} = 0.10$, $X_{CO2} = 0.85$.

The final two parameters that were considered during the simulations were the water time-histories and the temperature profiles. Both values were considered to ensure that there was little deviation from the desired trends in the Aramco 2.0 mechanism so that the mechanism could be as robust and accurate as possible. The maximum water concentration was already well modeled by both the Andersen et al. and Westbrook and Dryer mechanisms. During the development of the mechanism in this study, the water concentration did not undergo major changes and is still accurate throughout the simulations performed. Temperature profiles are shown at two different temperatures in Figure 49. The temperature profiles new mechanism can accurately measure the temperatures during the simulations at the lower temperatures but slightly over predicts the max temperature compared to the Aramco 2.0 and Andersen et al. mechanisms. The temperature profile of a decrease in the rate of the temperature rising was unable to be accurately simulated by any of the global mechanisms.

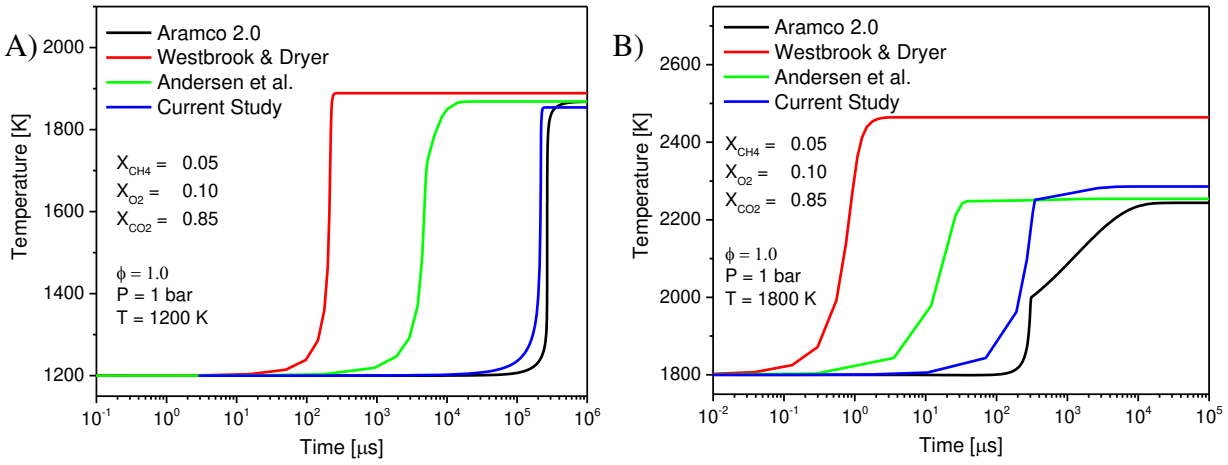

Figure 49: Comparison of temperature profiles between different mechanisms. A) Temperature at 1200 K. B) Temperature at 1800 K. Pressure was 1 bar. Mixture Composition: X_{CH4} = 0.05, X_{O2} = 0.10, X_{CO2} = 0.85.

8.3 Validation of Methane Mechanism

The global mechanism was compared to ignition delay times found in the literature to determine the full range of conditions that the mechanism could accurately predict. The mechanism was compared data taken from Koroglu et al. and Pryor et al. to understand the limits of the mechanism. The new updated mechanism does an excellent job at low pressures based on the data taken from Koroglu et al. and Pryor et al. [33, 67]. The mechanism can accurately predict the ignition delay times for one mixture and set of experiments but those were a limited number of experiments. The combination of these experiments includes various levels of carbon dioxide, different equivalence ratios, four different pressure ranges and several distinct levels of fuel loading.

The mechanism can accurately predict the ignition delay times for equivalence ratios between ϕ = 0.5 to 1.0, particularly at pressures close to 1 bar. Figure 50(Left: Stoichiometric Mixture, ϕ = 1.0,

Right: Lean Mixture, ϕ = 0.5) show the different mechanisms compared to experiments from Koroglu et al. [33]. The mechanism fails to predict the ignition delay times at rich mixtures. Using the data for ϕ = 2.0 from Koroglu et al., the updated mechanism does the worst performance of the three mechanisms. The Andersen et al. mechanism was originally under predicted the ignition delay times by an order of magnitude compared to the Aramco 2.0 mechanism and experimental data, but it does much better with higher equivalence ratios. The current study over predicts the ignition delay times by an order of magnitude while the Andersen et al. mechanism over predicts by 3 times the Aramco 2.0 mechanism.

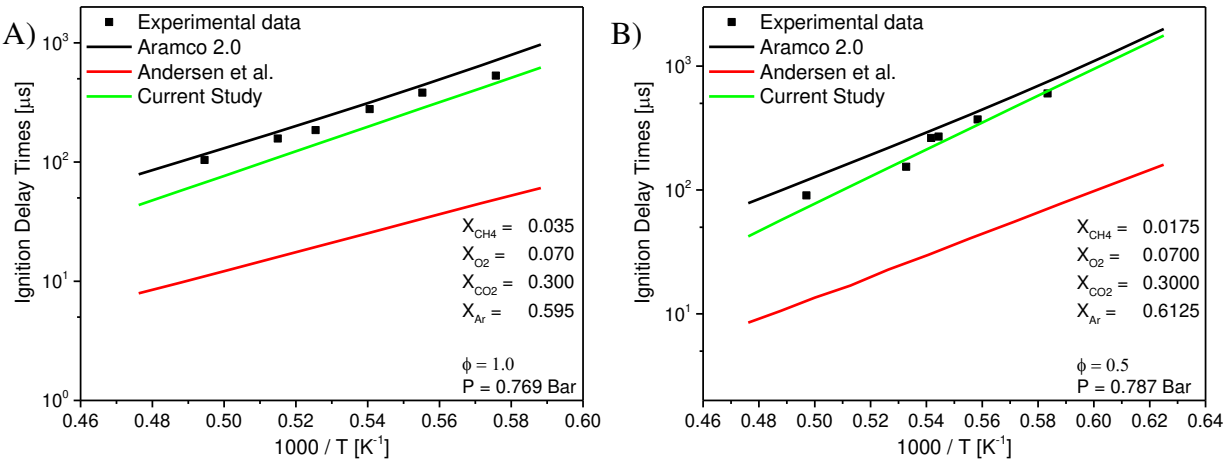

Figure 50: Ignition delay time comparisons to data from Koroglu et al [33]. A) Average pressure was 0.769 Bar. Mixture Composition: X_{CH4} = 0.035, X_{O2} = 0.070, X_{CO2} = 0.300, X_{Ar} = 0.595. B) Average pressure was 0.787 Bar. Mixture Composition: X_{CH4} = 0.0175, X_{O2} = 0.070, X_{CO2} = 0.300, X_{Ar} = 0.6125.

The mechanism was also compared to data that was taken at elevated pressures. Experimental data existed in Koroglu et al. and Pryor et al. at pressures around 4 bar, 8 bar and 30 bar [33, 67]. Two sets of experiments at different pressures are shown in Figure 51. The mechanism does not perform as well at these elevated pressures. The mechanism predicts the ignition delay times between

equivalence ratios between 0.5 and 1.0 but still is unable to predict the ignition delay times for rich conditions. For the lean and stoichiometric mixtures, the ignition delay times are over predicted by approximately a factor of 2 – 2.5 but can predict the energy required for the ignition delay times or the slope of the ignition delay time on the graph. For comparison, the Andersen et al. mechanism differed from the Aramco mechanism by a factor of 7 – 10 and had much greater variance in the numbers so it failed to match the slope that the Aramco 2.0 mechanism predicts.

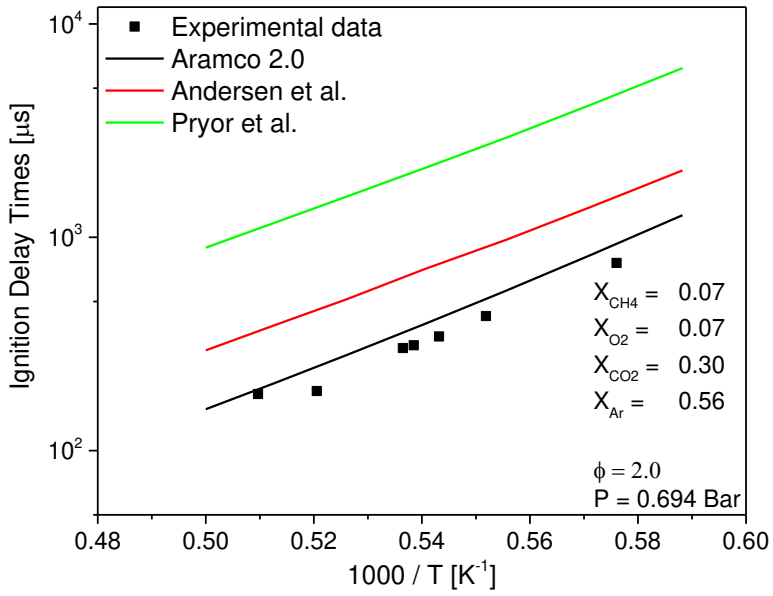

Figure 51: Ignition delay time comparisons for fuel rich conditions. Data taken from Koroglu et al [33]. Average pressure was 0.694 Bar. Mixture Composition: X_{CH4} = 0.07, X_{O2} = 0.07, X_{CO2} = 0.30, X_{Ar} = 0.56.

The same trend was seen in the ignition delay times for the experiments around 8 atm. The ratio between the ignition delay times predicted by the new mechanism compared to the Aramco 2.0 mechanism was 3.3 for both levels of CO_2 dilution while the Andersen et al. mechanism was off by a factor between 10 and 12. The new mechanism over predicts the mechanism and the experimental data points but still improves upon the original mechanism that it was built upon.

The final experiments that the mechanism was compared to was experiments taken at an average pressure of 30 bar. The new mechanism over predicts the ignition delay times by approximately 9 times the Aramco 2.0 mechanism while the Andersen et al. mechanism under predicts the ignition delay times by a factor of 12. The Aramco 2.0 mechanism also slightly over predicts the ignition delay times compared to the experimental trace so both mechanisms tend to be off by one order of magnitude. Figure 52 shows the comparison of the mechanism with data from Pryor et al.

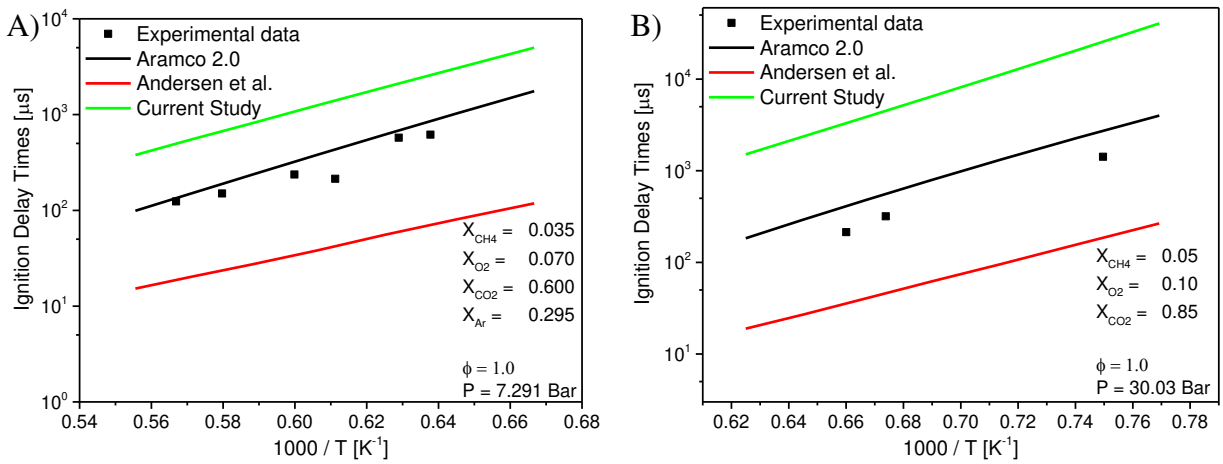

Figure 52: Ignition delay time comparisons to data from Pryor et al [67]. A) Average pressure was 7.291 Bar. Mixture Composition: X_{CH4} = 0.035, X_{O2} = 0.070, X_{CO2} = 0.600, X_{Ar} = 0.295. B) Average pressure was 30.03 Bar. Mixture Composition: X_{CH4} = 0.05, X_{O2} = 0.10, X_{CO2} = 0.300, X_{Ar} = 0.85.

8.4 Global mechanism for oxy-syngas combustion

Modifications have been made to the previous iteration of the syngas global mechanism. Table 11 shows the updated mechanism. The mechanism is based on the global mechanism created by Slavinskaya et al. [75]. The last two reactions were added from the global mechanism created for methane. These two reactions drive the mechanism to the equilibrium values after combustion.

Table 11: Global Reaction mechanism for oxy-syngas combustion. Units for the mechanism are in cm, mole, s, K, cal.

	Reactions	A	β	E	Reaction Orders
1	$2H_2 + O_2 \Rightarrow 2H_2O$	1.00×10^2	6.5	52.0×10^3	$[H_2]^{2.0}\,[O_2]^{1.4}$
2	$CO + O_2 + H_2 \Rightarrow CO_2 + H_2O$	2.00×10^1	5.9	47.0×10^3	$[CO]^{1.3}\,[O_2]^{0.8}\,[H_2]^{1.0}$
3	$CO + 0.5O_2 \Rightarrow CO_2$	4.00×10^8	0	10.0×10^3	$[CO]^{1.2}\,[O_2]^{0.3}\,[H_2O]^{0.5}\,[CO_2]^{-0.2}$
4	$CO_2 \Rightarrow CO + 0.5O_2$	3.50×10^{12}	-0.97	66.5×10^3	$[CO_2]^{0.8}\,[H_2O]^{0.5}\,[O_2]^{-0.2}\,[CO]^{0.2}$

The ignition delay times are shown in Figure 53 at 100 and 300 bar. The mechanism can predict the ignition delay times as predicted by the Aramco 2.0 mechanism for the arbitrary test mixture of $X_{H2} = 0.05$, $X_{CO} = 0.05$, $X_{O2} = 0.05$, $X_{CO2} = 0.85$. The ignition delay times for the global mechanism was taken as the time it takes to consume 90% of the initial hydrogen concentration in the fuel. The mechanism is referred to as the UCF Syngas Mechanism for the remainder of the section.

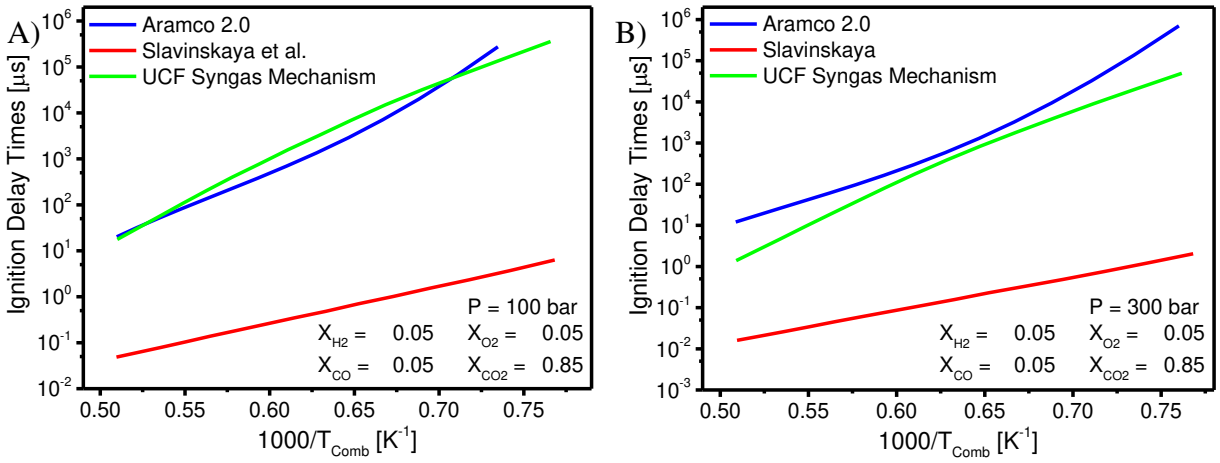

Figure 53: Ignition delay times at elevated pressures for syngas oxidation. A) Ignition delay times at 100 bar. B) Ignition delay times at 300 bar. The mixture for all simulations was X_{H2} = 0.05, X_{CO} = 0.05, X_{O2} = 0.05 and X_{CO2} = 0.85. Temperature is defined as the temperature after combustion. Combustion temperature ranged between 1000 and 2000 °C.

The mechanism was also compared to the carbon monoxide time-histories at 100 and 300 bar using the mechanism. The mechanism accurately predicted the major trends in the CO time-histories for the lower temperatures as shown in Figure 54. The CO time-histories slightly under predict the start of the CO consumption matched the rapid depletion once combustion starts. Due to the addition of the third and fourth reactions, the final value of CO is accurately predicted compared to the previous state-of-the art. Larger deviations in the CO time-histories appear at the higher temperatures. In Figure 55, The mechanisms match the Aramco 2.0 mechanism extremely well at 100 bar but starts to show multiple time-scales as it depletes. It starts with a rapid depletion but slows as a change in the dominate reaction occurs. This feature is even more pronounced at the 1690 °C (Figure 56) where the first time-scale occurs around an order of magnitude faster. The difference in the mechanisms appears to grow with increasing pressure and temperature but in the real combustor environment, the combustion residence time is at the range of 10^3-10^4 µs level which is after the CO is shown to reach the steady-state conditions. This shows that the main

differences between the global and detailed mechanisms are less important at the higher pressures and temperatures.

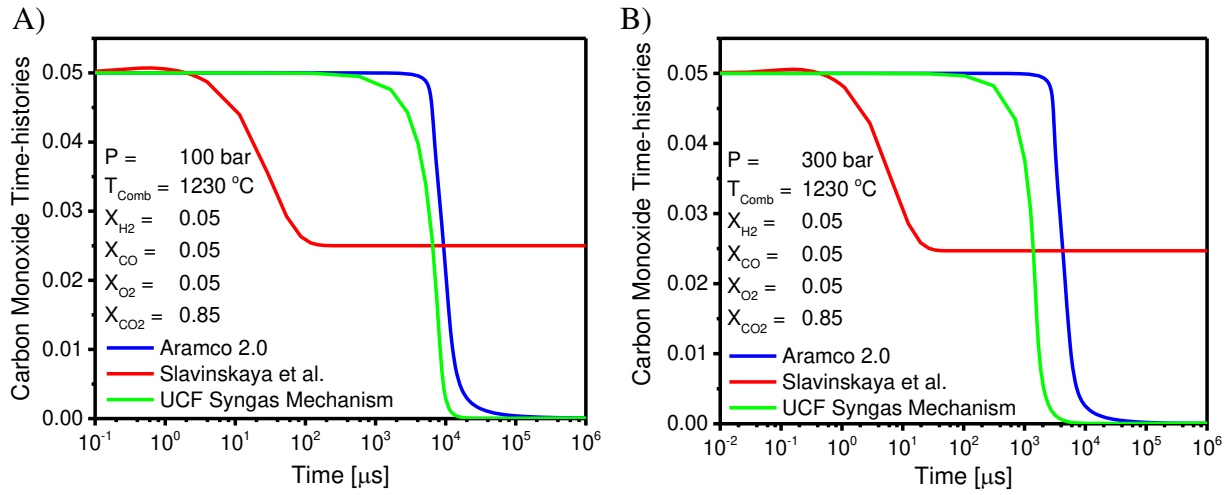

Figure 54: Carbon monoxide time-histories for syngas global mechanism at 1230°C. a) Simulation results for 100 bar. b) Simulations results for 300 bar. All simulations were performed with a mixture of $X_{H2} = 0.05$, $X_{CO} = 0.05$, $X_{O2} = 0.05$, $X_{Ar} = 0.85$.

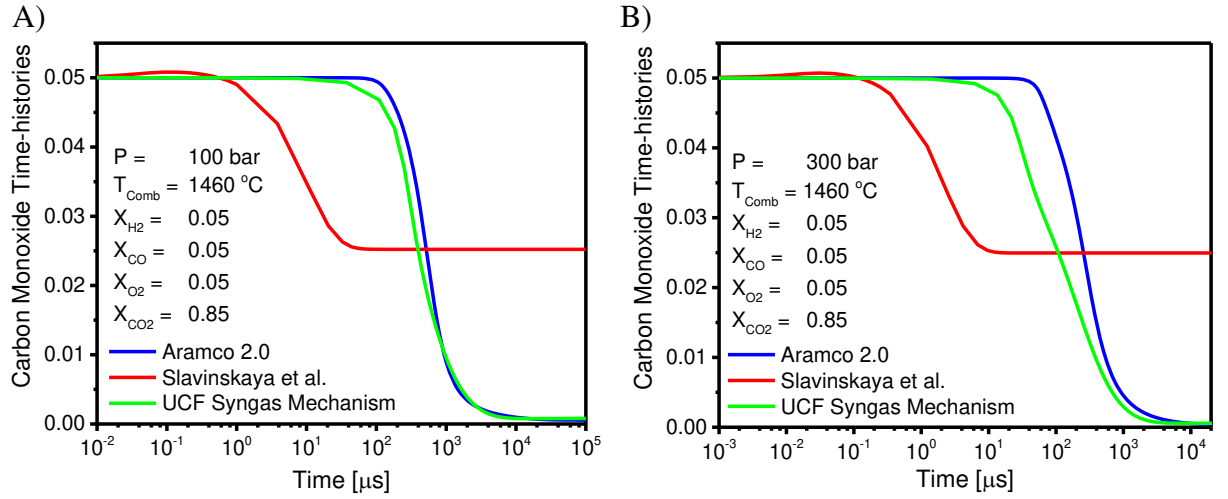

Figure 55: Carbon monoxide time-histories for syngas global mechanism at 1460°C. a) Simulation results for 100 bar. b) Simulations results for 300 bar. All simulations were performed with a mixture of $X_{H2} = 0.05$, $X_{CO} = 0.05$, $X_{O2} = 0.05$, $X_{Ar} = 0.85$.

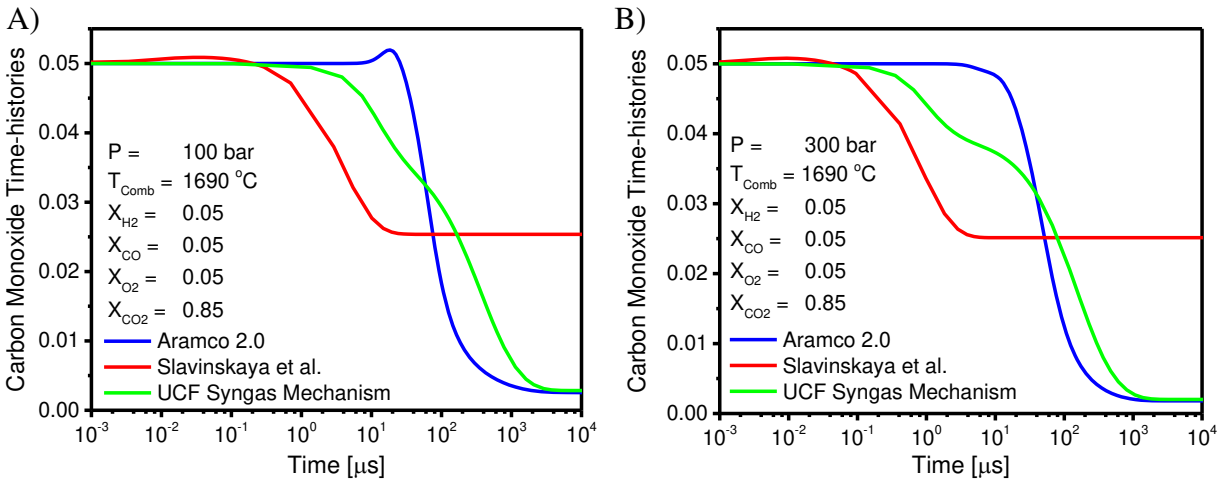

Figure 56: Carbon monoxide time-histories for syngas global mechanism at 1690°C. a) Simulation results for 100 bar. b) Simulations results for 300 bar. All simulations were performed with a mixture of $X_{H2} = 0.05$, $X_{CO} = 0.05$, $X_{O2} = 0.05$, $X_{Ar} = 0.85$.

CHAPTER 9: CONCLUSIONS

The chemical kinetics and fluid dynamics were explored for oxy-fuel combustion behind reflected shockwaves. Several different topics were examined for a comprehensive understanding of how carbon dioxide dilution affects the combustion of different hydrocarbon fuels. All the experiments were performed using a shock tube for methane, syngas and ethylene mixtures. Experiments were performed between 1000 – 2000 K for pressures up to 30 atm.

The fluid dynamics of carbon dioxide dilution was examined using high-speed imaging. Based on the images, the reaction zone when carbon dioxide was added was significantly reduced compared to argon diluted mixtures. The area that ignited was reduced from upwards of 95% of the shock tube to as low as 25% of the area. The other major conclusion that was determined with the fluid dynamics is that the reaction zone is no longer homogeneous across the range of experiments. The main reason for the reduction in size and homogeneity of the ignition area is from the bifurcation of the shock wave but the global reactivity seems to be well modeled with the Aramco 2.0 mechanism.

It was also shown that the uncertainty in ignition delay time experiments was increased with carbon dioxide dilution. Examining the emission profile, it was determined that carbon dioxide increases the width of the emission profile. A typical emission profile had a rise time of 17% of the time at peak emission. With the addition of carbon dioxide to the system, the rise time increased to up to 50%.

The ignition delay times for all three fuels were measured behind reflected shock waves. It was determined that methane was well modeled by the Aramco 2.0 mechanism, but the model did not perform as well for syngas and ethylene ignition delay times. The model overpredicted the elevated temperature experiments for ethylene, particularly at atmospheric pressures. The model also overpredicted the ignition delay times at the elevated pressures as the temperature decreased.

Correlations were created for all three fuels to predict the ignition delay times. The correlation for methane included data taken from Koroglu et al. [33]. The correlation can accurately predict ignition delay times during methane combustion over an extensive range of conditions. The ignition delay times were also measured for a fourth mixture, a blend of methane and ethane. A higher fuel loading was examined, and it was determined that a higher fuel loading increases the scatter of the ignition delay times. The study also extended the temperature range to as low as 900 K for CO_2 diluted methane mixtures.

The concentrations of two species were measured during experiments. Methane time-histories were measured for various levels of carbon dioxide dilution. It was shown that the methane concentrations are well predicted by the Aramco 2.0 mechanism despite increased noise in the signal due to the bifurcation of the shock wave. The $1/3^{rd}$ methane decay times were also measured using the laser and it was determined that the methane decay time is a good approximation for ignition delay times in methane mixtures. Carbon monoxide was also measured in different fuels and it was determined that the Aramco 2.0 mechanism performs at various levels depending the fuel. The mechanism struggles to predict the carbon monoxide time-histories for methane oxidation under most of the conditions measured. The mechanism overpredicted the carbon

monoxide concentrations at atmospheric pressures for both stoichiometric and fuel-rich conditions. The mechanism performs much better for ethylene and syngas oxidation. The main issue that was determined is that the absorbance from carbon dioxide extremely high for elevated pressures.

The ignition delay times were also measured to understand the addition of water in the system and has been shown that for low levels of water addition (up to 15%), the Aramco 2.0 mechanism is able to accurately predict the ignition delay times. However, at elevated levels of water addition (50%) in the system, the ignition delay times are underpredicted compared to the experiments. Sensitivity analysis indicate that understanding the third-body collision efficiencies of CO_2 and H_2O are crucial for accurately modeling the data.

Two different global mechanisms were created for oxy-methane and oxy-syngas combustion. The mechanism developed for methane was shown to predict the ignition delay times and the carbon monoxide concentrations when compared to the Aramco 2.0 mechanism. The mechanism was validated with the experimental data up to 30 atm. The mechanism was able to predict experimental data at both stoichiometric and fuel-lean conditions but struggled to predict the ignition delay times for fuel-rich conditions. Simulations with the Aramco 2.0 mechanism were extrapolated up to 300 atm and temperatures up to 2000 K and the global mechanism was able to predict the ignition delay times and major species concentrations. The syngas mechanism was also compared to Aramco 2.0 mechanism up to 300 atm. The mechanism follows the same general trends as the Aramco 2.0 mechanism, but two distinct time-scales were shown at the highest pressure and temperature simulations. These time-scales show that there is a difference between the reaction

rates between the two initiation reactions, but the overall time-scales are shorter than the characteristic times for a combustor.

Overall, it has been shown that the Aramco 2.0 mechanism is able to predict the global reactivity for oxy-fuel combustion. The mechanism is shown to predict the ignition delay times and the rate of fuel decay but struggles with the carbon monoxide time-histories. More work is needed to understand how carbon dioxide dilution affects the carbon monoxide time-histories. It has also been shown that the fluid dynamics behind the reflected shock wave are strongly affected by the addition of carbon dioxide to the system. Future work should focus on extending the pressure and temperature ranges for the ignition delay times as well as improving the predictive ability of chemical kinetic mechanisms to design novel combustor designs and help usher in this potentially revolutionary technology.

REFERENCES

[1] J. Pires, F. Martins, M. Alvim-Ferraz, M. Simões, Recent developments on carbon capture and storage: an overview, Chemical Engineering Research and Design 89 (2011) 1446-1460.

[2] V. Dostal, P. Hejzlar, M.J. Driscoll, The supercritical carbon dioxide power cycle: comparison to other advanced power cycles, Nuclear technology 154 (2006) 283-301.

[3] J. Gibbins, H. Chalmers, Carbon capture and storage, Energy Policy 36 (2008) 4317-4322.

[4] A. McClung, K. Brun, L. Chordia, Technical and economic evaluation of supercritical oxy-combustion for power generation, 4th International Supercritical CO2 Power Cycles Symposium, (2014).

[5] R. Allam, J. Fetvedt, B. Forrest, D. Freed, The Oxy-Fuel, Supercritical CO2 Allam Cycle: New Cycle Developments to Produce Even Lower-Cost Electricity From Fossil Fuels Without Atmospheric Emissions, ASME Turbo Expo 2014: Turbine Technical Conference and Exposition, (2014).

[6] Annual Energy Outlook 2014. http://www.eia.gov/forecasts/aeo/pdf/0383(2014).pdf 2015).

[7] P. Sabia, M.L. Lavadera, G. Sorrentino, P. Giudicianni, R. Ragucci, M. de Joannon, H2O and CO2 dilution in MILD combustion of simple hydrocarbons, Flow, Turbulence and Combustion 96 (2016) 433-448.

[8] G. Sorrentino, P. Sabia, M. de Joannon, A. Cavaliere, R. Ragucci, The effect of diluent on the sustainability of MILD combustion in a cyclonic burner, Flow, Turbulence and Combustion 96 (2016) 449-468.

[9] Y. Xie, J. Wang, M. Zhang, J. Gong, W. Jin, Z. Huang, Experimental and Numerical Study on Laminar Flame Characteristics of Methane Oxy-fuel Mixtures Highly Diluted with CO2, Energy & Fuels 27 (2013) 6231-6237.

[10] F. Liu, H. Guo, G.J. Smallwood, The chemical effect of CO2 replacement of N2 in air on the burning velocity of CH4 and H2 premixed flames, Combustion and Flame 133 (2003) 495-497.

[11] M. Holton, P. Gokulakrishnan, M. Klassen, R. Roby, G. Jackson, Autoignition delay time measurements of methane, ethane, and propane pure fuels and methane-based fuel blends, Journal of Engineering for Gas Turbines and Power 132 (2010) 091502.

[12] A.G. Gaydon, I.R. Hurle, The shock tube in high-temperature chemical physics, Reinhold Publishing Corp., NY, 1963.

[13] H. Mirels, Test Time in Low-Pressure Shock Tubes, The Physics of Fuilds 6 (1963) 1201.

[14] H. Mirels, Shock Tube Test Time Limitation Due to Turbulent-Wall Boundary Layer, AIAA J. 2 (1964) 84.

[15] H. Mirels, Correlation Formulas for Laminar Shock Tube Boundary Layer, The Physics of Fuilds 9 (1966) 1265.

[16] H. Mirels, Flow Nonuniformity in Shock Tubes Operating at Maximum Test Times, The Physics of Fuilds 9 (1966) 1907.

[17] H. Mirels, J. Hamman, Laminar boundary layer behind strong shock moving with nonuniform velocity, The Physics of Fuilds 5 (1962) 91.

[18] H. Mark, The interaction of a reflected shock wave with the boundary layer in a shock tube, National Advisory Committee for Aeronautics1958.

[19] E.L. Petersen, A Shock Tube and Diagnostics for Chemistry Measurement at Elevated Pressures with Application to Methane Ignition, Mechanical Engineering, Stanford University, Stanford, 1998.

[20] L. Davies, J.L. Wilson, Influence of Reflected Shock and Boundary-Layer Interaction on Shock-Tube Flows, Physics of Fluids 12 (1969) I-37-I-43.

[21] H. Kleine, V. Lyakhov, L. Gvozdeva, H. Grönig, Bifurcation of a reflected shock wave in a shock tube, Shock Waves, (1992) 261-266.

[22] V. Fokeev, L. Gvozdeva, Study of bifurcation of reflected shock waves in channels of various cross-sections, Current Topics in Shock Waves 17th International Symposium on Shock Waves and Shock Tubes 208 (1990) 862-866.

[23] E. Petersen, R. Hanson, Measurement of reflected-shock bifurcation over a wide range of gas composition and pressure, Shock Waves 15 (2006) 333-340.

[24] R.J. Sanderson, Interpretation of pressure measurements behind the reflected shock in a rectangular shock tube., AIAA Journal 7 (1969) 1370.

[25] Y.S. Weber, E.S. Oran, J.P. Boris, J.D. Anderson Jr., Physics of Fluids 7 (1995) 2475.

[26] V. Daru, C. Tenaud, Numerical Simulation of the Shock Wave /Boundary Layer Interaction in a Shock Tube by Using a High Resolution Monotonicity-Preserving Scheme, 3rd International Conference on Computational Fluid Dynamics (ICCFD3), (2004).

[27] M. Nishida, L. Min-gyoo, Reflected-shock/side-boundary-layer interaction in a shock tube, Album of visualization 13 (1996) 1-2.

[28] G.J. Wilson, S.P. Sharma, W.D. Gillespie, Time-dependent simulation of reflected-shock/boundary layer interaction, 31st AIAA Aerospace Sciences Meeting and Exhibit 1 (1993).

[29] K.P. Grogan, M. Ihme, Regimes describing shock boundary layer interaction and ignition in shock tubes, Proceedings of the Combustion Institute, (2016).

[30] S. Walton, X. He, B. Zigler, M. Wooldridge, A. Atreya, An experimental investigation of iso-octane ignition phenomena, Combustion and Flame 150 (2007) 246-262.

[31] P.R. Bevington, D.K. Robinson, Data reduction and error analysis, McGraw–Hill, New York, (2003).

[32] J.E. John, T.G. Keith, Gas Dynamics, 3rd ed., Pearson Hall, Upper Saddle River, N.J., 2006.

[33] B. Koroglu, O.M. Pryor, J. Lopez, L. Nash, S.S. Vasu, Shock tube ignition delay times and methane time-histories measurements during excess CO 2 diluted oxy-methane combustion, Combustion and flame 164 (2016) 152-163.

[34] A.S. Pine, Self-, N2, O2, H2, Ar, and He broadening in the ν3 band Q branch of CH4, The Journal of Chemical Physics 97 (1992) 773-785.

[35] S.H. Pyun, W. Ren, D.F. Davidson, R.K. Hanson, Methane and ethylene time-history measurements in n-butane and n-heptane pyrolysis behind reflected shock waves, Fuel 108 (2013) 557-564.

[36] K.-Y. Lam, W. Ren, S.H. Pyun, A. Farooq, D.F. Davidson, R.K. Hanson, Multi-species time-history measurements during high-temperature acetone and 2-butanone pyrolysis, Proceedings of the Combustion Institute 34 (2013) 607-615.

[37] S.H. Pyun, J. Cho, D.F. Davidson, R.K. Hanson, Interference-free mid-IR laser absorption detection of methane, Measurement Science and Technology 22 (2011) 025303.

[38] O. Pryor, G. Barari, B. Koroglu, J. Lopez, L. Nash, S.S. Vasu, Shock Tube Ignition Studies of Advanced Biofuels, 52nd AIAA/SAE/ASEE Joint Propulsion Conference, (2016).

[39] B. Koroglu, O. Pryor, J. Lopez, L. Nash, S.S. Vasu, Methane Ignition Delay Times in CO2 Diluted Mixtures in a Shock Tube, 51st AIAA/SAE/ASEE Joint Propulsion Conference, (2015).

[40] B. Koroglu, O. Pryor, J. Lopez, L. Nash, S.S. Vasu, Shock Tube Ignition and CH4 Time-Histories during Propanal Oxidation, 54th AIAA Aerospace Sciences Meeting, (2016).

[41] B. Koroglu, S.S. Vasu, Measurements of Propanal Ignition Delay Times and Species Time Histories Using Shock Tube and Laser Absorption, Int. J. Chem. Kinet. 48 (2016) 679-690.

[42] V. Troutman, C. Strand, M. Campbell, A. Tulgestke, V. Miller, D. Davidson, R. Hanson, High-speed OH* chemiluminescence imaging of ignition through a shock tube end-wall, Appl. Phys. B 122 (2016) 1-7.

[43] CHEMKIN-PRO 15131, Reactiondesign, San Diego, CA., 2013.

[44] G.P. Smith, D.M. Golden, M. Frenklach, N.W. Moriarty, B. Eiteneer, M. Goldenberg, C.T. Bowman, R.K. Hanson, S. Song, W.C. Gardiner Jr, GRI-Mech 3.0, 1999.

[45] W.K. Metcalfe, S.M. Burke, S.S. Ahmed, H.J. Curran, A Hierarchical and Comparative Kinetic Modeling Study of C1 − C2 Hydrocarbon and Oxygenated Fuels, International Journal of Chemical Kinetics 45 (2013) 638-675.

[46] S. Richter, T. Kathrotia, C. Naumann, T. Kick, N. Slavinskaya, M. Braun-Unkhoff, U. Riedel, Experimental and modeling study of farnesane, Fuel 215 (2018) 22-29.

[47] B. Koroglu, O.M. Pryor, J. Lopez, L. Nash, S.S. Vasu, Shock tube ignition delay times and methane time-histories measurements during excess CO2 diluted oxy-methane combustion, Combustion and flame 164 (2016) 152-163.

[48] A. Burcat, B. Ruscic, Third millenium ideal gas and condensed phase thermochemical database for combustion with updates from active thermochemical tables, Argonne National Laboratory Argonne, IL2005.

[49] E.L. Petersen, R.K. Hanson, Measurement of reflected-shock bifurcation over a wide range of gas composition and pressure, Shock Waves 15 (2006) 333.

[50] D. Bull, D. Edwards, An investigation of the reflected shock interaction process in a shock tube, AIAA Journal 6 (1968) 1549-1555.

[51] L. Davies, J. Wilson, Influence of Reflected Shock and Boundary-Layer Interaction on Shock-Tube Flows, Physics of Fluids (1958-1988) 12 (1969) I-37-I-43.

[52] H. Kleine, V. Lyakhov, L. Gvozdeva, H. Grönig, Bifurcation of a reflected shock wave in a shock tube, Shock Waves, Springer1992, pp. 261-266.

[53] M. Ihme, Y. Sun, R. Deiterding, Detailed Simulations of shock-bifurcation and ignition of an argon-diluted hydrogen/oxygen mixture in a shock tube, AIAA Paper 538 (2013) 1-14.

[54] H. Yamashita, J. Kasahara, Y. Sugiyama, A. Matsuo, Visualization study of ignition modes behind bifurcated-reflected shock waves, Combustion and flame 159 (2012) 2954-2966.

[55] P. Andrzej J. Nowak, M. Lamnaouer, A. Kassab, E. Divo, N. Polley, R. Garza-Urquiza, E. Petersen, A conjugate axisymmetric model of a high-pressure shock-tube facility, International Journal of Numerical Methods for Heat & Fluid Flow 24 (2014) 873-890.

[56] J.W. Hargis, E.L. Petersen, Methane Ignition in a Shock Tube with High Levels of CO2 Dilution: Consideration of the Reflected-Shock Bifurcation, Energy & Fuels 29 (2015) 7712-7726.

[57] J. Ye, P.R. Medwell, B.B. Dally, M.J. Evans, The transition of ethanol flames from conventional to MILD combustion, Combustion and Flame 171 (2016) 173-184.

[58] T. Plessing, N. Peters, J.G. Wünning, Laseroptical investigation of highly preheated combustion with strong exhaust gas recirculation, International Symposium on Combustion 27 (1998) 3197-3204.

[59] M. Evans, P. Medwell, H. Wu, A. Stagni, M. Ihme, Classification and lift-off height prediction of non-premixed MILD and autoignitive flames, Proceedings of the combustion institute, (2016).

[60] G. Szegö, B. Dally, G. Nathan, Operational characteristics of a parallel jet MILD combustion burner system, Combustion and Flame 156 (2009) 429-438.

[61] M. Ihme, Y. Sun, R. Deiterding, Detailed Simulations of shock-bifurcation and ignition of an argon-diluted hydrogen/oxygen mixture in a shock tube, 51st AIAA Aerospace Sciences Meeting including the New Horizons Forum and Aerospace Exposition, (2013) 538.

[62] A.J. Nowak, M. Lamnaouer, A. Kassab, E. Divo, N. Polley, R. Garza-Urquiza, E. Petersen, A conjugate axisymmetric model of a high-pressure shock-tube facility, International Journal of Numerical Methods for Heat & Fluid Flow 24 (2014) 873-890.

[63] L. Rothman, I. Gordon, R. Barber, H. Dothe, R. Gamache, A. Goldman, V. Perevalov, S. Tashkun, J. Tennyson, HITEMP, the high-temperature molecular spectroscopic database, Journal of Quantitative Spectroscopy and Radiative Transfer 111 (2010) 2139-2150.

[64] L.S. Rothman, I.E. Gordon, Y. Babikov, A. Barbe, D.C. Benner, P.F. Bernath, M. Birk, L. Bizzocchi, V. Boudon, L.R. Brown, The HITRAN2012 molecular spectroscopic database, Journal of Quantitative Spectroscopy and Radiative Transfer 130 (2013) 4-50.

[65] C. Mulvihill, E. Petersen, High-temperature argon broadening of CO2 near 2190 cm− 1 in a shock tube, Appl. Phys. B 123 (2017) 255.

[66] R. Design, CHEMKIN-PRO 15131, San Diego, CA., 2013.

[67] O. Pryor, S. Barak, J. Lopez, E. Ninnemann, B. Koroglu, L. Nash, S. Vasu, High Pressure Shock Tube Ignition Delay Time Measurements During Oxy-Methane Combustion With High Levels of CO2 Dilution, Journal of Energy Resources Technology 139 (2017) 042208-042208-042206.

[68] W. Jones, R. Lindstedt, Global reaction schemes for hydrocarbon combustion, Combustion and flame 73 (1988) 233-249.

[69] C.K. Westbrook, F.L. Dryer, Simplified reaction mechanisms for the oxidation of hydrocarbon fuels in flames, Combustion science and technology 27 (1981) 31-43.

[70] S.p.d. Persis, G. Cabot, L. Pillier, I. Gökalp, A.M. Boukhalfa, Study of Lean Premixed Methane Combustion with CO2 Dilution under Gas Turbine Conditions, Energy and Fuels, (2012).

[71] B. Almansour, L. Thompson, J. Lopez, G. Barari, S.S. Vasu, Laser Ignition and Flame Speed Measurements in Oxy-Methane Mixtures Diluted With CO2, Journal of Energy Resources Technology 138 (2016) 032201.

[72] P. Glarborg, L.L. Bentzen, Chemical effects of a high CO2 concentration in oxy-fuel combustion of methane, Energy & Fuels 22 (2007) 291-296.

[73] J. Andersen, C.L. Rasmussen, T. Giselsson, P. Glarborg, Global combustion mechanisms for use in CFD modeling under oxy-fuel conditions, Energy & Fuels 23 (2009) 1379-1389.

[74] O. Pryor, S. Barak, B. Koroglu, E. Ninnemann, S.S. Vasu, Measurements and interpretation of shock tube ignition delay times in highly CO2 diluted mixtures using multiple diagnostics, Combustion and Flame 180 (2017) 63-76.

[75] N. Slavinskaya, M. Braun-Unkhoff, P. Frank, Reduced reaction mechanisms for methane and syngas combustion in gas turbines, Journal of Engineering for Gas Turbines and Power 130 (2008) 021504.